A Study of Cosmic-Ray Acceleration History in Supernova Remnants through Observations of Synchrotron X-ray Radiation

Ryoko Nakamura

Department of Physics, Tokyo Institute of Technology
&
The Institute of Space and Astronautical Science

February 8, 2010

Abstract

We study the cosmic-ray acceleration history in the shocks of Supernova Remnants (SNRs) using observations of synchrotron X-ray emission from accelerated electrons.

As a first step, we searched synchrotron X-ray emission from SNRs from which the TeV γ-rays were detected. We focused on the TeV-detected SNRs because the TeV γ-ray emission is direct evidence of cosmic-ray acceleration up to $\sim$ TeV. As a result, we succeeded to discover synchrotron X-ray emission from two SNRs, W28 and CTB37B. In the case of W28, a middle-aged SNR, we detected hard-tail X-ray emission from inside the shell of north-eastern part with the *XMM-Newton* observatory. We consider that this hard component is most probably the synchrotron X-ray emission from accelerated electrons. The spectrum was described by a power-law with a photon index of ~ 3, and the 2–10 keV luminosity was 6.9×10^{32} erg/s. In addition, X-ray emission from thermal plasma was also detected. The thermal emission was described by an non-equilibrium collisional ionization plasma model (so-called "NEI" model) with a temperature, a pre-shock electron density, and an age of ~ 0.3 keV, ~ 0.1 cm^{-3}, and several times 10^4 yr, respectively. For the other SNR CTB37B, we obtained a clear image and high quality spectra of diffuse X-ray emission for the first time with the *Suzaku* satellite. Synchrotron X-ray emission and weak thermal X-ray emission were detected from the southern region of CTB 37B. Its photon index and a 2–10 keV luminosity of the synchrotron X-ray component were 1.5 and 9.7×10^{33} erg/s, respectively. We obtained a tight upper limit of pre-shock electron density as < 0.21 cm^{-3} from the spectral analysis of the thermal component. These results indicate that the cosmic-ray acceleration occurs in the regions of low plasma density for both SNRs.

As a next step, we compiled a sample of SNRs from which the synchrotron X-ray emission was detected including our new results. The compilation includes several physical parameters of the SNRs, such as an actual radius, a synchrotron X-ray luminosity, a plasma electron density, and so on. Because it is generally difficult to estimate the age of the SNR, we adopted its radius as a measure of the age, and constructed a radius-luminosity relation. We found that the luminosity drops off around the radius of ~ 10 pc, which corresponds to approximately an age of ~ 1000 yr.

To understand the luminosity drop-off, we constructed a simple model describing the time history of particle acceleration in SNRs based on the SNR dynamic and magnetic evolution and the theory of diffusive shock acceleration. The model describes the magnetic field strength and maximum electron energy as a function of the shock velocity, which is determined by the number density, n_0, of the interstellar plasma. This means that the electron acceleration history depends on n_0. The model can successfully reproduce the radius-luminosity relation including the drop-off. According to the model, electron acceleration up to $\sim$ TeV, which is necessary for the synchrotron X-ray emission, is sustained longer when n_0 is smaller. In fact, plasma density measured by the thermal emission generally satisfies $n_0 < 1.0$ cm^{-3}, except for the young SNR, Cas A. In addition, we found that the maximum electron energy $E_{\rm max,e}$ reaches 10^{13} – 10^{14} TeV according to this model.

With the same model of electron acceleration, proton acceleration history can also be investigated. In contrast to the electron acceleration, protons are accelerated to $\sim 10^{15}$ eV with little density dependence of ${n_0}^{1/6}$. Protons are rapidly accelerated to the maximum energy in the free expansion phase, and sustain $\sim 10^{15}$ eV with little energy loss for

$\geq 10^7$ year. Using the cataloged TeV γ-ray luminosities, we studied the relation between radius and luminosity, and no luminosity drop-off was found. This result is consistent with the proton origin (i.e. decay of the neutral pions) of the TeV γ-ray emission. As a cross-check, we calculated the TeV γ-ray luminosity due to the Inverse Compton (IC) scattering based on our model. The luminosity obtained was smaller than the observed one by a factor of ~ 100. Furthermore, the calculated radius-luminosity curve shows a cut-off around $5 \leq R \leq 10$ pc with $n_0 > 0.1$ cm^{-3}. This result indicates that we need to incorporate at least multi-zone IC scattering, if we want to explain the TeV γ-ray emission by the IC scattering. However, the explanation does not work for large (old) SNRs because of the short life of TeV electrons.

Contents

List of Figures

List of Tables

Chapter 1

Introduction

Cosmic rays are high energy particles flying in the universe with energy up to 10^{20} eV. The energy density of cosmic ray is $\sim$1 eV cm^{-3}, which is one of the main component in our Galaxy like cosmic microwave background, magnetic field, stellar lights, and so on. However, the origin of cosmic rays are still unknown since the discovery in 1912 (Hess, 1911, 1912).

For a long time, Supernova Remnants (SNRs) have been considered to be one of the most promising acceleration sites of cosmic rays up to $\sim 10^{15.5}$ eV (the knee energy). The theory of diffusive shock acceleration in SNRs can explain efficient particle acceleration and the observed comic ray flux. Chemical composition of cosmic rays consists of not only proton but also heavy elements, which means acceleration site has rich metals, like SNRs. Energy budget of cosmic rays can be explained with supernova expansion energy of 10^{51} ergs and expansion rate of $\sim$1 per 30 yr. These facts also support the assumption of cosmic ray acceleration in SNRs, although nobody had any observational evidence.

A breakthrough was brought by hard X-ray studies of SNRs. Koyama et al. (1995) discovered synchrotron X–ray from the shell of SN 1006, indicating the existence of extremely high energy electrons up to $\sim$100 TeV produced by the first-order Fermi acceleration. Following this discovery, the synchrotron X-ray emission has been discovered from a few more young shell-type SNRs, such as RX J1713.7–3946 (Koyama et al., 1997), RCW 86 (Bamba et al., 2000) and others (Bamba et al., 2005). In addition, TeV γ–ray have also been detected from some SNRs. The radiation of TeV γ-ray is explained by (1) Inverse-Compton scattering (IC) of cosmic microwave background photons by the same high energy electron giving rise to the X-ray synchrotron emission, (2) non-thermal bremsstrahlung by high energy elections or (3) the decay of neutral pions that are generated by collisions between high energy protons and dense interstellar matter. Thus, the detection of TeV γ-ray is a direct evidence of acceleration of electrons and/or protons, although TeV γ-ray observation can not distinguish the particle of which originates emission.

Synchrotron X-ray from SNRs is the powerful tool to study the cosmic-ray acceleration processes, because we can probe only on electron acceleration, and X-ray observation have high sensitivity than TeV γ-ray. However, previous studies of cosmic-ray acceleration through synchrotron X-ray concentrated almost on young SNRs, we thus do not know the acceleration in older system. In other words, we do not understand the time history of cosmic-ray acceleration in SNRs. In order to study that, what necessary for are;

1. Discovery of synchrotron X-ray emission from not only historical, young SNRs, but also middle-aged SNRs.

2. To probe the time development of synchrotron X-ray luminosity

Proton acceleration history can be traced by using accelerated electron evolution.

In addition to that, to reveal what sort of conditions are necessary for SNRs to accelerate particles is useful for cosmic-ray acceleration study. It may be brought about by searching thermal X-ray emission, since the thermal emission provides us a lot of information on the environment such as temperature, density, and age of the plasma.

In this thesis, we study on cosmic-ray acceleration history by using observational result of synchrotron X-ray from young and middle-aged SNRs. In Chapter 2 and 3, we review the current understandings of physical processes on cosmic-ray acceleration, and the nature of SNRs. Chapter 4 is the summary of the basic characteristics of the instrument onboard *XMM-Newton*, *Suzaku* and *Chandra* X-ray satellite we used in this work. Results of our analyses of two SNRs W28 and CTB37B, from which TeV γ-ray were detected, are presented in Chapter 5 and 6. We discuss the cosmic-ray acceleration history with a sample of SNRs with synchrotron X-ray including our new result in Chapter 7. Finally, a summary of this thesis is given in Chapter 8.

Chapter 2

The Acceleration of Cosmic rays

2.1 Cosmic rays

Cosmic rays were discovered by Victor Hess in 1912. He measured the ionization level of the atmosphere up to 5 km altitude on a balloon and found that some radiation must come from space to explain the ionization state of the atmosphere. Cosmic rays are mainly composed of protons (90%) and α particles (9%). The energy density is $\sim$1 eV cm^{-3}, which is one of the main forms of energy in our Galaxy. However, the origin of the cosmic rays are yet unknown. In this section, we summarize the properties of the cosmic rays.

2.1.1 Energy Spectrum

Figure 2.1 shows the differential energy spectrum of the cosmic rays. The spectrum is almost power-law like and featureless with the 2 breaks at $\sim 10^{6.5}$ GeV and $\sim 10^{9}$ GeV, which are called "knee" and "ankle", respectively. The spectrum up to 10^9 GeV can be expressed as:

$$\frac{dN}{dE} \propto \begin{cases} E^{-2.7} & (E < E_{\rm knee}), \\ E^{-3.1} & (E_{\rm knee} < E < E_{\rm ankle}) \ . \end{cases} \tag{2.1}$$

It is believed that the particles up to $\sim E_{\rm knee}$ are accelerated in our Galaxy, mainly at the shock waves of supernova remnants (SNRs) (Ginzburg & Syrovatskii, 1964), on the grounds of the chemical composition and the energy budget of cosmic-ray as we discuss below. The particles with such energy are thought to be confined in our Galaxy because the gyro radii of the particles are smaller than the thickness of Galaxy. The origin of more high energy particle is believed to be extragalactic sources.

2.1.2 Chemical Composition

Chemical compositions of cosmic rays and solar particles are shown in figure 2.2. Cosmic rays consist of not only proton but also heavy elements. This suggests that rich metals are comprehended in the cosmic ray acceleration site. The abundances with even atomic numbers are larger than those with odd number for both cosmic rays and solar. On the other hand, cosmic rays are significantly overabundant in Li, Be, F, Sc, Ti, V, Mn, and Ni. Since these elements are not produced in the stellar evolution, it is thought that they

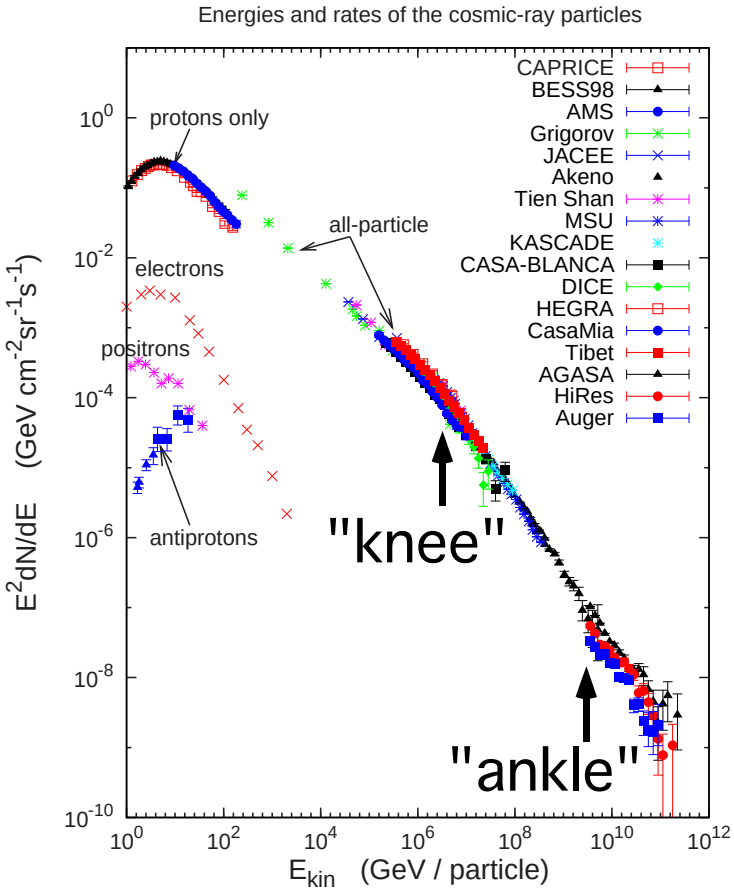

Figure 2.1: Energy spectrum of cosmic rays (Gaisser, 2006)

are produced by inelastic interaction of cosmic rays with the interstellar matter. The column density along the pass of cosmic rays is 5–10 g cm^{-2}, using the cross sections of the spallation. The travel distance of cosmic rays is estimated to be ∼1000 kpc with a ISM density of 1 cm^{-3}. This is much longer than the size of our Galaxy. Hence, cosmic rays are confined by the galactic magnetic field.

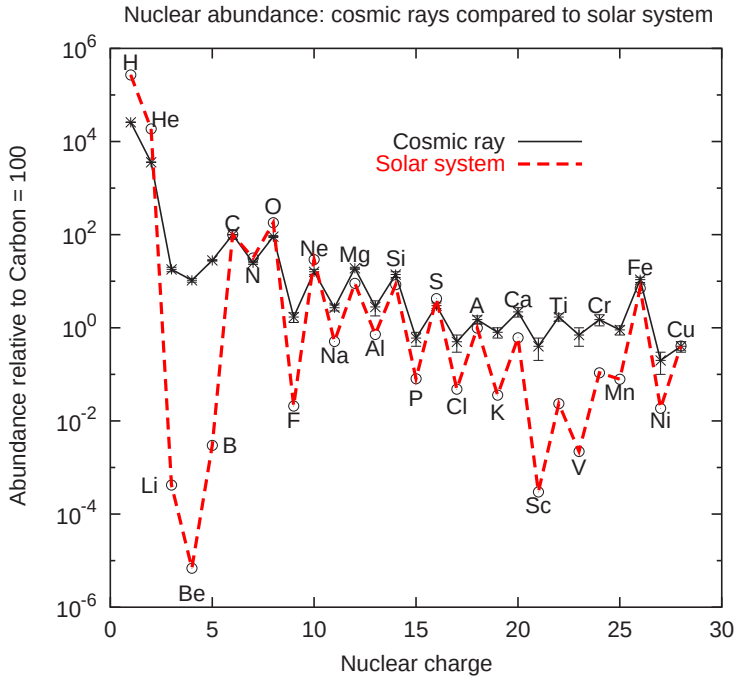

Figure 2.2: Chemical composition of cosmic rays (Gaisser & Stanev, 2006). The horizontal axis is nuclear charge, and the vertical axis is abundance relative to carbon = 100. Crosses represent cosmic ray, and circles show solar abundances, respectively.

2.1.3 Energy Budget

Let us consider the energy supply to cosmic rays ($L_{\rm CR}$). On the assumption that the life time of cosmic rays is determined mainly by the escape from our Galaxy, the energy can be described by using the life time $t_{\rm CR}$, the energy density $\epsilon_{\rm CR}$, and the volume filled by cosmic rays $V_{\rm gal}$;

$$L_{\rm CR} = \frac{V_{\rm gal}\,\epsilon}{t_{\rm CR}} \ . \tag{2.2}$$

The volume is approximated as

$$\begin{aligned} V_{\rm gal} &\simeq \pi \times r_{\rm gal}^2 \times d_{\rm gal} \\ &\sim \pi \times (15\ {\rm kpc})^2 \times 200\ {\rm pc} \\ &\sim 4 \times 10^{66}\ \ {\rm cm}^3\ , \end{aligned} \tag{2.3}$$

where $r_{\rm gal}$ and $r_{\rm gal}$ are the radius and the thickness of our Galaxy, respectively. The energy density is $\epsilon \sim 1$ eV. The life time of cosmic rays can be estimated with the ratio of radio

isotopes such as ^{10}Be, to be $\sim 6\times10^6$ yr (Garcia-Munoz et al., 1977). As the result, the energy is determined to be $L_{\rm CR} \sim 3 \times 10^{40}$ ergs s^{-1}.

Supernova remnants are the most promising candidate of the cosmic ray accelerator on this point of view. Supernova expansion rate is thought to be $\sim$1 per 30 yr, and the expansion energy is $\sim 10^{51}$ ergs. The energy budget of cosmic ray acceleration, thus, can be explained with supernova remnants if the energy injection rate is $\sim$3 %.

2.2 Diffusive shock Acceleration Theory

The most plausible process of cosmic ray acceleration is a diffusive shock acceleration (DSA) mechanism or the first order Fermi acceleration. This is a compelling theory because the acceleration time scale is shorter thanks to the high efficiency, and the expected spectrum is a power-law with an index of ~ 2 ($dN/dE \propto E^{-2}$), which generally coincides with the observed cosmic ray spectrum. In this section, we introduce the theory of cosmic ray acceleration.

2.2.1 Shock Waves

First of all, we describe general properties of shock wave, because the first order Fermi acceleration is adapted at the shock wave.

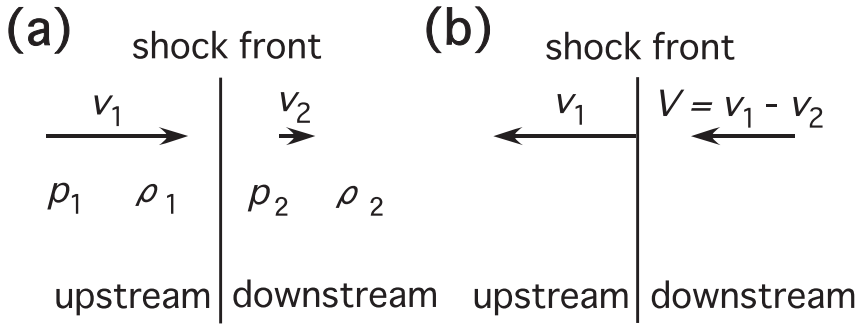

Figure 2.3: Schematic view of the shock front. (a) shock's frame. (b) labo. frame.

Figure 2.3 shows the schematic view and the parameter notations of the shock front. The relations of physical quantities between the upstream and the downstream regions can be obtained from conservation relations of the mass, the energy flux, and the momentum flux as mentioned below (the Rankine-Hugoniot equation) :

$$\rho_1 v_1 = \rho_2 v_2 \ , \tag{2.4}$$

$$p_1 + \rho_1 {v_1}^2 = p_2 + \rho_2 {v_2}^2 \ , \tag{2.5}$$

$$\rho_1 v_1 \left(\frac{1}{2} {v_1}^2 + \frac{u_1 + p_1}{\rho_1} \right) = \rho_2 v_2 \left(\frac{1}{2} {v_2}^2 + \frac{u_2 + p_2}{\rho_2} \right) , \tag{2.6}$$

where u is the internal energy density. By using the sound velocity $C_{\rm s} = \sqrt{\gamma p/\rho}$, where γ is the ratio of specific heats, and the Mach number $M = v/c_{\rm s}$, we can derive the equations of

$$\frac{\rho_2}{\rho_1} = \frac{v_1}{v_2} = \frac{(\gamma+1)M_1^2}{2+(\gamma-1)M_1^2} \ , \tag{2.7}$$

$$\frac{p_2}{p_1} = \frac{2\gamma M_1^2 - (\gamma-1)}{\gamma+1} \ . \tag{2.8}$$

With the equation of state,

$$\begin{aligned} \frac{T_2}{T_1} &= \frac{p_2\rho_1}{p_1\rho_2} \\ &= \frac{[2\gamma M_1^2 - (\gamma-1)][2+(\gamma-1)M_1^2]}{(\gamma+1)^2 M_1^2} \ . \end{aligned} \tag{2.9}$$

We assume that the shock is very strong ($M_1 \gg 1$) and the gas is non-relativistic mono-atomic ($\gamma = 5/3$), the compression ratio r to be

$$r \equiv \frac{\rho_2}{\rho_1} = \frac{v_1}{v_2} \rightarrow \frac{\gamma+1}{\gamma-1} = 4 \ . \tag{2.10}$$

In this case, the temperature in the downstream can also be written as

$$kT_2 = \frac{3}{16}\mu m_{\rm H} {v_1}^2 \ , \tag{2.11}$$

where μ and k are the mean atomic weight and the Boltzmann constant, respectively. The post-shock temperature is determined only by the upstream shock velocity. For example, with the shock velocity of 1000 km s^{-1}, kT_2 becomes 1.0×10^7 K (=1 keV). Since a plasma at this temperature emits X-rays.

2.2.2 Particle Acceleration in Shock Waves

Efficient acceleration can take place when a shock wave propagates through the plasma, and charged particles shuttle between upstream and downstream many times. Figure 2.4 shows a schematic view of particle acceleration around a shock front. Here, we must consider a *collisionless shock wave*. Cosmic plasmas are generally quite thin, and a collision rate of particles is few. Thus, the electric field or the turbulence of the magnetic field (mainly Alfvén wave) play a role as a scattering substance. Now we introduce the theory of DSA with the approach of tracing the behavior of individual particles (Bell, 1978). We assume (i) steady state (ii) plane parallel non-relativistic shock (iii) test particle approximation, i.e. ignoring the reaction of the accelerated particles on the flow. For simplicity, we consider non-thermal particles in relativistic energy.

Let us assume a particle with energy E in the upstream frame of reference. The energy E' in the downstream frame, which move into the downstream gas, can be derived by performing a Lorentz transformation:

$$E' = E + Vp_x \ , \tag{2.12}$$

where $V = v_1 - v_2$ and on the assumption that the shock is non-relativistic. The particle is assumed to be relativistic $E = cp$ and $p_x = (E/c)\cos\theta$, where θ is the angle of particle momentum from the x-axis. Since, the increase of energy becomes

$$\Delta E = E' - E = E\left(\frac{V}{c}\cos\theta\right) \ . \tag{2.13}$$

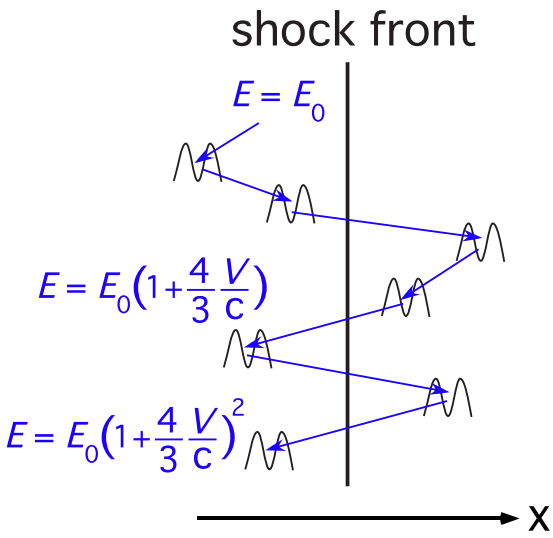

Figure 2.4: Schematic view of the diffusive shock acceleration.

The probability of the particle crossing the shock within the angles θ and $\theta + d\theta$ is

$$p(\theta) = 2 \sin\theta \cos\theta \, d\theta \ . \tag{2.14}$$

The average gain in energy on one round trip across the shock and again is calculated as

$$\left\langle \frac{\Delta E}{E} \right\rangle = 2 \cdot \frac{V}{c} \int_0^{\pi/2} 2\cos^2\theta \sin\theta \, d\theta = \frac{4}{3}\frac{V}{c} \ . \tag{2.15}$$

After n-times round trip, the average energy of the particle becomes

$$\begin{aligned} E_n &= E_0 \left(1 + \frac{4}{3}\frac{V}{c}\right)^n \\ &\approx E_0 \exp\left(\frac{4}{3}\frac{V}{c} n\right) \ , \end{aligned} \tag{2.16}$$

where E_0 is an initial energy. Note that the energy of particles increases exponentially with the number of round trip, n.

In order to obtain the spectrum of accelerated particles, we have to calculate the probability of the particles escaping from the acceleration site per one round trip. The number of particles crossing from upstream to downstream per unit time and unit area is $N\,c\,/\,4$, where N is the number density of particle. Meanwhile, in the downstream, the accelerated particles move with the average velocity of v_2, then the number of particles on the stream is $N\,v_2$. By using these two value, we found the probability of the particles escaping $P_{\rm esc}$ of $(Nv_2)\,/\,(Nc/4) = 4v_2/c$. Therefore, the probability of the particles shuttling between upstream and downstream over n-times is

$$\begin{aligned} P(>n) = (1 - P_{\rm esc})^n &= \left(1 - \frac{4v_2}{c}\right)^n \\ &\approx \exp\left\{-4n\frac{v_2}{c}\right\} \ . \end{aligned} \tag{2.17}$$

With equations of (2.16) and (2.17), the differential energy spectrum of accelerated particles is derived as

$$\frac{dN}{dE} \propto E^{-\frac{3v_2}{V}-1} = E^{-\frac{r+2}{r-1}} \ . \tag{2.18}$$

The spectral index of accelerated particles depends only on the compression ratio r. As mentioned in §2.2.1, r reaches 4 when the shock is strong with infinite Mach number and the gas is monoatomic. In this case, the spectral index becomes 2. This result is very important since it agrees well with the observed cosmic-ray spectrum.

2.2.3 Maximum Energy with Acceleration

Next we consider that how particles obtain energy by the diffusive shock acceleration. The acceleration time scale is

$$t_{\rm acc} = \Delta t \left\langle \frac{E}{\Delta E} \right\rangle \ , \tag{2.19}$$

where Δt is the time needed for one round trip. Δt is the sum of the time for which particles stay in the upstream and downstream regions, and calculated to be (Takahara, 2002)

$$\Delta t = \frac{4D_1}{v_1 c} + \frac{4D_2}{v_2 c} \ , \tag{2.20}$$

where D_1 and D_2 stand for the diffusion coefficients in the upstream and the downstream, respectively. $\langle E/\Delta E \rangle$ is $(3/4)(c/V)$ (see eq. (2.15)). Then, the acceleration time scale is

$$t_{\rm acc} = \frac{3}{V}\left(\frac{D_1}{v_1} + \frac{D_2}{v_2}\right) \ . \tag{2.21}$$

In order to estimate $t_{\rm acc}$, we have to know the diffusion coefficients, D_1 and D_2. The diffusion of the high energy particles are caused by the scattering with turbulence of magnetic fields such as Alfvén wave, and the coefficient is generally expressed as (Skilling, 1975)

$$D = \frac{c r_g}{3}\left(\frac{B}{\delta B}\right)^2 \equiv \frac{1}{3}\, r_g\, c\, \xi, \tag{2.22}$$

$$\xi \sim \left(\frac{B}{\delta B}\right)^2 , \tag{2.23}$$

where r_g is gyroradius ($\equiv pc/ZeB$) and ξ (≥ 1) is the so-called gyrofactor, which represents the largeness of the magnetic field turbulence. ξ is also described with the ratio of the mean free path l_{mfp} / r_g. The smallest possible value of $\xi = 1$ (so-called Bohm limit) corresponds to the case of the most efficient acceleration. By using equations (2.21) and (2.22) together with $v_{\rm s} = v_1 = 4v_2$, we obtain

$$t_{\rm acc} = \frac{20}{3}\frac{c r_g}{v_{\rm s}^2}\xi \ , \tag{2.24}$$

with $D_1 = D_2$ for simplicity. Note that the gyroradius is proportional to the particle energy, hence it takes more time to accelerate particles up to higher energy.

Now, we evaluate the maximum energy of accelerated particles at the shock wave of supernova remnants. The maximum energy of proton can be estimated assuming that

the acceleration time scale is equal to the age of acceleration site. We use the age of an SNR $t_{\rm age}$ as the acceleration time scale $t_{\rm acc}$. With the gyro radius of $r_g = E/ZeB$, the maximum energy in age-limit case is obtained to be

$$\begin{aligned} E_{\rm max,age} &= \frac{3}{20}\frac{1}{\xi}\frac{{v_{\rm s}}^2}{c} Z\,e\,B\,t_{\rm age}\ , \\ &= \frac{4.8\times10^2}{\xi}\left(\frac{v_{\rm s}}{10^8\ {\rm cm\,s^{-1}}}\right)^2\left(\frac{B}{10\ \mu{\rm G}}\right)\left(\frac{t_{\rm age}}{10^5\ {\rm yr}}\right)\ \ [{\rm TeV}]\ , \end{aligned} \tag{2.25}$$

with Z=1.

On the other hand, electrons lose their energy faster than protons, via several processes shown in figure 2.5, thus the maximum electron energy depends on whether the SNR age is shorter than the energy loss time scale or not. The energy loss time scale of accelerated high energy electrons is mainly determined by the synchrotron radiation loss time scale in the case of SNR shocks (the loss via inverse Compton scattering can be ignored because the photon density is low enough in SNRs). The radiation power by synchrotron with a relativistic electron can be written as:

$$\begin{aligned} P &= \frac{4}{3}\,\sigma_{\rm T}\,c\,\beta^2\,\gamma^2\,\frac{B^2}{8\pi} \\ &\simeq \frac{4}{3}\,\sigma_{\rm T}\,c\,\frac{E^2}{m_{\rm e}^2c^4}\,\frac{B^2}{8\pi} \\ &= 1.6\times10^{-3}\,E^2\,B^2\ \ [{\rm ergs/s}]\ , \end{aligned} \tag{2.26}$$

where $\sigma_{\rm T}, \beta, \gamma, m_{\rm e}$ are the Thomson cross section ($=8\pi r_0^2/3$), the electron velocity relative to the light speed (v/c), the Lorentz factor, and the electron mass, respectively (Rybicki & Lightman (1986); the detail of synchrotron radiation process is discussed in the next section). The time scale $t_{\rm loss}$ that the electron lose its energy by 1/e via synchrotron radiation is thus obtained to be

$$\begin{aligned} t_{\rm loss} &= \frac{E}{P} = 6.3\times10^2\,E^{-1}\,B^{-2}\ \ [{\rm s}] \\ &= 1.25\times10^4\left(\frac{E}{10\ {\rm TeV}}\right)^{-1}\left(\frac{B}{10\mu{\rm G}}\right)^{-2}\ \ [{\rm yr}]\ . \end{aligned} \tag{2.27}$$

Electrons with higher energy, or in higher magnetic field lose energy faster. The maximum energy in loss-limited case can be derived by using eq.(2.25) and (2.27) as

$$E_{\rm max,loss} = \frac{24}{\xi^{1/2}}\left(\frac{v_{\rm s}}{10^8\ {\rm cm\,s^{-1}}}\right)\left(\frac{B}{10\ \mu{\rm G}}\right)^{-1/2}\ \ [{\rm TeV}]\ . \tag{2.28}$$

In the case of $t_{\rm age}<t_{\rm loss}$, the maximum electron energy is described with eq.(2.25).

2.3 Radiation from Accelerated Particles

2.3.1 Synchrotron Radiation

Charged particles emit synchrotron radiation by interaction with magnetic field. The power of synchrotron radiation per unit frequency from a single electron of energy E and

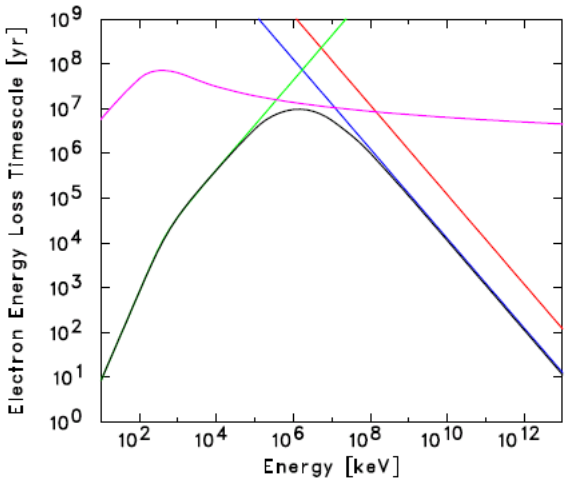

Figure 2.5: Electron energy loss time scales due to synchrotron radiation (blue), inverse Compton scattering (red), bremsstrahlung (magenta) and Coulomb collisions (green), for $n_{\rm H} = n_{\rm e} = 1$ cm^{-3} and $B = 10$ μG.

charge e is

$$P(\omega; E) = \frac{\sqrt{3}}{2\pi} \frac{e^3 B \sin\alpha}{m_{\rm e} c^2} F\left(\frac{\omega}{\omega_c}\right) \ , \tag{2.29}$$

where α is the angle between the velocity of the electron and the magnetic field, $F(x)$ is a dimensionless function given by Figure 6.6 of Rybicki & Lightman (1986) from which has a peak at $\omega/\omega_c \simeq 0.29$, and ω_c is the characteristic frequency described as

$$\omega_c = \frac{3}{2} \frac{eB \sin\alpha}{m_{\rm e} c} \gamma^2 \ . \tag{2.30}$$

The typical energy of synchrotron photon is

$$\begin{aligned} \varepsilon = h\nu_{\rm synch} &= 0.29\, h\omega_{\rm c} \\ &\sim 1.2 \left(\frac{B}{1\mu{\rm G}}\right) \left(\frac{E_{\rm e}}{100\,{\rm TeV}}\right)^2 \quad [{\rm keV}] \, . \end{aligned} \tag{2.31}$$

Electrons with energy of ∼10 GeV in $\sim \mu$G magnetic field radiate synchrotron photon in the radio band. When electrons have the energy of ∼TeV, photon energy becomes ∼keV.

An integration of equation (2.29) over ω gives the total emitted power of

$$P_{\rm sync} = \frac{4}{3} \sigma_{\rm T} c \beta^2 \gamma^2 U_B \ , \tag{2.32}$$

where $\sigma_{\rm T}$ is the Thomson cross section and U_B is the magnetic energy density ($=B^2/8\pi$).

In order to calculate the spectrum of synchrotron radiation from a distribution of electrons, we assume a electron distribution with power-law expressed in the form of

$$N_{\rm e}(E)\, dE = C E^{-p}\, dE \ . \tag{2.33}$$

The total radiated power per unit volume per unit frequency is obtained by the integration of single particle synchrotron radiation formula (eq. 2.29) times electron distribution (eq. 2.33) over all energies. Therefore, the spectrum can be written as

$$\begin{aligned} P_{\rm tot}(\omega) &= \int_0^\infty P(\omega; E) N_{\rm e}(E)\, dE \\ &= \frac{\sqrt{3}}{2\pi} \frac{e^3 C}{m_{\rm e} c^2} \left(\frac{3ec}{(mc^2)^3} \right)^{(p-1)/2} \frac{\Gamma\left(\frac{p}{4} + \frac{19}{12}\right) \Gamma\left(\frac{p}{4} - \frac{1}{12}\right)}{p+1} (B \sin\alpha)^{(p+1)/2} \omega^{-(p-1)/2} \\ &\propto B^{(p+1)/2}\, \omega^{-(p-1)/2} \,, \end{aligned} \tag{2.34}$$

where $\Gamma(y)$ is the gamma function of argument y. The spectral index of synchrotron emission of electrons is related to the electron distribution index p by

$$s = \frac{p-1}{2} \,, \tag{2.35}$$

and the photo index Γ of a power low of the synchrotron spectrum, defined by $I(\epsilon) \propto \epsilon^{-\Gamma}$ is

$$\Gamma = \frac{p+1}{2} \,. \tag{2.36}$$

In the case that an electron spectral index p is 2, the photon index of synchrotron emission becomes 1.5.

2.3.2 Non-thermal Bremsstrahlung

Bremsstrahlung is the radiation associated with the accelerated electrons in the electrostatic fields of ions and the nuclei of atoms. Now we assume relativistic limit. The radiation intensity from a electron with energy E is

$$I(\nu\,; E) = \frac{16}{3} \frac{Z^2 n_{\rm p} e^6}{(m_{\rm e} c^2)^2} \ln\left(\frac{b_{\rm max}}{b_{\rm min}} \right) \theta(E - h\nu), \tag{2.37}$$

where $n_{\rm p}$ is the number density of the plasma, and $+Ze$ is the charge of plasma particle. The function $\theta(E - h\nu)$ is defined as

$$\theta(E - h\nu) = \begin{cases} 1 & (\, E > h\nu \,) \\ 0 & (\, E < h\nu \,) \,. \end{cases} \tag{2.38}$$

$b_{\rm max}$ and $b_{\rm mim}$ are collision parameters with

$$\begin{aligned} b_{\rm max} &= 1.4\, a_0 Z^{-1/3} \quad , \quad b_{\rm min} = \frac{\hbar}{m_e c} \\ a_0 &= \frac{\hbar^2}{m_e e^2} = 0.5293 \times 10^{-8} {\rm cm} \,. \end{aligned} \tag{2.39}$$

Then, equation (2.37) is rewritten to be

$$\begin{aligned} I(\nu\,; E) &= A\, \theta(E - h\nu) \\ A &= \frac{16}{3} \frac{Z^2 n_{\rm p} e^6}{(m_{\rm e} c^2)^2} \ln\left(\frac{1.4 a_0 m_{\rm e} c}{\hbar Z^{\frac{1}{3}}} \right) \,. \end{aligned} \tag{2.40}$$

The number of radiated photons per unit time from a electron with the energy of E is

$$\psi(\varepsilon\,;E)\,d\varepsilon = \frac{I(\nu\,;E)}{h\nu}\,d\nu \equiv \frac{A\,\theta(E-\varepsilon)}{h}\,\frac{d\varepsilon}{\varepsilon}\ , \tag{2.41}$$

where $\varepsilon = h\nu$. Here we take the electron power-law distribution which is the same as synchrotron radiation (eq. 2.33). The emissivity of the photon which has energy over ε_0 is expressed as

$$\begin{aligned} J_\gamma(>\varepsilon_0) &= \int_{\varepsilon_0}^{\infty} d\varepsilon \int_0^{\infty} dE\, N_{\rm e}(E)\,\psi(\varepsilon\,;E) \\ &= \frac{CA}{h(p-1)^2}\varepsilon_0^{1-p}\ . \end{aligned} \tag{2.42}$$

The photon spectrum can be obtained by the derivation of emissivity with photon energy,

$$N(\varepsilon) = -\frac{dJ_\gamma}{d\varepsilon} = \frac{CA}{h(p-1)}\,\varepsilon^{-p}\ . \tag{2.43}$$

What we found here is a photon index of bremsstrahlung coincides with the electron number index,

$$\Gamma = p\ . \tag{2.44}$$

2.3.3 Inverse Compton Scattering

High energy electrons scatter low-energy photons or seed photons up to high energy via Compton scattering. In the case of SNRs, almost seed photons have the CMB origin. The total power of inverse Compton scattering from a single electron is

$$P_{\rm IC} = \frac{4}{3}\sigma_T c\beta^2\gamma^2 U_{\rm ph}\ , \tag{2.45}$$

$$U_{\rm ph} \equiv \int \epsilon v\,d\epsilon\ , \tag{2.46}$$

where $U_{\rm ph}$ is the energy density of seed photons. This formula is valid only for the Thomson regime ($\gamma\epsilon_0 \ll m_{\rm e}c^2$). Comparing with the synchrotron power $P_{\rm sync}$ (eq. 2.32), we have the general result

$$\frac{P_{\rm sync}}{P_{\rm IC}} = \frac{U_{\rm B}}{U_{\rm ph}}\ , \tag{2.47}$$

that is, the radiation losses due to synchrotron emission and to inverse Compton effect are in the same ratio as the magnetic field energy density and photon energy density. In the constant $U_{\rm ph}$ case, such as the upscattered photons being CMB, we can determine the strength of magnetic field directly comparing $P_{\rm sync}$ and $P_{\rm IC}$.

The number of photons scattered per unit time is $c\sigma_T n_{\rm ph}$. Dividing equation (2.45), the average energy of the scattered photons is given by

$$\bar{\epsilon} = \frac{4}{3}\gamma^2\epsilon_0\ , \tag{2.48}$$

where we set $\beta = 1$. For example, when an electron of 5 TeV ($\gamma = 10^7$) scatter a CMB photon ($\epsilon_0 = 2.7$ K $= 2.3{\times}10^{-4}$ eV), the scattered photon energy can be calculated as 10 GeV using this equation.

The spectrum of the inverse Compton scattering is calculated by Jones (1968) as

$$q(\epsilon) = \int d\epsilon_0\, n(\epsilon_0) \int d\gamma N(\gamma) C(\epsilon, \gamma, \epsilon_0) \ , \tag{2.49}$$

where $n(\epsilon_0)$ is the differential spectrum of seed photons and $N(\gamma)$ is the differential spectrum of electron. $C(\epsilon, \gamma, \epsilon_0)$ is the Compton kernel by Jones (1968):

$$C = \frac{2\pi r_{\rm e}^2 c}{\gamma^2 \epsilon_0} \left[2\kappa \ln \kappa + (1+2\kappa)(1-\kappa) + \frac{(4\epsilon_0\gamma\kappa)^2}{2(1+4\epsilon_0\gamma\kappa)}(1-\kappa) \right] \ , \tag{2.50}$$

$$\kappa = \frac{\epsilon}{4\epsilon_0\gamma(\gamma-\epsilon)} \ . \tag{2.51}$$

2.3.4 π^0–Decay Emission

As mentioned in §2.1, the main component of cosmic rays is proton. Accelerated high energy protons produce π^0 mesons when they collide with other protons in interstellar matter such as molecular clouds. γ–rays are emitted by decay of these π^0 mesons. The decay is summarized as

$$p + p \longrightarrow p + p + \pi_0 \longrightarrow p + p + \gamma + \gamma \ . \tag{2.52}$$

To produce π^0-mesons, the kinetic energy of protons should exceed $E_{kin} = 2m_\pi c^2(1 + m_\pi/4m_{\rm p}) \approx 280$ MeV. The π^0-mesons decay to two γ–rays with the mean lifetime of $t_{\pi^0} = 8.3\times10^{-17}$ sec, which is significantly shorter than the lifetime of charged π-mesons ($t_{\pi^{+,-}} = 2.6 \times 10^{-8}$ sec).

Here we assume the collision of protons at rest and with energy $E = \sqrt{p^2c^2 + m_{\rm p}^2c^4}$. The energy at a center-of-mass frame is

$$W = \sqrt{(E + m_{\rm p}c^2)^2 - p^2c^2} = \sqrt{2m_{\rm p}c^2(E + m_{\rm p}c^2)} \ . \tag{2.53}$$

While the energy of γ–ray at a labo. frame is expressed as

$$h\nu = \gamma h\nu_0 \ , \tag{2.54}$$

where $h\nu_0$ is the energy of γ–ray at a center-of-mass frame, which is proportional to W ($h\nu_0 = \eta W$). The relative velocity between a center-of-mass frame and a labo. frame is $c\beta = pc^2/(E + m_{\rm p}c^2)$. Then, we can obtained the γ–ray energy at a labo. frame approximately,

$$h\nu \approx \sqrt{\frac{E + m_{\rm p}c^2}{2m_{\rm p}c^2}}\, \sqrt{2m_{\rm p}c^2(E + m_{\rm p}c^2)}\, \eta \approx \eta E \ . \tag{2.55}$$

The energy of γ-ray produced by the decay of π^0-mesons are proportional to the proton energy. η is known to be $h\nu \approx 0.1E$, based on a experimental result. In order to calculate the total radiated energy, we use a proton distribution of $N_{\rm p}(E_{\rm p})\, dE_{\rm p} = CE_{\rm p}^{-p}\, dE_{\rm p}$. The total energy is

$$\begin{aligned} F_\nu\, d\nu &= \int (0.1E_{\rm p}) C E_{\rm p}^{-p}\, dE_{\rm p} \\ &= \int Ch(10h\nu)^{1-p} d\nu \ , \\ F_\nu &\propto \nu^{1-p}. \end{aligned} \tag{2.56}$$

Then, the photon index of π^0 decay emission corresponds to the number index of protons,

$$\Gamma = p \ . \tag{2.57}$$

Note that this photon index is only between low and high energy cut-off range. The low energy cut-off is half of the mass of π-mesons (70 MeV), and the high energy cut-off is determined with the maximum proton energy.

The cooling timescale of protons due to this process is (Aharonian & Atoyan, 1996)

$$t_{\rm pp} = \frac{1}{n_{\rm H}\sigma_{\rm pp} f c} \ , \tag{2.58}$$

where f is the coefficient of inelasticity. $\sigma_{\rm pp}$ is the total cross section of inelastic pp collisions, which can be approximated by

$$\sigma_{\rm pp}(E_{\rm p}) \approx 30\,[\,0.95 + 0.06\,\ln\left((E_{\rm p} - m_{\rm p}c^2)/1{\rm GeV}\right)]{\rm mb} \ . \tag{2.59}$$

Since $\sigma_{\rm pp}(E_{\rm p})$ shows small energy-dependency above 1 GeV (see equation (2.59)), $t_{\rm pp}$ is almost constant at $\simeq 6 \times 10^7 (n_{\rm H}\,/\,1\,{\rm cm}^{-3})^{-1}$ year in the high energy region. Therefore, the initial spectrum of accelerated protons remains unchanged.

We note that the secondary electron, which is produced by the decay of π^--mesons, also emit synchrotron radiation, non-thermal bremsstrahlung, or inverse Compton scattering. The decay is summarized as

$$p + n \longrightarrow p + p + \pi^- \longrightarrow p + p + \mu^- + \bar{\nu_\mu} \longrightarrow p + p + e^- + \bar{\nu_e} + \nu_\mu \ . \tag{2.60}$$

Chapter 3

Review of Supernova Remnants

As discussed in chapter 1, supernova remnants (SNRs) are the candidates of cosmic ray accelerators. SNRs are born by the explosion of stars with the energy release of $\sim 10^{51}$ ergs. The shock wave is formed by the explosion, and swept up the interstellar medium (ISM). A SNR expands as a shell within the ISM for thousands of year. It is believed that a supernova explosion occurs per ∼30 year in out Galaxy. Until now, 274 SNRs are discovered in our Galaxy (Green, 2009). In this section, we introduce the characteristics and the evolution of SNRs, and the process of thermal X-ray emission from SNRs.

3.1 Classes of Supernovae

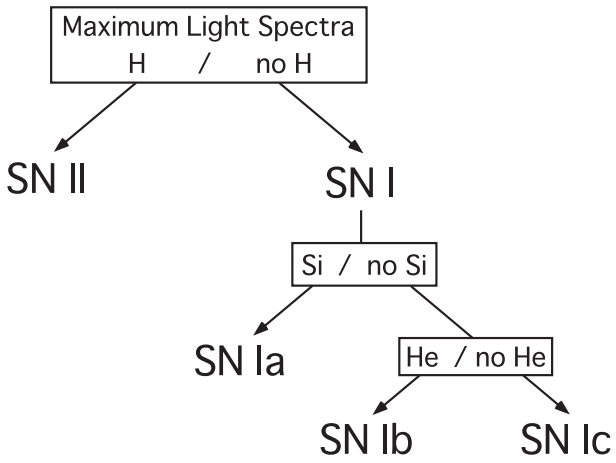

Figure 3.1: The basic classification scheme for SNe based on spectral features at early times

Supernovae (SNe) are classified on the basis of observational optical spectra near the maximum light as shown in Figure 3.1. The spectra of Type Ia SNe have no H lines and have little difference between objects, whereas those of Type II have H lines and have strong characteristic. Type Ia SNe are also classed into two subclasses depending on whether the Si absorption feature exists (Type Ia) or not (Type Ib or Ic). Type Ib spectra have the He absorption, in contrast, Type Ic does not have neither H, Si, nor He line.

After a half year from the maximum light, the spectra of SNe are composed of only emission lines because of the rarity due to expansion. The main component of Type Ia SNe is Fe, and of other Types are O and Ca, respectively. In addition, Type Ia SNe were observed in every galaxy, meanwhile others were discovered only from star forming galaxies. All these facts suggest that the progenitors of Type Ia SNe are mass accreting white dwarfs (WDs), and others are identified as core collapsed explosion of massive stars ($M \geq 8M_{\odot}$). The total released energy of Type Ia SN is estimated to be 1.3×10^{51} erg. A Core collapsed SN releases their energy of 10^{53} erg, then 99% of them are used into diffusion of neutrinos, and other 1% of 10^{51} erg become kinetic energy.

3.2 Evolution of SNRs

A supernova explosion forms SNR in interstellar space. Here we introduce the evolution of SNRs.

3.2.1 Free Expansion Phase

The density of ISM is much smaller than of the gas which originally composed the star (ejecta). Hence, the initial phase of evolution is characterized by the free expansion of ejecta. Most of the explosion energy is released kinetically, while 2–3% of the energy converted into the thermal energy. The average velocity of the ejecta V_0 is

$$V_0 = \sqrt{\frac{2E}{M_0}} = 3.2 \times 10^8 \left(\frac{E}{10^{51}\ \mathrm{erg}}\right)^{1/2} \left(\frac{M_0}{10M_{\odot}}\right)^{-1/2} \ [\mathrm{cm\,s^{-1}}] \ , \tag{3.1}$$

where E, M_0, $M_{\odot}$ are the total explosion energy, the mass of ejecta, and the mass of Sun ($M_{\odot} = 2 \times 10^{33}$ g), respectively. The velocity is much larger than the sound speed in the ambient gas and is preceded by a shock wave (the blast-wave shock). The blast-wave shock expands without deceleration, and the time dependence of the radius $R(t)$ of

$$R(t) \propto t \ . \tag{3.2}$$

The blast-wave push the ambient matter outward, then the ejecta is retarded by the reaction. This deceleration is caused by the occurrence of shock in the ejecta, which is called as "reverse shock".

At the end of this phase, the swept up mass by the blast wave (M_s) becomes comparable to that of the ejecta mass (M_0). The radius and the age of the remnant at this stage is derived as

$$R_s^0 = \left(\frac{3M_0}{4\pi\rho_0}\right)^{1/3} = 4.6 \left(\frac{M_0}{10M_{\odot}}\right)^{1/3} \left(\frac{n_0}{1\,\mathrm{cm^{-3}}}\right)^{-1/3} \ [\mathrm{pc}] \ , \tag{3.3}$$

and

$$t_s^0 \approx \frac{\sqrt{2}R_s}{V_0} = 6.3 \times 10^{10} \left(\frac{E}{10^{51}\,\mathrm{erg}}\right)^{-1/2} \left(\frac{M_0}{10M_{\odot}}\right)^{5/6} \left(\frac{n_0}{1\,\mathrm{cm^{-3}}}\right)^{-1/3} \ [\mathrm{s}] \ , \tag{3.4}$$

where ρ_0 [g cm^{-3}] and n_0 [cm^{-3}] are the ambient densities. The free expansion phase continues $\sim$1000 yr from the explosion and the radius becomes $\sim$5 pc in the average n_0 of $\sim$1 cm^{-3}.

3.2.2 Adiabatic Phase (Sedov Phase)

When the swept up mass becomes larger than the ejecta mass, the SNR evolution moves into an adiabatic expansion phase, since the radiative cooling is still negligible. The evolution can be written as the results of the similarity solution of a point explosion (Sedov, 1959). The condition can be characterized by using only the expansion energy (E), the density of ISM (ρ_0), and the age (t). We can define a non-dimensional parameter ξ as

$$\xi = R \left(\frac{E t^2}{\rho_0} \right)^{-1/5} . \tag{3.5}$$

In the case of that the ISM density has the radius dependence of $\rho_0(r) = Ar^{-m}$, such as massive star which make a density profile of $\propto r^{-2}$ by a stellar wind (Dwarkadas, 2005), eq. (3.5) becomes

$$\xi = R \left(\frac{E}{A} \right)^{-1/(5-m)} t^{-2/(5-m)} . \tag{3.6}$$

Then, the radius of the expanding shell R_s is

$$R_s = \xi_0 \left(\frac{E}{A} \right)^{1/(5-m)} t^{2/(5-m)} , \tag{3.7}$$

where ξ_0 can be determined from the energy conservation equation. The shock velocity is decelerated in nearly uniform density with $m<3$, and is accelerated in high density gradient with $m>3$, from the age index of eq. (3.7). In the case that energy L_0 is emitted per unit time continuously, the radius becomes

$$R_s' = \xi_0' \left(\frac{L_0}{A} \right)^{1/(5-m)} t^{3/(5-m)} , \tag{3.8}$$

which means decelerate with $m<2$, and accelerate with $m>2$.

Using ξ_0=1.17 for ideal gas (γ=5/3) (Landau & Lifshitz, 1959), and m=0 which means uniform ISM density, the radius (R_s), the temperature (T_s), and the velocity of the shock (V_s) are described as

$$R_s = 5.0 \left(\frac{E}{10^{51}\,\mathrm{erg}} \right)^{1/5} \left(\frac{n_0}{1\,\mathrm{cm}^{-3}} \right)^{-1/5} \left(\frac{t_s}{10^3\,\mathrm{yr}} \right)^{2/5} \ [\mathrm{pc}] , \tag{3.9}$$

$$\begin{aligned} T_s &= 1.5 \times 10^{10} \left(\frac{E}{10^{51}\,\mathrm{erg}} \right) \left(\frac{n_0}{1\,\mathrm{cm}^{-3}} \right)^{-1} {R_s}^{-3} \ [\mathrm{K}] \\ &= 1.2 \times 10^8 \left(\frac{E}{10^{51}\,\mathrm{erg}} \right)^{2/5} \left(\frac{n_0}{1\,\mathrm{cm}^{-3}} \right)^{-2/5} \left(\frac{t_s}{10^3\,\mathrm{yr}} \right)^{-6/5} \ [\mathrm{K}] , \end{aligned} \tag{3.10}$$

$$V_s = \frac{dR_s}{dt} = 2.1 \times 10^8 \left(\frac{E}{10^{51}\,\mathrm{erg}} \right)^{1/5} \left(\frac{n_0}{1\,\mathrm{cm}^{-3}} \right)^{-1/5} \left(\frac{t_s}{10^3\,\mathrm{yr}} \right)^{-3/5} \ [\mathrm{cm\,s}^{-1}] . \tag{3.11}$$

Until the end of this stage, about 70% of the initial explosion energy is converted into thermal energy of the swept up interstellar matter (Chevalier, 1974).

3.2.3 Radiative Cooling Phase

The remnant expands adiabatically, the cooling effect behind the shock front becomes unignorable, and the Sedov approximation is broken. The radiative cooling coefficient is a temperature dependence function defined as

$$\Lambda = n_e n_i \Lambda_0(T) \ , \tag{3.12}$$

where $\Lambda_0(T)$ is the radiative cooling function calculated by Gaetz & Salpeter (1983), and so on. Figure 3.2 shows the temperature dependence of $\Lambda(T)$. When the temperature drops around 5.0×10^5 K (∼40 eV), the cooling efficiency becomes large, and the cooling is accelerated.

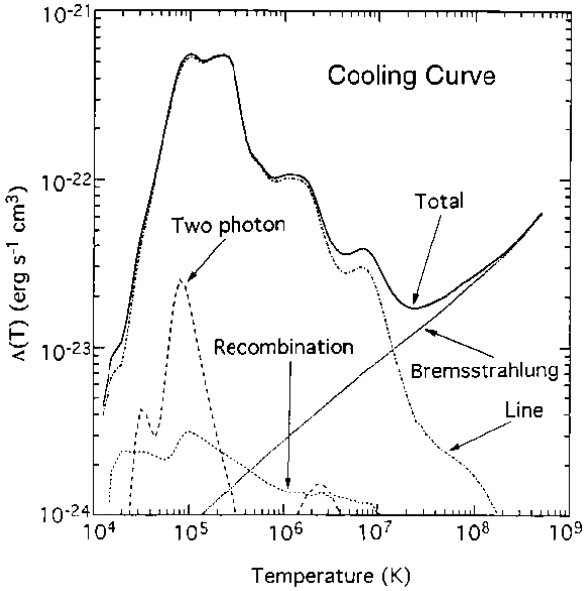

Figure 3.2: Radiative cooling coefficient (Gehrels & Williams, 1993)

At this stage, a cold and dense ISM shell is formed just behind the shock front, whereas a hot rarefied gas fills inside the shell. As the temperature cools down further, the pressure can be ignored and the cool shell expands at a constant radial momentum with the time dependency of $R_s \propto t^{1/4}$.

3.3 Morphologies of SNRs

Morphologies of SNRs are classified into three categories based on their X-ray and radio emission; (i) shell-like SNRs, (ii) Crab-like SNRs, and (iii) mixed-morphology (MM) SNRs.

Shell-like SNRs

This class consists of those in which both the X-ray and radio morphologies are shell-like. Most of the shell-like SNRs have thermal X-ray, from a plasma heated by a shock wave. Some shell-like SNRs emit non-thermal synchrotron emission from radio to X-ray from shock-accelerated electrons. These SNRs are in free expansion phase or adiabatic phase.

Crab-like SNRs

The X-ray and radio morphologies of crab-like SNRs are center-filled. Their energy source is an active rotating pulsar and its nebula. The X-ray spectrum is featureless power-law-like due to synchrotron processes.

MM SNRs

SNRs of this class have centrally peaked X-ray and shell-like radio morphology. Radio emission is non-thermal synchrotron radiation from accelerated electrons as same as shell-like SNRs. The distribution of hot gas, from which emits thermal X-ray, is different from the shape of shell. The trigger of this distribution is still unknown. One suggestion is that the hot gas is provided into SNRs by the integrated interstellar cloud through the heat conduction or shock wave heating.

3.4 Thermal X–ray Emission from SNRs

The shock wave heats the ejecta and ISM about 10^6–10^7 K. Then SNRs emits thermal X–ray from hot plasma of $kT \leq 1$ keV via thermal bremsstrahlung plus line emissions. Several SNRs also emit non-thermal X–ray via synchrotron radiation or non-thermal bremsstrahlung (more details are shown in §2.3). Here we summarize thermal X–ray emission mechanism of SNRs, which tells as the information of environments and conditions of the SNR itself.

3.4.1 Bremsstrahlung

Radiation due to the acceleration of a charge in the Coulomb field of another charge is called *bremsstrahlung* or *free-free emission*. The most intense emission in neutral plasma is the bremsstrahlung from electrons by the Coulomb field of ions. The power of emission from single-speed electrons per unit time, volume, and frequency is given by

$$\frac{dW}{dt\,dV\,d\nu} = \frac{32\pi^2 e^6}{3\sqrt{3}\,c^3 m_e^2 v_e} n_e n_i Z^2 g_{ff}(v,\nu) \ , \tag{3.13}$$

where e, m_e, v_e, n_e, n_i, and g_{ff} are charge unit, electron mass and velocity, density of electron and ion, and Gaunt factor, respectively. The Gaunt factor is a certain function of the energy of the electron and the of the frequency of the emission, which is described as

$$g_{ff}(v,\nu) = \frac{\sqrt{3}}{\pi} \ln\left(\frac{b_{\max}}{b_{\min}}\right) \ , \tag{3.14}$$

where $b_{\max}$ and $b_{\min}$ are collision parameters. The review articles of the Gaunt factor are Bressaard & van de Hulst (1962) and Karzas & Latter (1961).

To calculate the power of *thermal bremsstrahlung*, we average the single-speed expression over a thermal distribution of speeds. When the plasma temperature is kT, the probability dP that a particle has a velocity in the range of $v_e \sim v_e + dv_e$ is estimated under the assumption of an isotropic distribution of velocities to be

$$dP \propto v_e^2 \exp\left(-\frac{m v_e^2}{2kT}\right) dv_e \ . \tag{3.15}$$

Combining these equations, we obtain the emission power of

$$\frac{dW}{dt\,dV\,d\nu} = \frac{32\pi e^6}{3m_e c^3}\left(\frac{2\pi}{3km_e}\right)^{1/2} T^{-1/2} Z^2 n_e n_i e^{-h\nu/kT}\bar{g}_{ff} \ , \tag{3.16}$$

where $\bar{g}_{ff}(T,\nu)$ is a velocity averaged Gaunt factor. Evaluating eq. (3.16) in CGS units, we have for the emission (ergs cm^{-3} s^{-1} Hz^{-1})

$$\varepsilon_\nu^{ff} \equiv \frac{dW}{dt\,dV\,d\nu} = 6.8\times 10^{-38} Z^2 n_e n_i T^{-1/2} e^{-h\nu/kT}\bar{g}_{ff} \ . \tag{3.17}$$

The spectrum of *thermal bremsstrahlung* have cut-off around the temperature of plasma ($h\nu \sim kT$). The temperature of SNRs are almost $\leq$1 keV, thus the spectral index is large (the spectrum is soft) in X-ray band.

The total power per unit volume is obtained from the spectral results by integrating eq. (3.16) over frequency. The result may be stated as

$$\frac{dW}{dt\,dV\,d\nu} = \left(\frac{2\pi kT}{3m_e}\right)^{1/2} \frac{2^5\pi e^6}{3hm_e c^3} Z^2 n_e n_i \bar{g}_B \ , \tag{3.18}$$

or numerically, again in CGS units, the emission (erg s^{-1} cm^{-3}) is

$$\varepsilon^{ff} \equiv \frac{dW}{dt\,dV} = 1.4\times 10^{-27} T^{1/2} n_e n_i Z^2 \bar{g}_B \ . \tag{3.19}$$

Here $\bar{g}_B$ is a frequency average of the velocity averaged Gaunt factor, which is in the range 1.1 to 1.5. Choosing a value of 1.2 will give an accuracy to within about 20%.

The factor $T^{1/2}$ is proportional to a velocity $\langle v\rangle$, then plasmas with higher velocity and higher densities emits bremsstrahlung emission brighter.

3.4.2 Line Emission (Bound–Bound Emission)

The transitions between two discrete quantum levels often accompany photon emission called *line emission* or *bound-bound emission*. One case in which a fairly complete discussion of transition rates can be given purely theoretically is the pure Coulomb case of hydrogen (and for other hydrogen-like ions, such as HeII and LiIII, which have only one trapped electron). The energy of a photon absorbed or emitted in a transition between two discrete levels with principal quantum numbers n and n' is given by

$$E_{bb} = R_y\left(\frac{1}{n^2} - \frac{1}{n'^2}\right) \ , \tag{3.20}$$

where

$$R_y \equiv \frac{e^2}{2a_0} = 13.6 \ \ [\text{eV}] \ . \tag{3.21}$$

For heavy elements, E_{bb} roughly becomes

$$E_{bb} = Z^2 R_y\left(\frac{1}{n^2} - \frac{1}{n'^2}\right) \ . \tag{3.22}$$

Ionized plasma is collisionally excited by electrons. For the first approximation, we can assume that the rate of photon emission is the same as the excitation. Therefore, the line intensity is proportional to $n_e n_i$, which determines the probability of collisions between electrons and ions.

The line energy depends on a degree of ionization, an azimuthal quantum number, and so on. For example, hydrogen-like atoms emit photons with higher energy than that of helium-like ones. Mewe et al. (1985) calculated the line energies for hydrogen- and helium-like lines plus their satellites produced by inner shell transitions.

3.5 Non-Equilibrium Ionization

The density of plasma in SNRs are very low, then the collision rate between ions and electrons is small. As a result, the ionization of matter does not reach the level expected from the electron temperature, and it takes a long time for plasma to reach ionization equilibrium. This is called non-equilibrium ionization (NEI). The characteristic ionization timescale (τ) for plasma to reach ionization equilibrium is given by Masai (1994) as

$$\tau = n_e t \approx 10^{12} \quad [\mathrm{s\,cm^{-3}}]\,, \tag{3.23}$$

where n_e is an electron number density. With typical electron number density of 1 $\mathrm{cm^{-3}}$ in the interstellar medium, shock heated plasmas in SNRs up to ∼30000 yr old are expected to be in non-equilibrium ionization. Note that we must careful about the fact that line emission in an NEI state is different from that in an ionization equilibrium state, because ions in an NEI state capture more electrons compared with those in an ionization state, then the temperature estimated from ionization degree is lower than electron temperature.

3.6 Key Objects for Cosmic-Ray Acceleration study on SNRs

3.6.1 Molecular Clouds

A molecular cloud (MC) is low temperature (∼10 K) and high density ($n[\mathrm{H_2}] \leq 10^2 - 10^3$ $\mathrm{cm^{-3}}$) interstellar cloud. Hence, MC is good target for cosmic-ray protons to emit TeV γ-ray by decay of π^0 mesons, as discussed in §2.3.4.

Inner gas of MC is in a state of molecule. A line emission is caused by a rotation transition of molecules, although low temperature of ∼10 K. However, hydrogen molecule ($\mathrm{H_2}$), which is main component of MC, can not radiates because $\mathrm{H_2}$ have no electrical dipole moment. We generically observe emission lines of carbon monoxide molecules (COs), of which abundance ratio is large next to $\mathrm{H_2}$, with the radio of $\mathrm{CO/H_2} \sim 1/10000$.

We can obtain several physical parameters, such as molecular gas distribution, temperature, density, mass and so on by the observation of MC line emission. In addition, the distance to MC is derived by using the doppler shift measurement of line emission and the rotation curve of galaxy.

The mass of MC is roughly $\leq 10^4 M_\odot$ for dark MC, and $\leq 10^4 M_\odot$ for large MC. Small mass stars with $M \leq 1 M_\odot$ are formed in dark MC, in contrast, OB stars with the mass of $M_\odot \sim$ dozens of $M_\odot$ are built up in large MC. OB stars ionize the around gas, thus $\mathrm{H_{II}}$ region is often accompanied by large MC.

3.6.2 OH Masers

OH (1720 MHz) masers unaccompanied by masing in the 1665 and 1667 MHz main lines occur where SNRs interact with MCs (Frail et al. (1994); Yusef-Zadeh et al. (1996); Green et al. (1997); Wardle & Yusef-Zadeh (2002)). Because, the OH column densities required for the formation of OH (1720 MHz) masers ($\leq 10^{16}$ cm^{-2}) should be sufficient to create detectable thermal OH absorption in the mainline transitions of the OH (1665/1667 MHz) molecule if the background continuum is strong. Thus, the existence of 1720 MHz OH maser is the evidence of interaction with a shock wave and molecular cloud.

Maser stands for Microwave Amplification by Stimulation Emission of Radiation, the microwave-frequency analog of a laser. Amplification occurs in a particular radiative transition of a molecule (or, more generally, an ion or atom) when absorption of photons from the radiation field by molecules in the lower level is dominated by stimulated emission of photons by molecules in the upper state. This requires that the upper state be overpopulated relative to the lower state, a condition referred to as population inversion. When this occurs, seed photons originating from spontaneous emission or background radio sources will be exponentially amplified by stimulated emission, leading to the production of an intense, tightly collimated beam of photons at the frequency of the transition, which is only limited by the rate at which the inversion can be maintained by the processes responsible for the supply of molecules in the upper state.

Chapter 4

Instrument

4.1 *XMM-Newton*

XMM-Newton (Jansen et al., 2001) is a ESA's X-ray observatory lunched on December 10th, 1999. It takes an highly elliptical orbit with an apogee of about 115,000 km and a perigee of about 6000 km. The orbital period of the satellite is about 48 hours.

XMM-Newton carried two distinct types of telescopes: three X-ray telescopes with different X-ray detectors in their foci, and a 30-cm optical/UV telescope with a microchannel-plate pre-amplified chargecoupled devices (CCD) detector in its focal plane.

XMM-Newton provides the following three types of scientific instruments: three X-ray CCD cameras called European Photon Imaging Camera (EPIC), two high-resolution X-ray spectroscopy instruments called the Reflection Grating Spectrometer (RGS), and the Optical Monitor (OM). Three EPIC cameras consist of two different detectors; two MOS cameras and one pn. They provide X-ray imaging, moderate resolution spectroscopy, and X-ray photometry. Since we used only EPIC cameras, characteristics of them and the associated X-ray telescopes are described below.

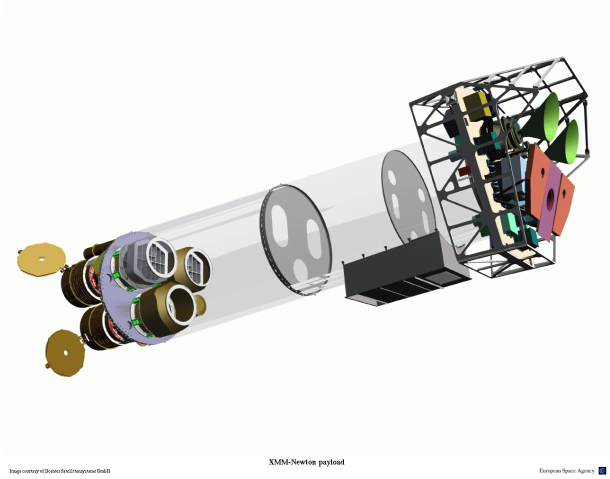

Figure 4.1: Sketch of the *XMM-Newton* payload. The three X-ray mirror modules are visible at the lower left. At the right end of the assembly, the focal X-ray instruments are shown: the EPIC-MOS cameras with their radiators, the radiator of the EPIC-pn camera and those of the RGS detectors.

4.1.1 X-ray Telescopes

Each of the three X-ray telescopes on board *XMM-Newton* consists of 58 Wolter I grazing-incidence gold-coated mirrors which are nested in a coaxial and confocal configuration. The mirror system had to utilize a very shallow grazing angle of 30' in order to provide sufficient reflectivity at high energies. The telescopes focal length is 7.5 meters and the diameter of the largest mirrors is 70 cm. Each telescope consists includes, apart from the mirror modules, baffles for visible and X-ray stray-light suppression and an electron deflector for diverting soft electrons. Two of the telescopes carry a Reflection Grating Array (RGA).

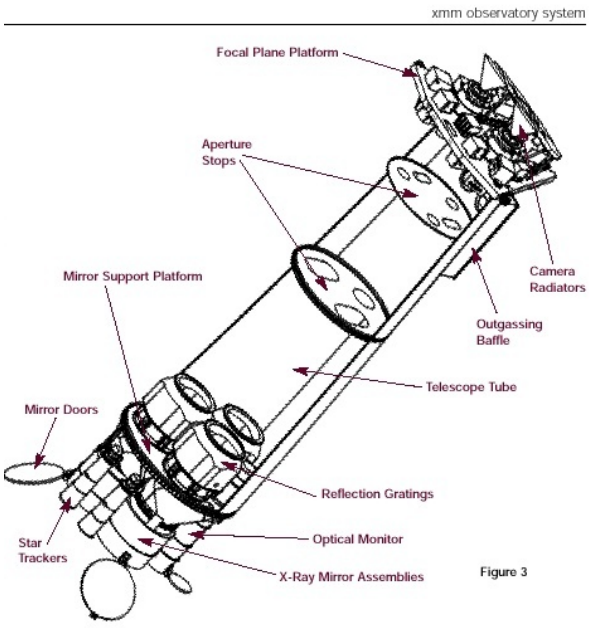

Figure 4.2: Design of the telescope on board *XMM-Newton*

Table 4.1: Specifications and characteristics of the telescopes on board *XMM-Newton*

		MOS1	MOS2	pn
Focal Length			7.5 m	
Field of View			30 ′	
Angular Resolution (HEW of PSF)	at 1.5 keV	13.6 ″	12.8 ″	15.1″
	at 8.0 keV	12.5 ″	12.2 ″	14.8″
Effective Area at 1.5 keV		540 cm^2		1400 cm^2
at 8.0 keV		80 cm^2		570 cm^2

Table 4.1 summarized the specifications and the characteristics of the telescopes. The angular resolutions of the telescopes are ∼15 ″, expressed in terms of half-energy width (HEW). The angular resolution slightly depends on the energy of the incident X-ray. Figure 4.3 shows the on-axis effective area of *XMM-Newton* telescopes. The XMM-Newton mirrors are most efficient in the energy range from 0.1 to 10 keV, with

a pronounced edge near 2 keV (Au M edge). The effective area of each MOS camera is smaller than that of the pn camera, because 44% of the incoming light is directed onto the MOS cameras at the prime foci, and while 40% of the radiation is dispersed onto a linear CCD strips of RGSs. The effective areas decreases with increasing off-axis angle due to the vignetting effect shown in figure 4.4 (a). In addition, The off-axis vignetting in the two telescopes with an RGA has a dependence on angle with respect to the RGAs' dispersion direction. A source at an off-axis position perpendicular to the dispersion direction will be vignetted by a different amount to one at a position parallel to the dispersion direction. This azimuthal dependency of the vignetting is shown in figure 4.4 (b).

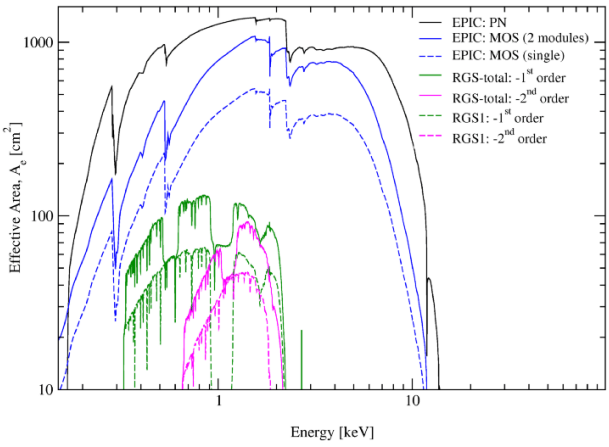

Figure 4.3: The on-axis effective areas of *XMM-Newton* telescopes, combined with the quantum efficiency of the focal X-ray instruments, EPIC and RGS..

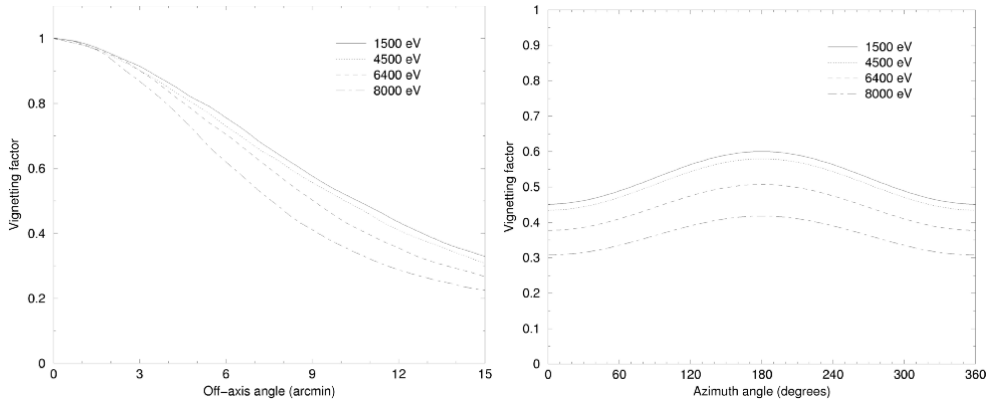

Figure 4.4: The vignetting function of *XMM-Newton* telescopes. (left): The vignetting factor as a function of off-axis angle at a few selected energies, of the X-ray telescope in front of the pn camera. (right): The vignetting effect as a function of azimuth angle of the X-ray telescope in front of the MOS1 camera. The curves are given for an off-axis angle of 10′. Due to the presence of grating assemblies in the beams of the X-ray telescopes, the vignetting functions measured in the MOS cameras are modulated azimuthally.

X-ray stray light in the EPIC is produced by rays which are singly reflected by the

mirror hyperbola and which reach the sensitive area of the camera. An X-ray baffle was implemented to shadow those singly reflected rays.

4.1.2 European Photon Imaging Camera (EPIC)

EPIC cameras are X-ray imagers, consists of two MOS (Metal Oxide Semi-conductor) CCD arrays and one CCD camera called pn. The EPIC cameras offer the possibility to perform extremely sensitive imaging observations over the telescope's field of view (FOV) of 30′ and in the energy range from 0.15 to 15 keV with moderate spectral (EΔ E 20-50) and angular resolution (PSF, 15″ HEW). All EPIC CCDs operate in photon counting mode with a fixed, mode dependent frame read-out frequency, producing event lists. This allows for simultaneous imaging and non-dispersive spectroscopy due to the intrinsic energy resolution of the pixels. In general, X-ray CCD converts an incident X-ray photon into a charge cloud, with the magnitude of charge proportional to the energy of the absorbed X-ray. This charge is then shifted out onto the gate of an output transistor via an application of time-varying electrical potential. Thus, a voltage level (plus height) proportional to the energy of the X-ray photon is read out.

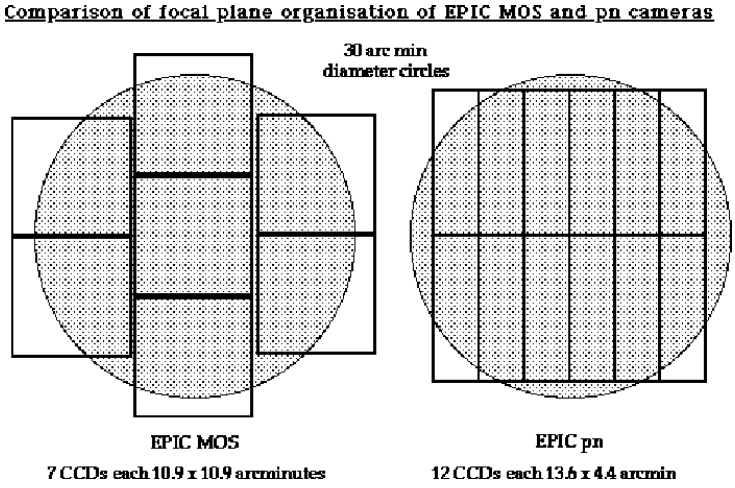

Figure 4.5: Sketch of the FOV of the two types of EPIC cameras; MOS (left) and pn (right). The shaded circles depict 30′ diameter areas.

Table 4.2: Specifications and characteristics of the EPIC MOS and pn

	EPIC-MOS	EPIC-pn
Bandpass	0.15–12 keV	0.15–15 keV
Illumination Method	Front illuminated	Back illuminated
Number of Pixels (1 chip)	600 × 600	378 × 64
Pixel Size	40 μm (1″.1)	150 μm (4″.1)
Thickness of Depletion Layer	30–40 μm	300 μm
Time Resolution (Full Frame Mode)	2.6 s	73.4 ms
Spectral Resolution at 6.4 keV	150 eV	

Figure 4.5 and table 4.2 show the sketch and specifications and characteristics of EPIC MOS and pn, respectively.

The MOS chip arrays consist of 7 individual identical, front-illuminated chips. The central CCD is at the focal point on the optical axis of the telescope while the outer six are stepped towards the mirror by 4.5 mm to follow approximately the focal plane curvature, and improve the focus for off-axis sources. Each chip is equipped with a frame store region. Two MOS cameras are rotated by 90° with respect to each other, in order to compensate for the dead spaces between the chips.

The pn-CCD consists of 12 back-illuminated chips. This realizes high quantum efficiency for the high X-ray photons. Each pixel column of pn chips has its own readout node; 64 channels per chip and a total of 768 channels for the entire camera. This allows much faster readout of the pn camera than the MOS cameras.

The EPIC cameras allow several modes of data acquisition. We used "full frame" mode in this thesis. In this mode, all pixels of all CCDs are read out and thus the full FOV is covered. In addition, Three kinds of the optical blocking filter were mounted for each cameras. These filters are used, because the EPIC CCDs are not only sensitive to X-ray photons, but also to IR, visible and UV light. Therefore, if an astronomical target has a high optical flux, there is a possibility that the X-ray signal becomes contaminated by those photons. Figure 4.6 shows the effective area for each of the optical blocking filters. There is the implication especially in the low energy band.

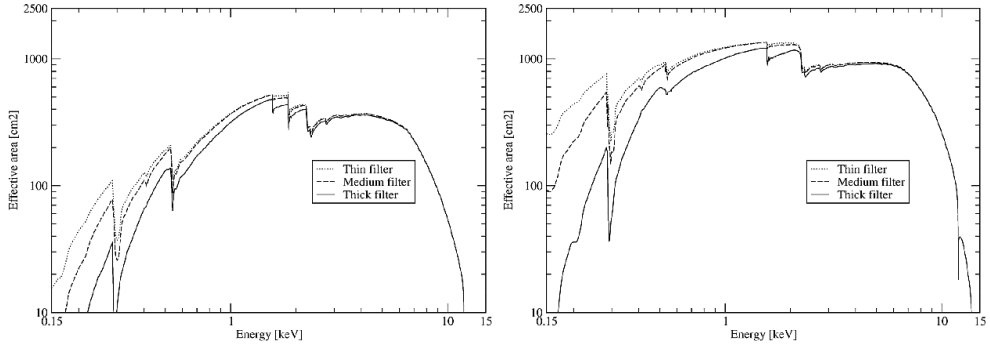

Figure 4.6: EPIC effective area for each of the optical blocking thin, medium and thick filters; MOS (left) and pn (right)

4.2 *Suzaku*

Suzaku (Mitsuda et al., 2007) is the fifth Japanese X-ray astronomy satellite launched on July 10th, 2005. It takes a circular orbit of 570 km altitude. The orbital period is about 96 minutes.

The schematic view of the *Suzaku* spacecraft is shown in figure 4.7. The five sets of X-ray telescopes are mounted on the top of the EOB and five focal plane detectors and a hard X-ray detectors are mounted on the base panel of the spacecraft.

The scientific payload of *Suzaku* initially consisted of two distinct co-aligned detectors: non-imaging collimated detector for high energies called Hard X-ray Detector (HXD; Takahashi et al. (2007); Kokubun et al. (2007)), and four X-ray sensitive imaging CCD cameras

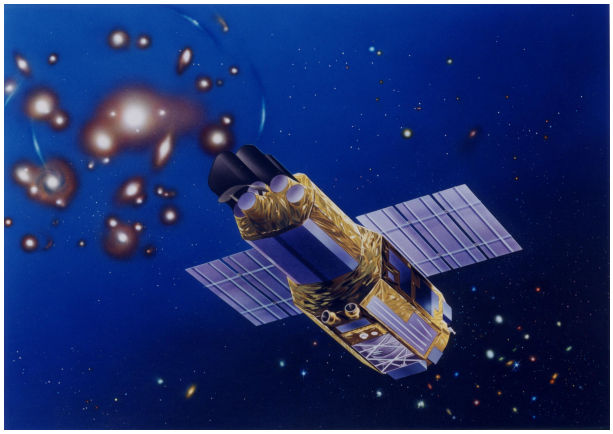

Figure 4.7: Schematic picture of the *Suzaku* satellite.

called X-ray Imaging Spectrometers (XIS; Koyama et al. (2007)), three front-illuminated (FI; energy range 0.4-12 keV) and one back-illuminated (BI; energy range 0.2-12keV), capable of moderate energy resolution. Each XIS is located in the focal plane of a dedicated XRT (Serlemitsos et al., 2007). We only used the XIS data in this thesis, because the HXD has no imaging capability, and hence there remains a large systematic error in estimating the flux from around sources or galactic plane emission. Since, characteristics of them and the associated XRT are described below.

4.2.1 X-ray Telescope (XRT)

The *Suzaku* X-ray Telescopes (XRT) are thin-foil-nested Wolter I type grazing-incidence telescopes, as same as *XMM-Newton*. Figure 4.8 shows the picture of *Suzaku* XRT. The XRTs consist of 175 nested very thin ($\sim$178 μm) gold-coated foils to achieve light weight and high throughput, with moderate imaging capability in the energy range of 0.2–12 keV. The focal length is 4.75 m and the diameter of the largest mirror is 40 cm. Each telescope includes a mirror module, a pre-collimeter for stray light elimination, and a thermal shield to avoid temperature gradient.

Table 4.3: Specifications and characteristics of the XRT on board *Suzaku*

Focal Length	4.75 m
Field of View* at 1.5 keV	$17'$
at 8 keV	$13'$
Angular Resolution (HPD)†	$\sim 2'$
Effective Area† at 1.5 keV	450 cm^2
at 8.0 keV	250 cm^2

* Diameter of the area within the effective area is more than 50% of the on-axis value.
† Measured on the ground.

Table 4.3 summarized the specifications and characteristics of the XRTs. The field of view is about $17'$ at 1.5keV and $13'$ at 8keV, which is a diameter of the area within

Figure 4.8: A *Suzaku* X-ray telescope (XRT)

which the effective area is more than 50% of the on-axis value. The angular resolution of the XRTs is $\sim$ 2′.0, expressed in terms of the half-power diameter, which is the diameter within which half of the focused X-ray is enclosed. The angular resolution does not significantly depend on the energy of the incident X-rays in the energy range of Suzaku, 0.2-12keV. The effective areas are typically 440 cm^2 at 1.5keV and 250 cm^2 at 8keV per telescope. Figure 4.9 shows the on-axis effective area of XRTs.

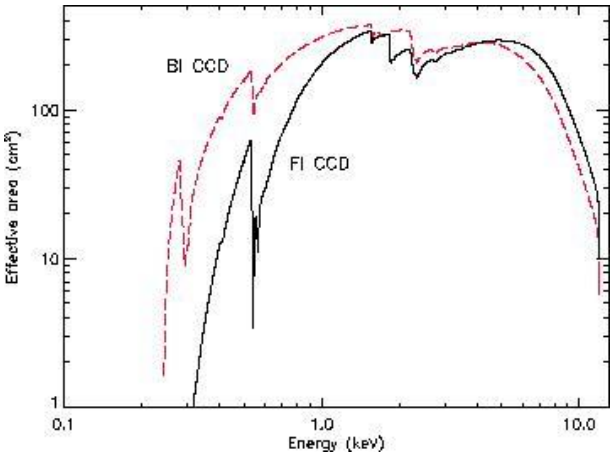

Figure 4.9: The on-axis effective areas of *Suzaku* telescopes, combined with the quantum efficiency of the focal X-ray instruments, XIS. Solid and dashed lines correspond to front-illuminated (FI) CCD and back-illuminated (BI) CCD, respectively.

4.2.2 X-ray Imaging Spectrometers (XIS)

The X-ray Imaging Spectrometers (XISs), X-ray sensitive silicon CCDs, are operated in a photon-counting mode, similar to those used in *XMM-Newton* EPIC. The picture is shown in figure 4.10.

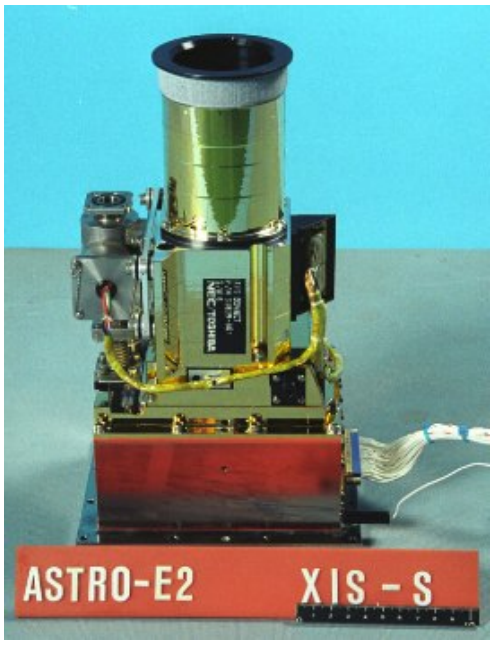

Figure 4.10: A *Suzaku* CCD camera (XIS) sensor.

Table 4.4: Specifications and characteristics of XISs (FI and BI) on board *Suzaku*

	XIS 0, 2, 3	XIS 1
Illumination Method	Front illuminated	Back illuminated
Bandpass	0.2–12 keV	
Field of View	$17'.8 \times 17'.8$	
Number of Pixels	1024×1024	
Pixel Size	24 μm ($1''.0$)	
Spectral Resolution at 5.9 keV	$\sim$130 eV	
Time Resolution (Normal Mode)	8 s	
Effective area* at 1.5 keV	330 cm^2	370 cm^2
at 8.0 keV	160 cm^2	110 cm^2

* On-axis effective area for one sensor including the OBF transmission, the CCD quantum efficiency, and the XRT effective area. The calculations are for a point source integrated over a circular region with a 6 mm ($4'.34$) radius.

Table 4.4 shows specifications and characteristics of XISs. The four *Suzaku* XISs are designated as XIS0, XIS1, XIS2, and XIS3, located in the focal plane of XRTs; XRT-I0, XRT-I1, XRT-I2, and XRT-I3, respectively. In an XIS camera, there is a single CCD chip with an array of 1024 ×1024 pixels, and covers an 17′.8 × 17′.8 region on the sky. The pixel size is 24 μm × 24 μm, and the size of the whole chip is 25 mm × 25 mm. One of the XISs, XIS1, used a back-illuminated (BI) CCD, while the other three use front-illuminated (FI) CCDs. Since the BI CCD has no gate structure on its illuminated side, XIS1 is more sensitive to soft X-rays than the other XISs (see Figure 4.9.

One of the features of *Suzaku* XISs is their superior energy resolution in the low energy band thanks to low background level. Especially, the BI CCD provides comparable spectral resolution to FI CCDs, with quantum efficiency more than 10 times better at $\sim$ 0.4 keV. Another merit of XIS is its low background level. Figure 4.11 shows the background level of various missions normalized by the effective area and the field of view. Among the instrument listed here the *ASCA* SIS had the lowest background, and *Suzaku* XIS (FI and BI CCD) has a low background comparable to *ASCA* SIS. The low background of XIS enables us to achieve high sensitivities especially for spatially extended source.

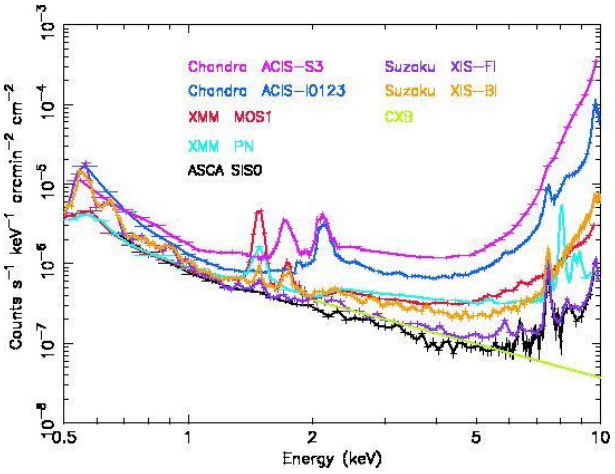

Figure 4.11: XIS background counting rate as a function of energy. The background rate was normalized with the effective area and the field of view, which is a good measure of the sensitivity determined by the background for spatially extended sources. The background rate of ASCA, Chandra, and XMM-Newton adopted from Katayama et al. (2004) are shown for comparisons.

4.3 *Chandra*

The *Chandra* X-ray Observatory (Weisskopf et al., 2002), which was successfully put into its orbit in July 1999, is an astronomical X-ray satellite managed by NASA and Chandra X-ray center.

Chandra's main feature is its high spatial resolution of $\sim$0.5″, which can be ascribed to be X-ray telescope called High Resolution Mirror Assembly (HRMA). For the focal plane instrument, we can choose one of two kinds of X-ray detectors: the Advanced

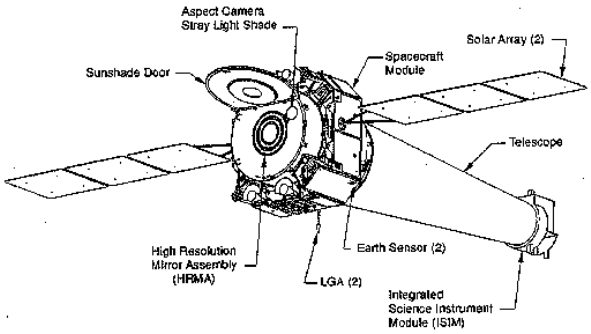

Figure 4.12: Schematic view of the *Chandra* satellite

CCD Imaging Spectrometer (ACIS) and the High Resolution Camera (HRC). HRC is a multiple-channel plate type detector optimized for imaging and is without ability of spectroscopy. Since we used only ACIS in this thesis, HRMA and ASIC are described further below.

4.3.1 High Resolution Mirror Assembly (HRMA)

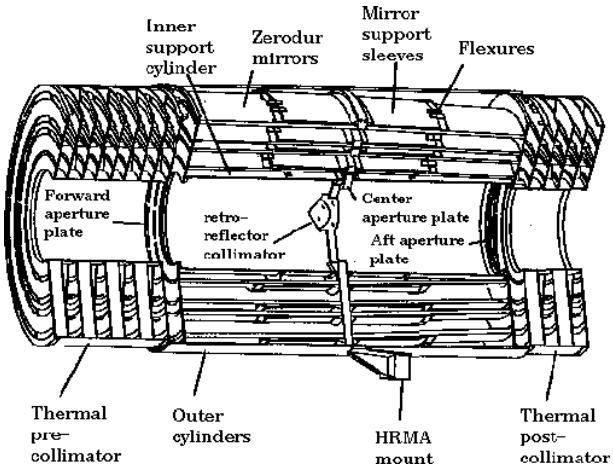

Figure 4.13: Schematic view of the HRMA on board *Chandra*. Source photons come from the left side and are detected on the right side.

Just as the telescope of *XMM-Newton* and *Suzaku*, the *Chandra* HRMA take a form of Wolter Type-I configuration. HRMA consists of a set of 4 concentric thin-walled paraboloid and hyperboloid mirrors, with the focal length of 10 m and the largest mirror having a diameter of ∼1.2 m. Those eight mirrors were fabricated from Zerodur glass, polished, and coated with iridium on a binding layer of chromium. In other to keep high accuracy of the mirror surface, the glass is very thick and heavy with the total mass of ∼1500 kg. Schematic view of the HRMA are shown in figure 4.13.

Table 4.5 shows the physical parameters of HRMA. The point spread function is so sharp, hence the angular resolution is limited by the detector pixel size of $\sim 0.5''$. The on-axis effective area is shown in figure 4.14. The effective area is smaller than that of

Table 4.5: Specifications and characteristics of the HRMA on board *Chandra*

Focal Length	10.07 m
Ghost-free Field of View	$30'$
Angular Resolution (FWHM with detector)	$<0.5''$
Effective Area at 0.25 keV	800 cm^2
at 5.0 keV	400 cm^2
at 8.0 keV	100 cm^2

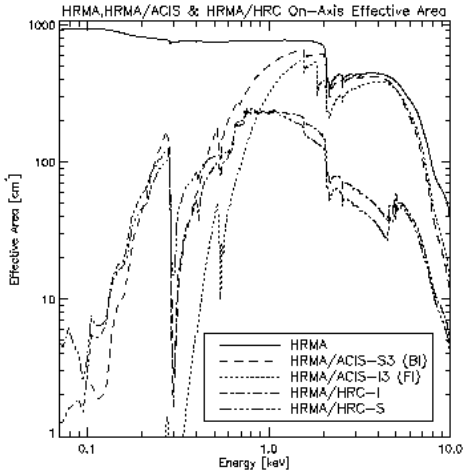

Figure 4.14: On-axis effective area of HRMA as a function of X-ray energy

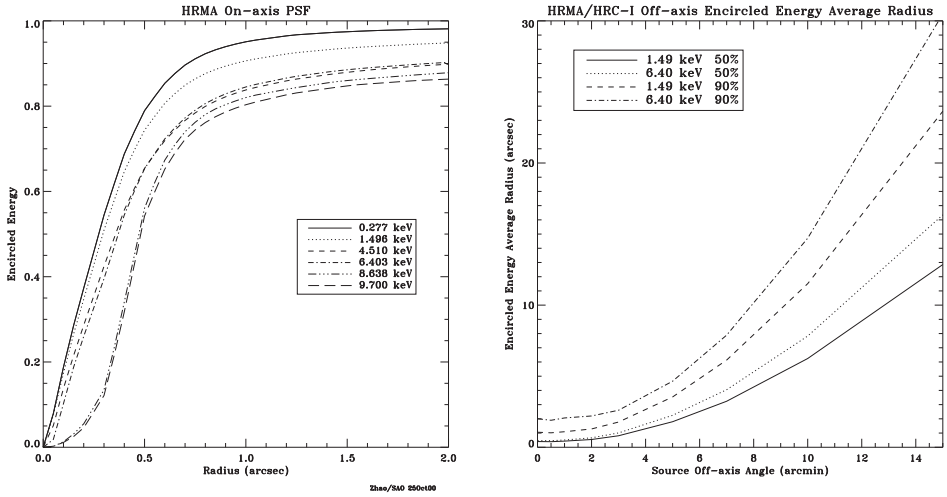

Figure 4.15: (left) The Fractional encircled energy as a function of angular radius, calculated for an on-axis point source, at selected X-ray energies. (right) The HRMA/HRC-I encircled energy average radii for circles enclosing 50% and 90% of the power at 1.49 and 6.40 keV as a function of off-axis angle.

XMM-Newton and *Suzaku*. The encircled energy function of HRMA is shown in figure 4.15 (left). On axis, 50% photons are included in a radius of $\sim 0.''35$ for 4.51 keV X-rays. The focus blurrs as the distance from the on-axis point becomes large (figure 4.15 (right)).

4.3.2 Advanced CCD Imaging Spectrometer (ACIS)

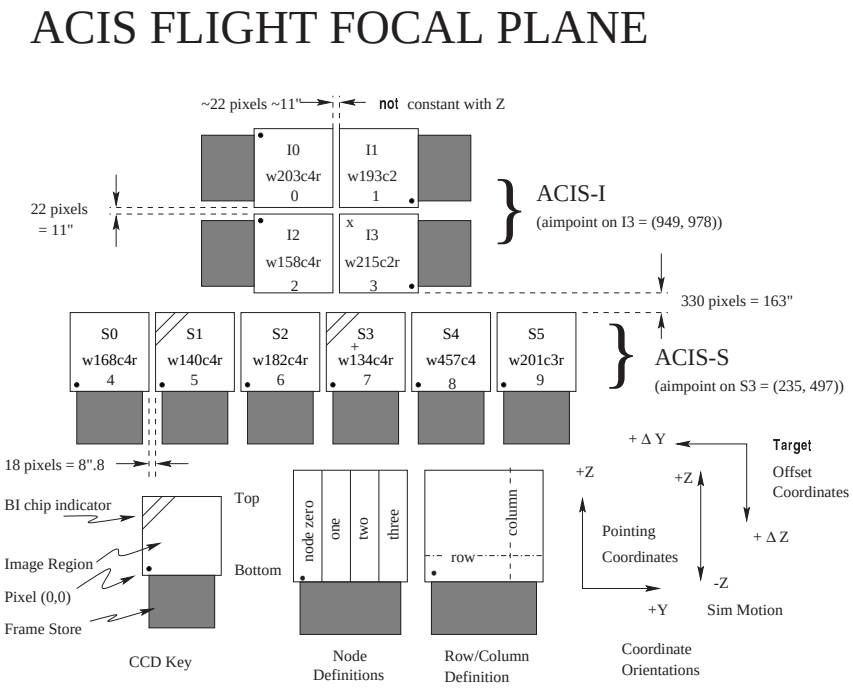

Figure 4.16: A schematic drawing of the ACIS focal plane

The ACIS array consists of ten CCDs, which are divided into two parts; ACIS-I with 2×2 CCDs and ACIS-S with 1×6 CCDs. The former is mainly used for imaging-spectroscopy, whereas the latter are for grating spectroscopy. ACIS-S1 and ACIS-S3 are back-illuminated CCDs, whereas all the other CCDs are front-illuminated CCDs. We used only ACIS-I in this thesis.

Table 4.6: Specifications and characteristics of ACIS (FI) on board *Chandra*

Number of Pixels	1024 × 1024
Pixel Size	24 μm ($0.''492$)
ACIS-I array size	$16.'9 \times 16.'9$
ACIS-S array size	$8.'3 \times 50.'6$
Spectral Resolution at 5.9 keV	∼120 eV
Time Resolution (Full Frame Mode)	3.2 s
Effective area at 0.5 keV	110 cm^2
at 1.5 keV	600 cm^2
at 8.0 keV	40 cm^2

Table 4.6 shows the specifications and characteristics of front-illuminated ACIS. The spectral resolution of FI CCD is ∼120 eV at 5.9 keV, and the time resolution of full frame mode is 3.2 sec.

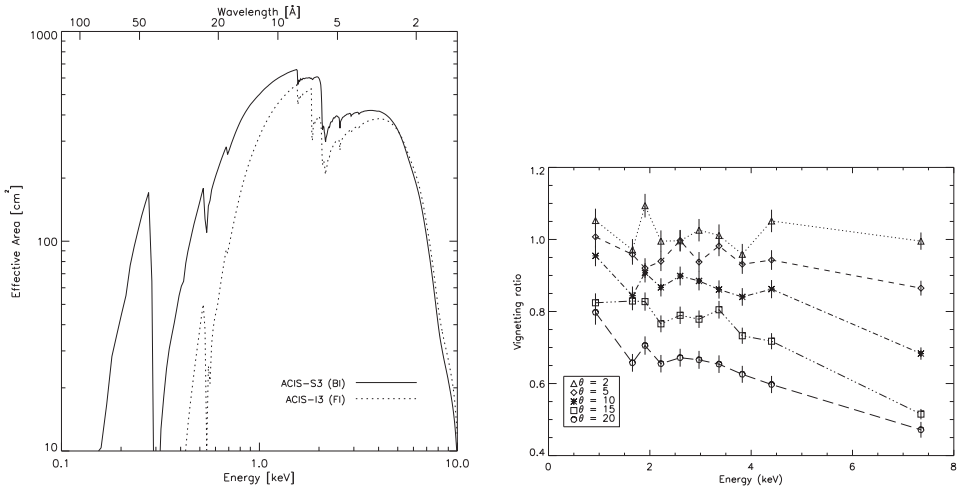

Figure 4.17: (left) The HRMA/ACIS predicted effective area versus the energy on a log scale. The dashed line is for the FI CCD I3, and the solid line is for the BI CCD S3. (right) Vignetting (the ratio of off-axis to on-axis effective area) as a function of energy for several off axis angles in arcminutes.

Figure 4.17 show the on-axis effective area of FI and BI CCDs (left), and vignetting as a function of energy for several off-axis angles. The more off-axis angle becomes large, the more energy dependence of vignetting ratio stands out.

Chapter 5

Analysis of W28

5.1 Overview of W28

The SNR W28, which is located at $(l, b) = (6.^{\circ}4, -0.^{\circ}1)$, is an interesting target as a cosmic ray accelerator from which GeV and TeV γ-rays were detected from the eastern edge of the radio shell (Abdo et al. (2009); Aharonian et al. (2008a)). The whole image of W28 is shown in figure 5.1, which is in the 0.5–2.4 keV band obtained with *ROSAT* satellite. A diameter and a distance to W28 are 48 arcmin and 1.9 kpc, respectively (Velázquez et al., 2002) , and a physical diameter is calculated to be 27 pc. Rho & Borkowski (2002) reported the age of several times 10^4 years by the ionization time scale of the southwest shell combined with the electron density, which means W28 is a middle-aged SNR. The age, the temperature, and the shock speed obtained by the Sedov solution (eq. (3.9), (3.10) and (3.11)) are 11000 years, 0.6 keV and 800 km s^{-1}, respectively, on the assumption that expansion energy is 10^{51} erg and the plasma density is 1 cm^{-3}.

W28 is classified as "mixed–morphology" (MM) SNR, showing center-filled X-rays and a shell-like radio emission. Figure 5.2 (a) shows a 1.4 GHz radio image. The shell-like radio emission peaks at the northern and northeastern boundaries where interaction of the SNR matter with the molecular cloud is established (Wootten, 1981). This interaction was revealed by a lot of OH Maser spots (Frail et al., 1994; Claussen et al., 1997; Hoffman et al., 2005), which are signposts of molecular interactions and the location of high density shocked gas. Arikawa et al. (1999) clarified the distribution of post-shock and pre-shock molecular cloud from their CO (J = 3–2) and CO (J = 1–0) observations, respectively. Figure 5.3 shows the examples of CO (J = 1–0) and CO (J = 3–2) spectra adapted from Arikawa et al. (1999). The CO line profile consists of two component; (i) narrow components with a FWHM linewidth of $\Delta V \sim 3$ km s^{-1} at the velocity with respect to a local standard of rest (LSR) frame $V_{\rm LSR} \sim +7$ and +21 km s^{-1}, and (ii) a broad component with a FWHM linewidth of $\Delta V \geq 20$ km s^{-1}. They argued that the 7 km s^{-1} narrow component, which is intense in CO (J = 1–0), corresponds to "pre-shock" molecular gas associated with W28, while the broad component whose intensity is stronger in CO (J = 3–2) is likely to be post-shock accelerated gas due to the interaction of W28 with the molecular cloud. A kinetic temperature and a density ($n_{\rm H_2}$) were found to be $\leq$20 K and $\leq 10^3$ cm^{-3} in the pre-shock gas, and $\geq$60 K and $\geq 10^4$ cm^{-3} in the post-shock gas, respectively. TeV γ-ray was detected by H.E.S.S. (Aharonian et al., 2008a) from the eastern edge of the radio shell as shown in figure 5.2 (b). The photon index and the 1–10 TeV flux are 2.66$\pm$0.27 and 1.3×10^{-12} erg cm^{-2} s^{-1}, respectively. Recently, *Fermi* also

detected γ-ray at 100 MeV $<E<$ 100 GeV (Abdo et al., 2009). In contrast, the emission in X-ray band has been believed to comprise of thermal radiation. Rho & Borkowski (2002) evaluated temperatures of 1.5 keV in the southwest, 0.56 keV in the northeast, and the central region requires two temperature plasma with 0.6 keV and 1.8 keV. The long ionization timescales in the northeast and central region imply that the gas is close to the ionization equilibrium.

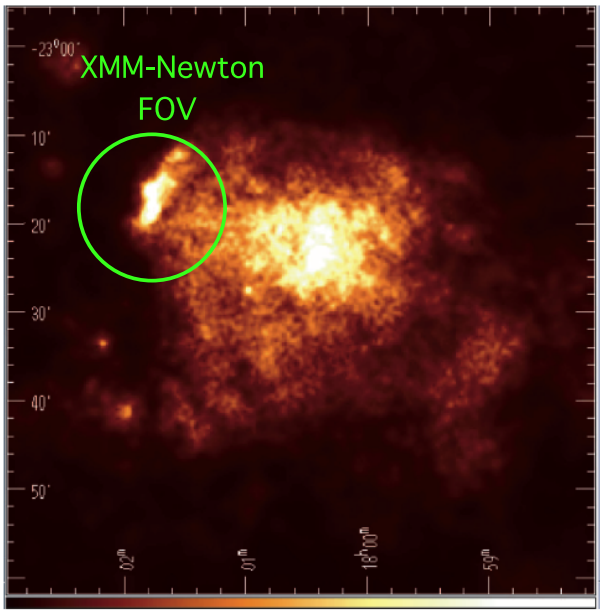

Figure 5.1: Mosaicked *ROSAT* image (0.5–2.4 keV) of W28 taken from Rho & Borkowski (2002). A green circle corresponds to *XMM-Newton* MOS field of view.

5.2 *XMM-Newton* Observations and Data Reduction

We analyzed *XMM-Newton* archival data of the north–eastern part of W28, where the molecular clouds, OH Maser spots, bright X-ray shells, GeV and TeV emission were detected. The field of view of *XMM-Newton* MOS instrument is shown in figure 5.1 green circle. *XMM-Newton* has large effective area and high angular resolution. These characteristics enable us to carry out high quality spatially resolved spectroscopy.

The north-eastern part of W28 was observed with the European Photon Imaging Camera (EPIC) on board *XMM-Newton* Observatory on 2002 September 23 (ObsID = 0145970101) and 2003 October 7 (ObsID = 0145970401), respectively. The nominal pointing position was $\alpha = -270.^{\circ}438$, $\delta = -23.^{\circ}330$ (J2000). All of the EPIC instruments were operated in the full-frame mode with a thick filter. We used version 7.0.0 of the Standard Analysis System (SAS) software, and selected X-ray event with PATTERN keywords of $\leq$12 for the MOS1/2 and $\leq$4 for the pn, respectively.

The net exposure times were 54.1 ksec and 49.9 ksec for the MOS1/2 and the pn, respectively after combining the 2002 and 2003 data. To remove the high particle background time intervals, we accumulated a lightcurve in the 10–12 keV band from the whole field of view, and filtered the time intervals when the count rate was larger than

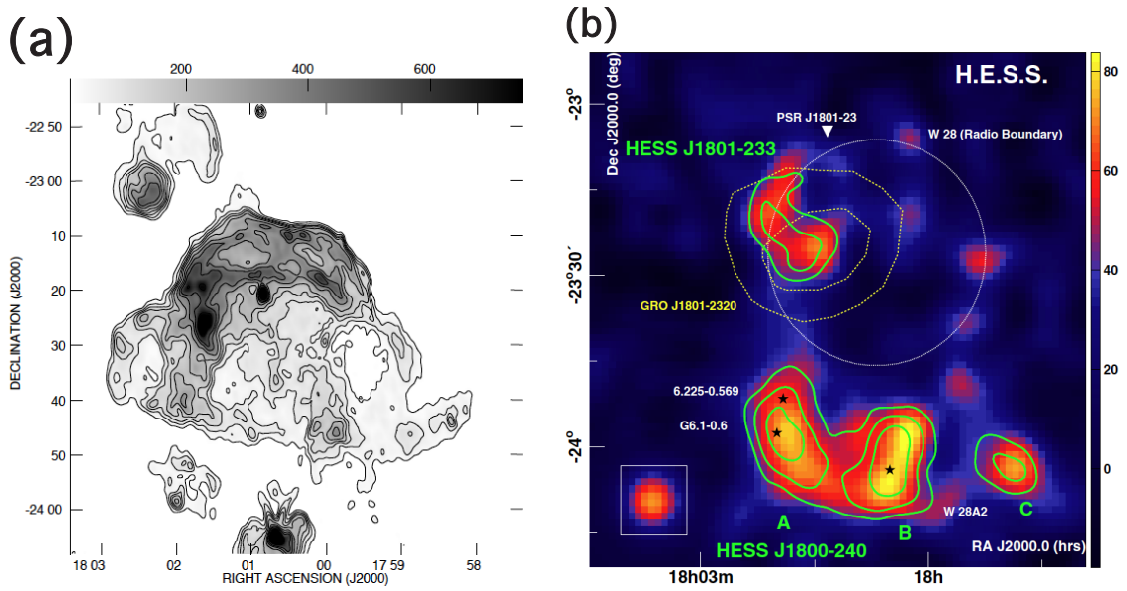

Figure 5.2: (a) 1.4 GHz radio image adapted from Dubner et al. (2000). The gray scale varies between 10 and 750 mJy beam^{-1}. (b) TeV γ-ray excess map of W28 region ($1\overset{\circ}{.}5 \times 1\overset{\circ}{.}5$) taken from Aharonian et al. (2008a). The thin-dotted circle depicts the approximate radio boundary of the SNR W28 guided predominantly by the bright northern radio emission. TeV γ-ray emission was detected from the northeastern part of W28, named "HESS J1801-233". The inset to the bottom left depicts the beam size.

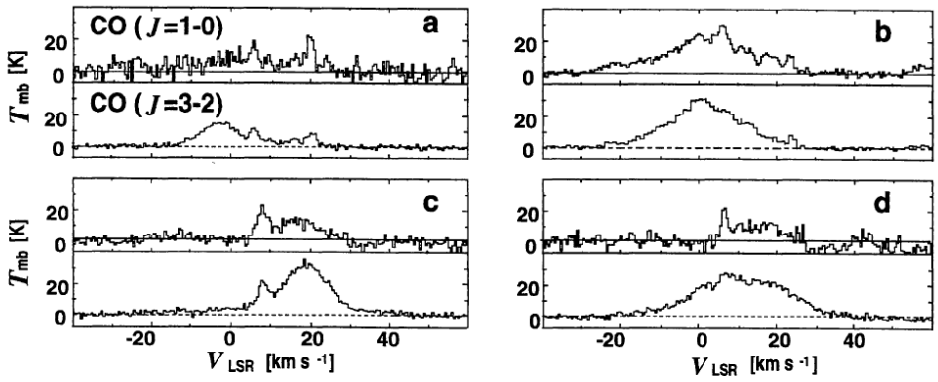

Figure 5.3: Examples of CO (J = 1–0) and CO (J = 3–2) spectra obtained towards four positions in W28 SNR, which is adapted from Arikawa et al. (1999).

0.35 count/s for the MOS and 0.4 count/s for the pn. After this screening, the effective exposure time of MOS1, MOS2 and pn were 51.9 ksec, 52.1 ksec and 39.6 ksec, respectively.

5.3 Image Analysis

Figure 5.4 shows the exposure-corrected MOS images in 0.3–2.0 keV and 2.0–10.0 keV with a binning size of 25.″6. They were created by combining all the MOS1/2 data from

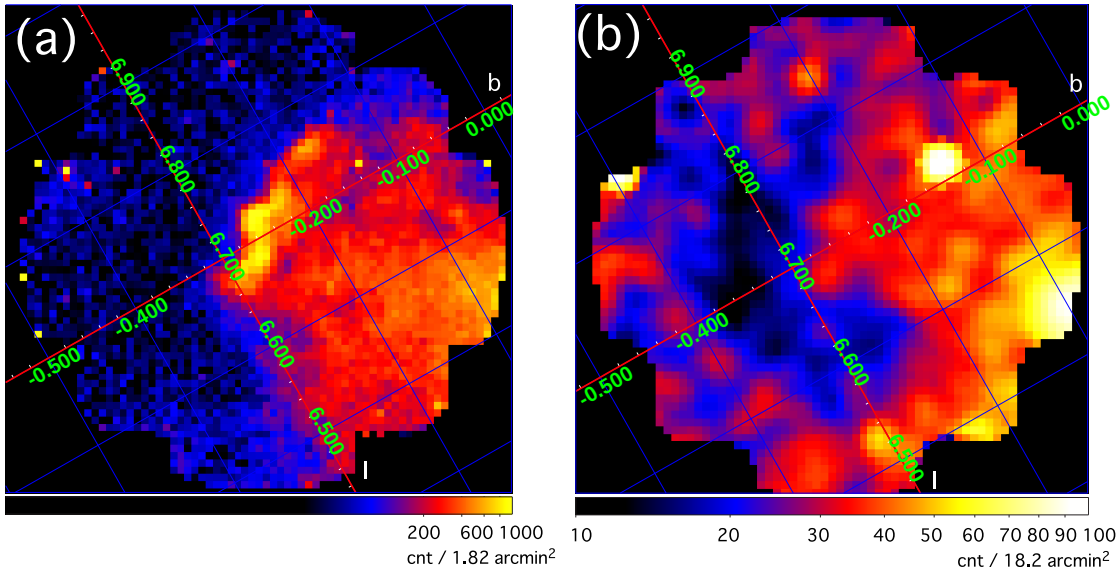

Figure 5.4: Exposure corrected images of the north-eastern part of W28 (a) in 0.3–2.0 keV and (b) in 2.0–10.0 keV in logarithmic scale in the galactic coordinates. The images are binned up to 25.″6 per pixel.

the 2002 and 2003 observations. In the low energy band image, the shell region located at (l, b) $\simeq$ (6.°70, $-$0.°26) is the brightest. Its shape is twisted in a complex manner. The inner region of W28, toward the southwest of the image, is also enhanced in surface brightness. In the high energy band, on the other hand, the inner region is much brighter than the shell region.

In Fig. 5.5 shown are intensity contours of CO (J = 3–2) and CO (J = 1–0) in red and blue (Arikawa et al., 1999) and those of TeV γ-ray with H.E.S.S. in yellow (Aharonian et al., 2008a), overlaid on the 0.3–2.0 keV gray scale MOS image (Fig. 5.4a). The CO J =3–2 and 1–0 contours trace distributions of post-shock and pre-shock molecular clouds, respectively (Arikawa et al., 1999). The green dots represent OH maser spots, which also indicate presence of shock waves (Claussen et al., 1997). The aqua circle indicates the 95% confident error circle of the GeV γ-ray source detected with *Fermi* in Abdo et al. (2009). The eastern bunch of the OH maser sources spatially coincides with the edge of the X-ray bright shell, as well as the edge of the eastern molecular cloud. This indicates that the shock occurs there. Edge of one of the TeV γ-ray peaks seems to appear at the same position. OH maser spots are also detected with spatial coincidence with a molecular cloud region which extends linearly from the X-ray shell toward western edge

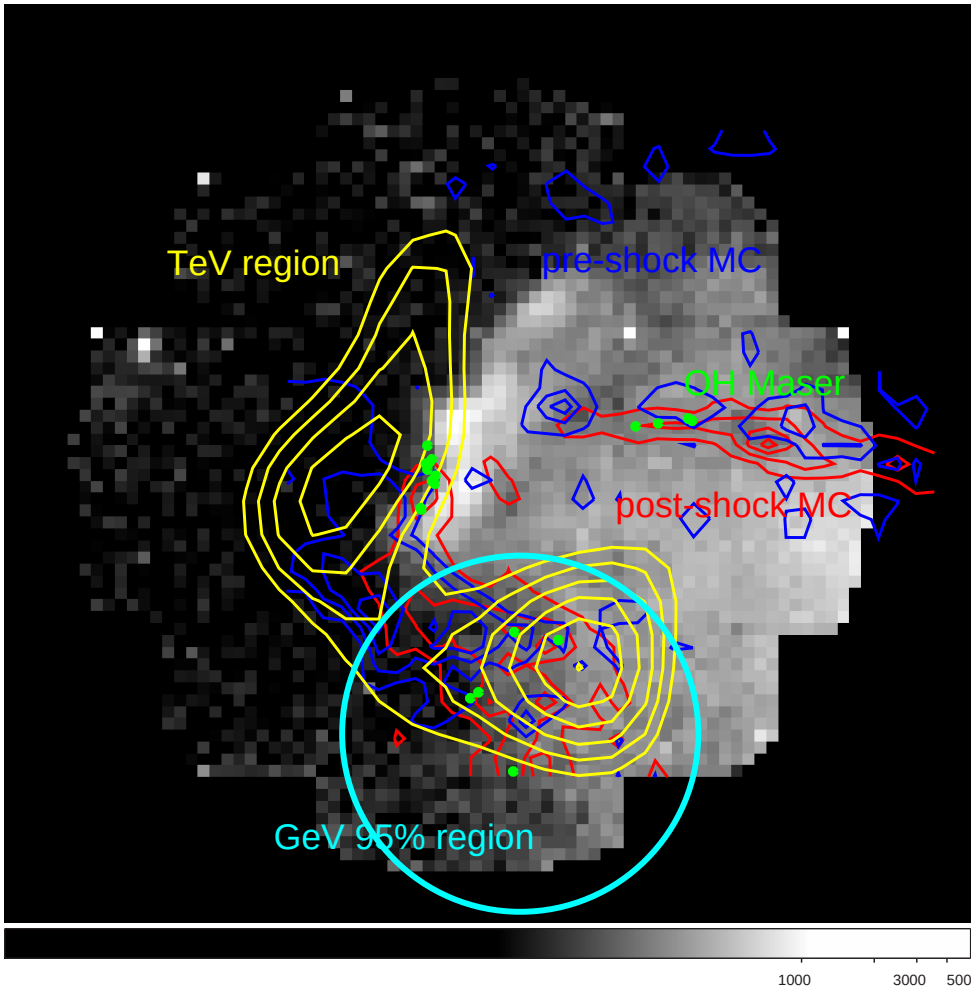

Figure 5.5: Gray scale X-ray image with molecular clouds (the blue and red) and TeV γ-ray (yellow) contours overlaid. The blue and red molecular cloud contours are velocity-integrated line intensities of CO (J = 1–0) and CO (J = 3–2) in logarithmic scale, respectively, which correspond to 0–55 K km s^{-1} pre-shock cloud and 60–650 K km s^{-1} post-shock cloud, respectively. The yellow TeV γ-ray contours are in linear scale from 50 to 70 count/1.4 arcmin^2. Green points are the positions of OH Maser. The 95% confidence region of a GeV source detected with the *Fermi* satellite is shown in aqua circle.

of the image. In the southern part of the image, the molecular clouds coincide with the other TeV γ-ray emission peaks, where the surface brightness of the X-ray emission is somewhat reduced. From this region, several OH maser spots are also detected. They are all within the error circle of the GeV γ-ray source.

5.4 Spectral Analysis

In this section, we present the results of spatially-resolved spectral analysis. The analysis is carried out on the shell regions, the inner region, and the eastern peak of the TeV γ-ray emission, which are described in § 5.4.1 through § 5.4.4. The source and the background regions are summarized in figure 5.6. The purposes of the spectral analysis are as follows;

- North-eastern shell region ;
  To elucidate the nature of an excess emission over the shell emission due to collision of SNR outflow with the molecular cloud, and to search for non-thermal X-ray emission from accelerated electrons. We therefore adopt the south-eastern shell region for background extraction.

- South-eastern shell region ;
  To search for evidence of non-thermal X-ray emission by secondary electrons which are originated from interaction of putative accelerated protons with molecular clouds. Note that this region overlaps with molecular clouds and one of the TeV γ-ray peaks.

- Inner region ;
  To search for the presence of non-thermal X-ray emission.

- TeV γ-ray peak region ;
  To determine the X-ray flux for constraining TeV γ-ray emission mechanism.

The background regions are chosen to accomplish these purposes, and by considering the vignetting effect.

In evaluating the spectra, we have utilized XSPEC (version 11.3.2) in the band 0.3–10.0 keV. We have created ancillary response file (ARF) by assuming flat brightness distribution within each source integration region. As emission spectral models, we basically adopt the NEI model to represent optically thin thermal spectra in ionization non-equilibrium. In some cases where the NEI model indicates the ionization equilibrium, we utilize the APEC model also. In applying these models to the data, we adopt the metal composition of Anders & Grevesse (1989) as the solar abundance. To represent interstellar absorption, we multiply the model PHABS on these emission models. In the course of the spectral fitting, we have found that there remain wiggles in the fit residual. This is caused by difference of gain among the CCD chips of MOS-1/2 and the inaccuracy of calibration of the line spread function. Accordingly, we always multiply a Gaussian smoothing model (GSMOOTH in XSPEC) on the emission models. The errors quoted are always at the 90% confidence level.

5.4.1 North-eastern shell region

In Fig. 5.7 (a) shown with ellipses are regions 1 through 3 for collecting photons from the north-eastern shell, overlaid on the 0.3–10 keV MOS image.

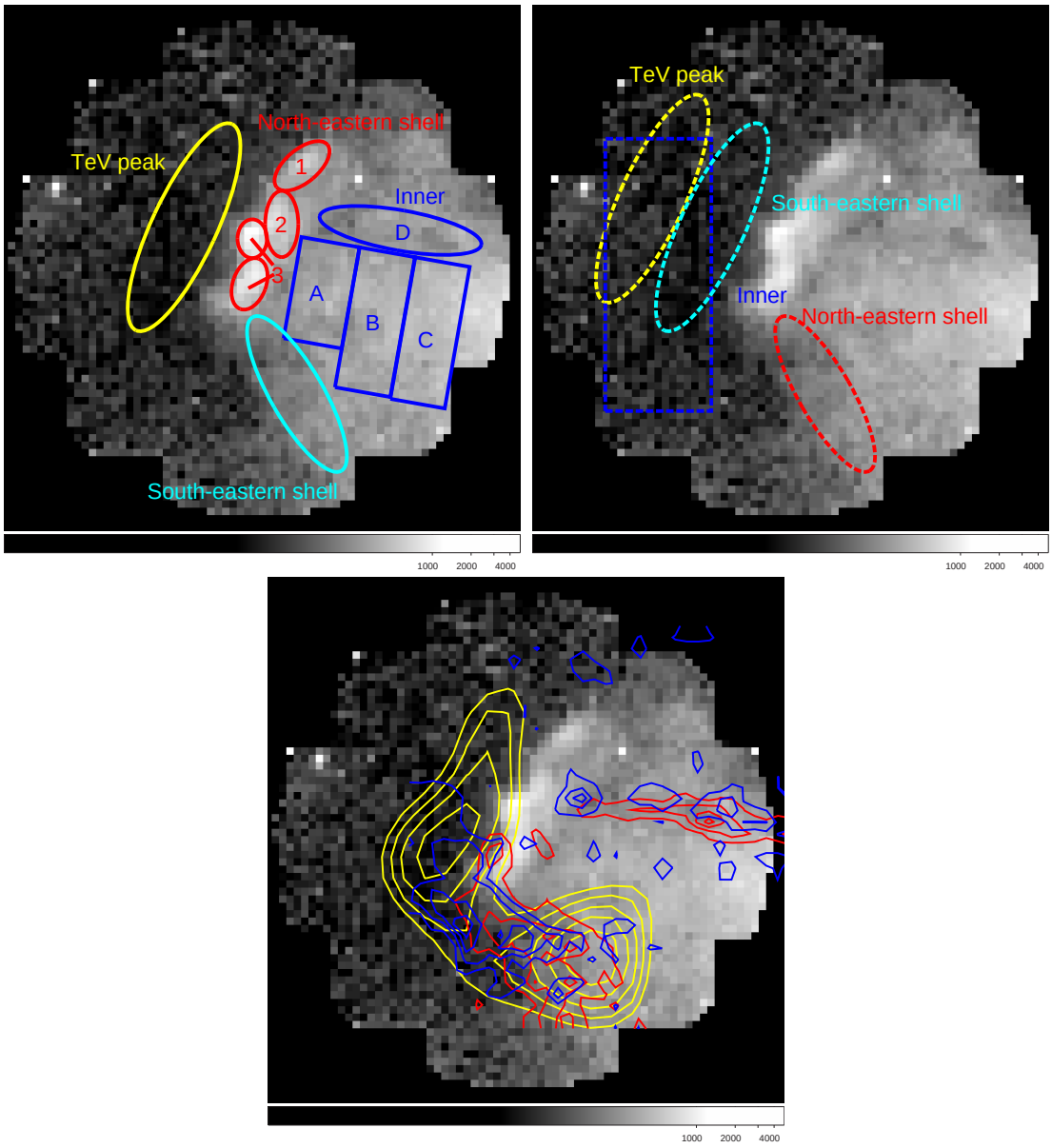

Figure 5.6: Spectral extracted regions of W28. (a) Source regions. (b) Corresponding background regions drawn with the same colors as the source regions. (c) Gray scale X-ray image with pre-shock and post-shock molecular cloud intensity contour in blue and red, and TeV γ-ray contort shown in yellow.

.

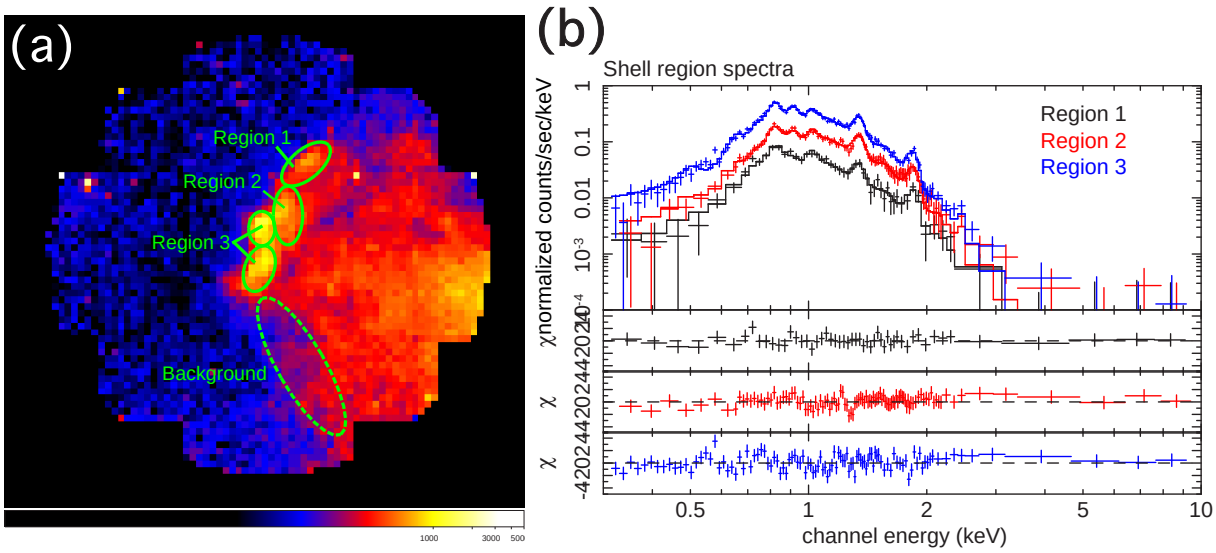

Figure 5.7: (a) The photon integration regions for the north-eastern shell. Region 1 and 2 are an ellipse with 0′.96 × 1′.9, and region 3 is composed of two ellipses, one with 0′.85 × 1′.1 and the other with 0′.96 × 1′.5. The dashed ellipse is the common background region. (b) MOS spectra of each regions with the best-fit VAPEC model. Black, red and blue represent the data and the models of region 1, 2, and 3, respectively. The residuals are shown in the bottom panels. The best-fit parameters are summarized in table 5.1
.

The dashed ellipse is the background region. This region is taken symmetrical to regions 1 through 3 with respect to the peak of the center-filled brightness distribution of W28 as well as to the optical axis position of the current field of view, in order to elucidate the nature of an excess emission from the shell.

The background-subtracted MOS spectra are shown in figure 5.7 (b) which are combined ones of MOS1 and MOS2 from the 2002 and 2003 observations. The black, red and blue crosses represent the data points from region 1, 2 and 3, respectively. We have obviously detected He-like Kα emission lines from O (0.57 keV), Ne (0.91 keV), Mg (1.34 keV), Si (1.86 keV), and L lines of Fe around 1 keV. This means that the spectra include an optically thin thermal component. We therefore tried to fit the spectra with a single temperature non-equilibrium collisional ionization plasma emission model (VNEI model in XSPEC; Borkowski et al. (2001); Hamilton et al. (1983); Borkowski et al. (1994); Liedahl et al. (1995)) undergoing photoelectric absorption represented with a single hydrogen column density $N_{\rm H}$. In the fitting, we set abundances of O, Ne, Mg, Si, and Fe free to vary but constrained to be common among the regions, because no statistically significant difference in the abundances are found among the regions in a trial fit. The abundances of the other elements are fixed at the solar values. The fitting is acceptable with the reduced χ^2 of 0.91. As a result, however, we found an ionization parameter $n_{\rm e}t$ of $\sim 10^{13}$ cm^{-3}s, which indicates the shell plasma is in collisional ionization equilibrium. Accordingly, we replaced the VNEI model with a VAPEC model which represents a spectrum from a plasma in collisional ionization equilibrium (http://hea-www.harvard.edu/APEC). The best-fit parameters are summarized in table 5.1, and the best-fit models as well as the residuals are displayed in figure 5.7 (b). Note that we used both MOS and pn data for spectral

Table 5.1: Best-fit parameters of the north-eastern shell region spectra

Parameters		Region 1	Region 2	Region 3
VAPEC				
Temperature [keV]		$0.37^{+0.05}_{-0.03}$	$0.30^{+0.02}_{-0.01}$	0.28 ±0.01
abundance [1]	O		$0.29^{+0.07}_{-0.05}$	
	Ne		$0.33^{+0.06}_{-0.04}$	
	Mg		$0.39^{+0.06}_{-0.05}$	
	Si		$0.62^{+0.10}_{-0.08}$	
	Fe		$0.42^{+0.07}_{-0.05}$	
E.M. [2]		$1.8^{+0.6}_{-0.5}$	10 ±2	22 ±3
$N_{\rm H}$ [3]		6.2 ±0.5	8.2 ±0.3	7.5 ±0.2
gsmooth				
σ (MOS) [4]		$0.11^{+0.06}_{-0.05}$	$0.088^{+0.030}_{-0.033}$	$0.094^{+0.020}_{-0.018}$
σ (pn) [4]		$0.11^{+0.09}_{-0.11}$	0.23 ±0.05	0.17 ±0.03
index [5]		1.0 (fix)	1.0 (fix)	1.0 (fix)
χ^2/d.o.f (reduced χ^2)		461.6 / 546 (0.85)		

[1] Abundance ratio relative to the solar value (Anders & Grevesse, 1989). The abundances are common over the regions.
[2] Emission measure $E.M. = \int n_e n_H dV \simeq n_e^2 V$ in units of 10^{56} cm^{-3}, where n_e and V are the electron density and the plasma volume. The distance to W28 is assumed to be 1.9 kpc (Velázquez et al., 2002).
[3] Absorption column density in units of 10^{21} cm^{-2}.
[4] Gaussian sigma at 6 keV in a unit of keV.
[5] Energy index of σ, namely, $\sigma \propto E^{-\rm index}$.

fitting, although only MOS spectra are shown in figure 5.7 (b) for clarity. The reduced χ^2 of 0.85 implies that the fit is acceptable at the 90% confidence level. The temperatures are obtained to be $kT = 0.37^{+0.05}_{-0.03}$ keV, $0.30^{+0.02}_{-0.01}$ keV and 0.28 ± 0.01 keV for regions 1, 2, and 3, respectively. The temperature decreases from north to south in the shell. The hydrogen column density $N_{\rm H}$ are $6.2\pm0.5 \times 10^{21}$ cm^{-2}, $8.2\pm0.3 \times 10^{21}$ cm^{-2} and $7.5\pm0.2 \times 10^{21}$ cm^{-2} for region 1, 2, and 3, respectively. The hydrogen column densities of region 2 located slightly inside, and region 3 near the molecular cloud are higher than that of region 1. The abundances of the elements that are set free converge to sub-solar values. There is no non-thermal X-ray in the north-eastern shell.

5.4.2 South-eastern rim region

We next analyzed a spectrum from the south-eastern rim region of W28, which is encircled with a solid ellipse in Fig. 5.8(a). As notice from this figure, the region corresponds to one

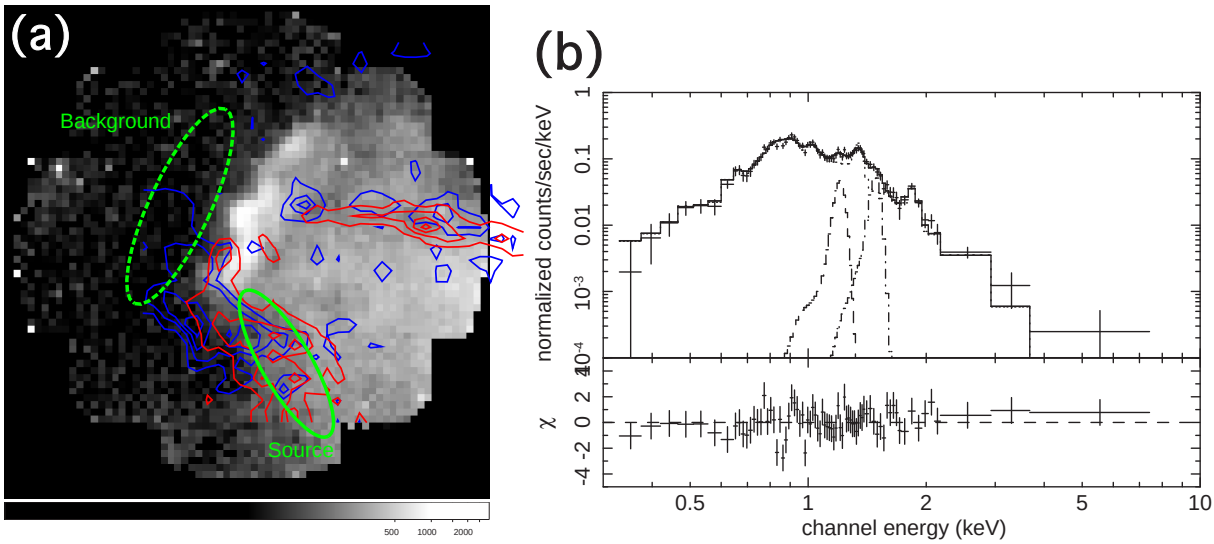

Figure 5.8: (a) The photon-integration region of the south-eastern rim. The solid ellipse with 5′.3 × 1′.5 is the source region, whereas a dashed ellipse region correspond to the background-integration region. (b) MOS spectrum with the best-fit VNEI model. The residuals are shown in the bottom panel. The best-fit parameters are summarized in table 5.2.

of the molecular clouds emitting the CO lines. This region was used as the background region for the analysis of the north-eastern shell in §5.4.1. Since this region apparently contains emission only from the center-filled emission, we consider this region being appropriate as the background region to evaluate the nature of the excess emission associated with the shell structure. In this section, on the other hand, we have chosen the same region as the source region to search for evidence of non-thermal X-ray emission originating from interaction of accelerated protons with molecular clouds. We extracted a background spectrum from the dashed ellipse region, which is set out of W28, as shown in Fig. 5.8(a). The observed spectrum as well as the best-fit model and the residual are shown in Fig. 5.8(b). The model is composed of a single temperature VNEI model with two Gaussian lines at 1.2 keV and 1.5 keV, of which the former belongs to Fe L-shell line

forests that is missing in the fitting model (Brickhouse et al. (2000); Rho et al. (2002)) whereas the latter is a fluorescent Al Kα line due to interaction of cosmic-ray particles with the camera body. In order to correct possible calibration error on the line-spread function, we convolved a Gaussian to the spectrum using the XSPEC model GSMOOTH. The best-fit VNEI parameters are summarized in table 5.2. The fit is acceptable at the 90%

Table 5.2: Best-fit parameters of the south-eastern shell region spectrum

Parameters		
VNEI		
Temperature [keV]		$0.60^{+0.03}_{-0.05}$
abundance [1]	O	$0.26^{+0.10}_{-0.07}$
	Ne	$0.38^{+0.14}_{-0.12}$
	Mg	$0.70^{+0.22}_{-0.14}$
	Si	$0.61^{+0.24}_{-0.17}$
	Fe	$0.34^{+0.12}_{-0.06}$
$n_{\rm e}t$ [10^{11} s/cm^3] [2]		$0.94^{+0.26}_{-0.21}$
E.M. [10^{56} cm^{-3}] [3]		$1.5^{+0.6}_{-0.4}$
$N_{\rm H}$ [10^{21} cm^{-2}] [4]		$5.3^{+0.8}_{-0.6}$
gsmooth		
σ (MOS) [keV] [5]		0.13 $\pm$0.03
σ (pn) [keV] [5]		$0.26^{+0.07}_{-0.05}$
index [6]		1.0 (fix)
χ^2/d.o.f (reduced χ^2)		130 / 123 (1.05)

[1] Abundance ratio relative to the solar value (Anders & Grevesse, 1989). The abundances are common over the regions.
[2] Ionization time-scale in units of 10^{11} cm^{-3} s, where $n_{\rm e}$ and t are the electron density and age of the plasma.
[3] Emission measure $E.M. = \int n_e n_H dV \simeq n_e^2 V$ in units of 10^{56} cm^{-3}, where n_e and V are the electron density and the plasma volume. The distance to W28 is assumed to be 1.9 kpc (Velázquez et al., 2002).
[4] Absorption column density in units of 10^{21} cm^{-2}.
[5] Gaussian sigma at 6 keV in a unit of keV.
[6] Energy index of σ, namely, $\sigma \propto E^{-\rm index}$.

confidence level. The temperature, the ionization parameter and the emission measure are obtained to be $kT = 0.60^{+0.03}_{-0.05}$ keV, $n_{\rm e}t = 9.4^{+2.6}_{-2.1} \times 10^{10}$ cm^{-3}s and $E.M = 1.5^{+0.6}_{-0.4} \times 10^{56}$ cm^{-3}, respectively. The abundances are sub-solar as same as the excess shell component. Non-thermal emission was not detected from this region.

5.4.3 Inner Regions

We have extracted four source spectra from the inner region, as shown in the gray scale picture of Fig. 5.9. Regions A through C are box-shaped and are separated from the shell region in this order. We have set these regions not to overlap the molecular clouds. Region D is taken offset to north of regions A through C so that it overlaps the northern

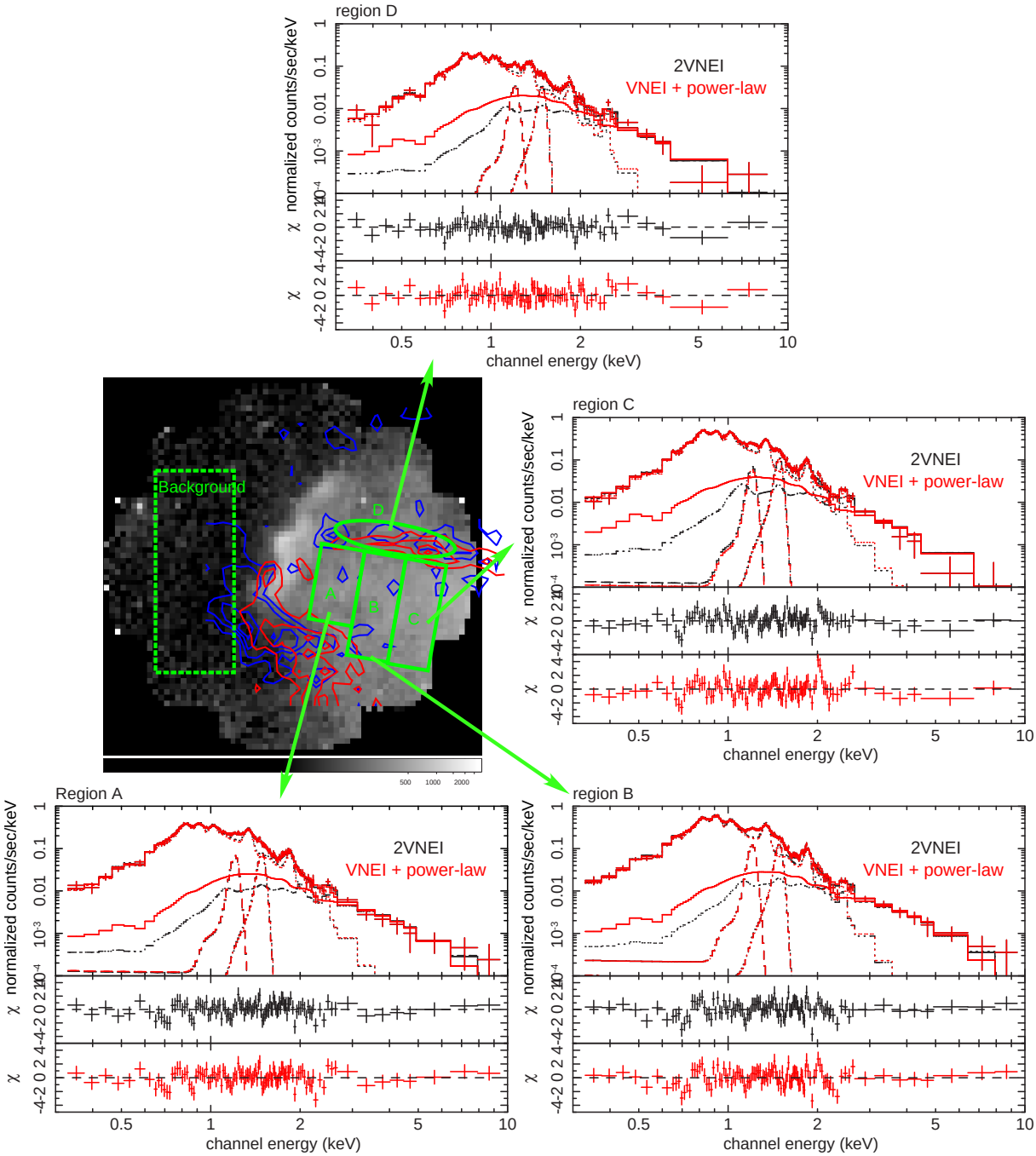

Figure 5.9: The source and background integration regions and the resultant spatially-resolved spectra of the inner regions of W28. The integration regions of source photons are shown with solid lines (A through D). The bashed region corresponds to the background-integration region. Regions A to C are rectangles with two sides being 6′.0 × 3′.4, 8′.3 × 3′.7 and 8′.2 × 3′.5, respectively. Region D is an ellipse with a semi-major and minor axes being 4′.8 and 1′.3 for, respectively. The other four panels show MOS spectra from each region. The black histograms show a two-temperature VNEI model whereas the red ones show a model composed of a single temperature VNEI and a power law. The residuals are shown in the bottom panels. The best-fit parameters are summarized in table 5.3 and table 5.4.

Table 5.3: Best-fit parameters of the inner region spectra with two-temperature thermal emission models.

Parameters		Region A	Region B	Region C	Region D
VNEI 1 (low temperature)					
abundance [1]	O	$0.43^{+0.16}_{-0.10}$	$0.44^{+0.14}_{-0.09}$	$0.47^{+0.24}_{-0.20}$	$0.41^{+0.27}_{-0.15}$
	Ne	$0.55^{+0.09}_{-0.12}$	$0.81^{+0.23}_{-0.13}$	$0.82^{+0.31}_{-0.33}$	$0.66^{+0.36}_{-0.20}$
	Mg	$0.77^{+0.24}_{-0.15}$	$1.1^{+0.3}_{-0.2}$	$0.97^{+0.34}_{-0.22}$	$0.85^{+0.46}_{-0.25}$
	Si	1.3 ± 0.3	$1.5^{+0.5}_{-0.3}$	$1.5^{+0.7}_{-0.3}$	$1.6^{+1.1}_{-0.6}$
	S	$1.9^{+1.1}_{-0.8}$	$1.9^{+0.9}_{-0.6}$	$2.1^{+0.9}_{-0.7}$	$2.4^{+1.8}_{-1.1}$
	Fe	$0.46^{+0.12}_{-0.08}$	$0.48^{+0.11}_{-0.07}$	$0.56^{+0.11}_{-0.12}$	$0.50^{+0.12}_{-0.13}$
$n_{\rm e}t$ [2]		$4.2^{+2.6}_{-1.4}$	$3.2^{+1.8}_{-0.7}$	$3.3^{+1.8}_{-1.0}$	$5.2^{+110}_{-2.4}$
Temperature [keV]		0.33 ± 0.03	$0.35^{+0.03}_{-0.02}$	0.38 ± 0.02	0.33 ± 0.02
E.M. [3]		$9.5^{+3.2}_{-2.3}$	$9.3^{+2.7}_{-1.0}$	$7.8^{+2.4}_{-2.0}$	$5.3^{+3.0}_{-2.0}$
VNEI 2 (high temperature) [4]					
Temperature [keV]		$3.5^{+1.6}_{-0.9}$	$4.1^{+1.5}_{-1.3}$	$2.7^{+0.4}_{-0.5}$	$2.7^{+0.6}_{-0.7}$
E.M.		0.16 ± 0.02	$0.23^{+0.05}_{-0.04}$	$0.33^{+0.07}_{-0.03}$	$0.17^{+0.05}_{-0.04}$
$N_{\rm H}$ [5]		$7.6^{+0.2}_{-0.4}$	6.5 ± 0.4	$6.3^{+0.2}_{-0.7}$	$7.0^{+0.3}_{-0.6}$
gsmooth					
σ (MOS) [6] [keV]		0.15 ± 0.02	0.14 ± 0.01	0.11 ± 0.01	$0.11^{+0.02}_{-0.03}$
σ (pn) [6] [keV]		$0.21^{+0.04}_{-0.03}$	$0.25^{+0.04}_{-0.03}$	$0.25^{+0.05}_{-0.04}$	$0.17^{+0.04}_{-0.05}$
index [7]		1.0 (fix)	1.0 (fix)	1.0 (fix)	1.0 (fix)
χ^2/d.o.f		242.2 / 262	277.2 / 262	188.9 / 171	120.3 / 146
(reduced χ^2)		(0.92)	(1.06)	(1.10)	(0.82)

[1] Abundances relative to the solar value (Anders & Grevesse, 1989).
[2] Ionization time-scale in units of 10^{11} cm^{-3} s, where $n_{\rm e}$ and t are the electron density and age of the plasma.
[3] Emission measure $E.M. = \int n_e n_H dV \simeq n_e^2 V$ in units of 10^{56} cm^{-3}, where n_e and V are the electron density and the plasma volume. The distance to W28 is assumed to be 1.9 kpc (Velázquez et al., 2002)
[4] Abundances and $n_{\rm e}t$ are constrained to be the same with those of the low temperature component.
[5] Absorption column density in units of 10^{21} cm^{-2}, which is common between the two VNEI components.
[6] Gaussian sigma at 6 keV in a unit of keV.
[7] Energy index of σ, namely, $\sigma \propto E^{-\rm index}$.

bundle of the molecular cloud. The background spectrum is extracted outside W28 as shown in Fig. 5.9 as the dashed box.

The background-subtracted MOS spectra are shown in Figure 5.9. Emission lines are also detected from these inner region spectra, as in the spectra of the north-eastern shell and the south-eastern rim. We therefore fitted them with a two-temperature VNEI model with photoelectric absorption with a single value of $N_{\rm H}$. In addition, two Gaussian emission lines at 1.2 keV and 1.5 keV were added, as in the analysis of the south-eastern rim region. Abundances of O, Ne, Mg, Si, S, Fe, and ionization time-scale $n_{\rm e}t$ are set free, but are constrained to be common between the two VNEI components. The best-fit parameters are summarized in table 5.3 and the best-fit models overlaid on the observed spectra and the fit residuals are displayed in figure 5.9. The residuals in these fits are

shown in black in the middle panels. The two-temperature VNEI model well described the spectra, with a resultant χ^2_ν ranging from 0.82 to 1.10. As noticed from this table, all regions share temperature of $\sim$0.35 keV for the low temperature component. The abundances are sub-solar for O, Ne, and Fe in the range 0.4–0.8$Z_\odot$, close to solar for Mg, and super-solar for Si and S in the range 1.3–2.4$Z_\odot$. The ionization parameters $n_{\rm e}t$ are $\sim 10^{11}$ cm^{-3}s for all regions. The absorption column density at region D, which encircles the northern bundle of the molecular cloud, is same as in the other molecular-cloud-free inner regions.

The temperature of the higher temperature component, on the other hand, show larger variation, resulting in $\sim$4 keV in region A and B, and 2.7 keV in region C and D, respectively. The high temperature emission is often to be observed from a young SNR, like historical SNRs Tycho ($kT_{\rm e} \sim 4.7$ keV; Tamagawa et al. (2009)), Cas A ($kT_{\rm e} = 1.5-4.0$ keV; Maeda et al. (2009)), and so on. However, W28 is a middle-aged SNR with several times 10^4 years (Rho & Borkowski, 2002). We thus assumed that the origin of hard component is non-thermal. Hence we substituted a power-law model for the VNEI model. The best-fit parameters are summarized in table 5.4, and residuals between data and the model are displayed in the lowest panels of the spectra in Fig. 5.9 in red. The parameters of the lower-temperature VNEI component are the same as the case of the two-temperature VNEI model fitting. The photon indices ($\sim$3) are common among the four regions within statistical error. The intrinsic fluxes between 2–10 keV are $\sim 10^{-13}$ ergs/cm^{2}s for all regions.

We obtained similarly good fit whether a power-law or VNEI model is adopted for the high temperature component. In order to distinguish these two possibilities, we focused on the iron Kα emission line in the 6–7 keV band. If a significant line is detected, the high temperature component is probably thermal origin. To increase statistics, we extracted the spectra by combining regions A and B, where the temperatures are particularly high. We first fitted the 0.3–10 keV band spectrum with a two-temperature VNEI model to determine the parameters of the low-temperature component. Abundances are constrained to be common between the two VNEI components. The best-fit parameters are summarized in table 5.5. The parameters are roughly average of those obtained from individual fitting of region A and B. We next fitted the spectrum in the 2–10 keV band since the high-temperature component is dominant above 2 keV. The temperature, iron abundance, and normalization of high-temperature component are set free. Others are fixed to the best-fit values obtained from the fitting in the 0.3–10 keV band. The best-fit parameters are summarized in table 5.5, and the best-fit model as well as the residual is displayed in figure 5.10. The obtained iron abundance of the hard component is $0.69^{+0.83}_{-0.67}$. Because of the relatively large uncertainty in the abundance, we could not distinguish whether the hard-tail component is thermal or non-thermal by the spectral fitting. In spite of this result, we consider that we do not need to change the interpretation made in the previous paragraph, i.e, the hard component has non-thermal origin, since the temperature is much higher than those seen in the typical middle-aged SNRs.

5.4.4 TeV γ-ray Region

We investigated X-ray spectrum of a region where intense TeV γ–ray emission is detected in spite of no apparent X-ray emission. In Fig. 5.11(a) shown are the TeV γ-ray intensity contours (the same as in Fig. 5.5, Aharonian et al. (2008a)) overlaid on the X-ray gray-

Table 5.4: Best-fit parameters of the inner spectra with VNEI + power-law model.

Parameters		Region A	Region B	Region C	Region D
VNEI 1 (low temperature)					
abundance [1]	O	$0.43^{+0.09}_{-0.11}$	$0.44^{+0.16}_{-0.10}$	$0.50^{+0.31}_{-0.16}$	$0.39^{+0.37}_{-0.14}$
	Ne	$0.62^{+0.20}_{-0.14}$	$0.90^{+0.19}_{-0.18}$	$0.95^{+0.36}_{-0.32}$	$0.80^{+0.52}_{-0.27}$
	Mg	$0.84^{+0.19}_{-0.18}$	1.2 ± 0.2	$1.1^{+0.6}_{-0.3}$	$0.97^{+0.84}_{-0.31}$
	Si	1.4 ± 0.3	$1.6^{+0.7}_{-0.4}$	$1.6^{+1.1}_{-0.6}$	$1.6^{+1.6}_{-0.6}$
	S	$2.4^{+1.7}_{-1.1}$	$3.2^{+1.1}_{-1.3}$	$4.3^{+4.0}_{-1.8}$	$5.0^{+6.4}_{-2.5}$
	Fe	$0.49^{+0.07}_{-0.09}$	$0.51^{+0.06}_{-0.04}$	$0.65^{+0.36}_{-0.18}$	$0.56^{+0.38}_{-0.16}$
$n_{\rm e}t$ [2]		$3.6^{+1.9}_{-1.2}$	$2.6^{+1.4}_{-0.7}$	$2.6^{+1.2}_{-0.6}$	$3.1^{+3.4}_{-1.2}$
Temperature [keV]		$0.35^{+0.01}_{-0.02}$	$0.37^{+0.01}_{-0.02}$	$0.41^{+0.04}_{-0.02}$	$0.37^{+0.05}_{-0.02}$
E.M. [3]		$7.1^{+1.5}_{-1.9}$	$6.8^{+2.5}_{-1.8}$	$5.3^{+2.2}_{-1.8}$	$3.0^{+1.2}_{-0.8}$
Power-law					
Γ		2.8 ± 0.5	2.5 ± 0.4	3.0 ± 0.3	$2.9^{+0.5}_{-0.4}$
Intrinsic Flux [4]		2.9 ± 0.5	$5.0^{+0.9}_{-0.8}$	$5.0^{+0.8}_{-0.4}$	2.7 ± 0.6
$N_{\rm H}$ [5]		$7.2^{+0.2}_{-0.3}$	6.2 ± 0.4	$5.9^{+0.4}_{-0.3}$	$6.5^{+0.6}_{-0.7}$
gsmooth					
σ (MOS) [6] [keV]		0.15 ± 0.02	$0.14^{+0.02}_{-0.01}$	$0.10^{+0.02}_{-0.01}$	$0.10^{+0.02}_{-0.03}$
σ (pn) [6] [keV]		$0.21^{+0.02}_{-0.03}$	$0.25^{+0.04}_{-0.01}$	$0.24^{+0.03}_{-0.02}$	$0.16^{+0.05}_{-0.04}$
index [7]		1.0 (fix)	1.0 (fix)	1.0 (fix)	1.0 (fix)
χ^2/d.o.f		247.9 / 262	289.4 / 262	211.4 / 171	129.8 / 146
(reduced χ^2)		(0.95)	(1.10)	(1.24)	(0.89)

[1] Abundances relative to the solar value (Anders & Grevesse, 1989).
[2] Ionization time-scale in units of 10^{11} cm^{-3} s, where $n_{\rm e}$ and t are the electron density and age of the plasma.
[3] Emission measure $E.M. = \int n_e n_H dV \simeq n_e^2 V$ in units of 10^{56} cm^{-3}, where n_e and V are the electron density and the plasma volume. The distance to W28 is assumed to be 1.9 kpc (Velázquez et al., 2002)
[4] Flux in the 2.0–10.0 keV band in units of 10^{-13} ergs cm^{-2} s^{-1}.
[5] Absorption column density in units of 10^{21} cm^{-2}.
[6] Gaussian sigma at 6 keV in a unit of keV.
[7] Energy index of σ, namely, $\sigma \propto E^{-\rm index}$.

Table 5.5: Best-fit parameters of the W28 region A + B spectra with two temperature thermal emission model

Parameters		0.3–10 keV band fit	2–10 keV band fit
VNEI 1 (low temperature)			
abundance [1]	O	$0.45^{+0.08}_{-0.07}$	0.45 (fix)
	Ne	$0.68^{+0.05}_{-0.09}$	0.68 (fix)
	Mg	$0.89^{+0.07}_{-0.11}$	0.89 (fix)
	Si	1.5 $\pm$0.3	1.5 (fix)
	S	$2.2^{+0.6}_{-0.5}$	2.2 (fix)
	Fe	$0.49^{+0.07}_{-0.05}$	0.49 (fix)
$n_{\rm e}t$ [2]		$3.9^{+1.1}_{-0.9}$	3.9 (fix)
Temperature [keV]		$0.34^{+0.02}_{-0.01}$	0.34 (fix)
E.M. [3]		$23^{+3.9}_{-3.8}$	23 (fix)
VNEI 2 (high temperature)			
abundance [1]	Fe	0.49 [7]	$0.69^{+0.83}_{-0.67}$
Temperature [keV]		3.7 $\pm$0.5	$3.4^{+0.6}_{-0.4}$
E.M. [3]		$0.44^{+0.06}_{-0.06}$	$0.42^{+0.03}_{-0.04}$
$N_{\rm H}$ [4]		$7.1^{+0.2}_{-0.3}$	7.1 (fix)
gsmooth			
σ (MOS) [5] [keV]		0.14$\pm$0.01	0.14 (fix)
σ (pn) [5] [keV]		$0.23^{+0.01}_{-0.02}$	0.23 (fix)
index [6]		1.0 (fix)	1.0 (fix)
χ^2/d.o.f		374.4 / 250	42.9 / 58
(reduced χ^2)		(1.50)	(0.74)

[1] Abundances relative to the solar value (Anders & Grevesse, 1989).
[2] Ionization time-scale in units of 10^{11} cm^{-3} s, where $n_{\rm e}$ and t are the electron density and age of the plasma.
[3] Emission measure $E.M. = \int n_e n_H dV \simeq n_e^2 V$ in units of 10^{56} cm^{-3}, where n_e and V are the electron density and the plasma volume. The distance to W28 is assumed to be 1.9 kpc (Velázquez et al., 2002)
[4] Absorption column density in units of 10^{21} cm^{-2}.
[5] Gaussian sigma at 6 keV in a unit of keV.
[6] Energy index of σ, namely, $\sigma \propto E^{-\rm index}$.
[7] Common with the value of VNEI 1 component.

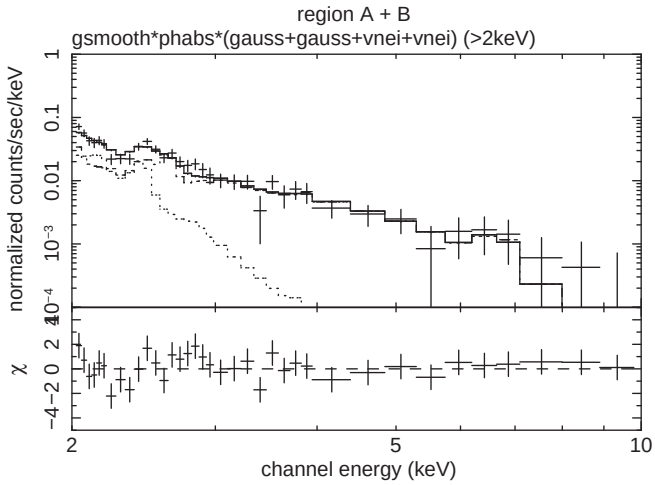

Figure 5.10: Region A + B spectrum in the 2–10 keV band with the best-fit 2 VNEI models.

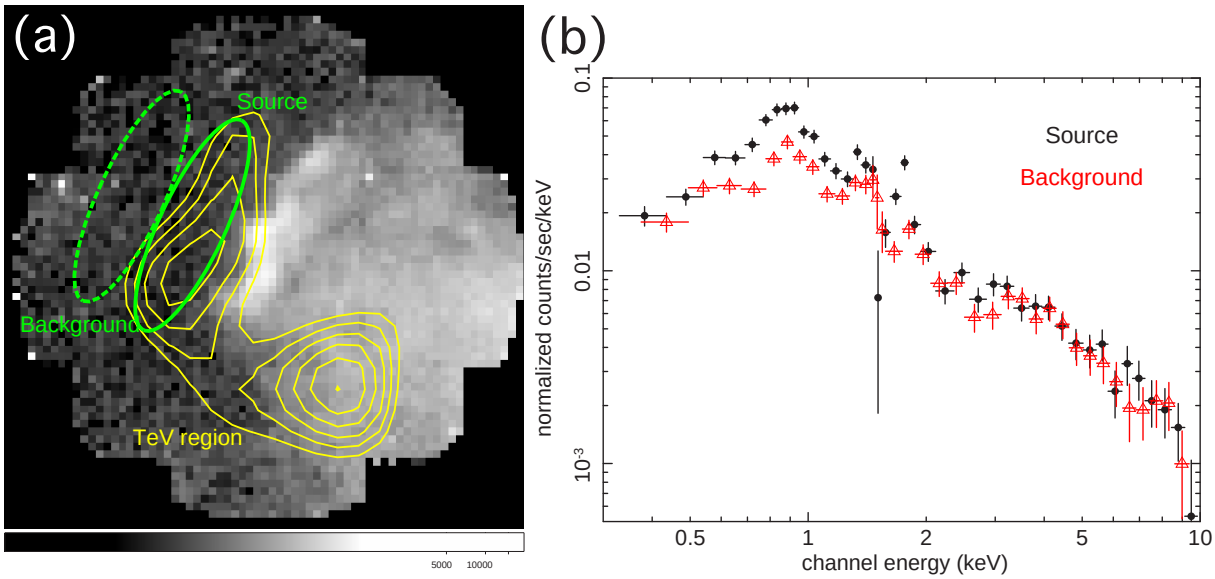

Figure 5.11: Integration regions and resultant spectra of the north-eastern TeV γ-ray peak. (a) The source and background integration regions are drawn in green. They are an ellipse with a semi major and minor axis of 6′.6 and 1′.9, respectively. (b) The source (black) and background (red) spectra with the MOS instruments. NXB spectrum extracted from out of field of view is already subtracted. The source spectrum below 2 keV is contaminated by the thermal emission from the north-eastern rim.

scale image. Although the TeV γ-ray surface brightness has a dual peak structure,we concentrated on the north-eastern peak, and extracted the source spectrum from the ellipse region located at $(l, b) \simeq (6.^{\circ}75, -0.^{\circ}30)$, as shown in Fig. 5.11(a) in green, because the southern peak centered at $(l, b) \simeq (6.^{\circ}56, -0.^{\circ}26)$ is partly included in the south-eastern rim (§ 5.4.2), which region is found to be contaminated by the thermal emission from W28. The choice of the source integration region adopted here also intends to excludes the

thermal emission from the north-eastern shell region (§ 5.4.1). We note that this source region was used as the background region for the south-eastern shell analysis (§5.4.2). The dashed ellipse is, on the other hand, a background region. Figure 5.11(b) shows the source and background spectra thus extracted, from which the Non X-ray Background (NXB) spectrum evaluated out of the telescope field of view are already subtracted. Even we took care of intrusion of the thermal emission from the north-eastern rim region, we found significant excess in the source spectrum below 2 keV. Since we are interested in non-thermal emission associated with the TeV γ-ray emission, we hereafter use the data only in the band 2–10 keV.

The effective area of the background region is smaller than the source region due to telescope vignetting. We checked the vignetting effect by using the Lockman Hole archival data observed on 2002 December 27 to 29 (Obs ID = 0147511601) with the total effective exposure time of 110 ksec. A count ratio of the background to source regions at the same detector positions was found to be 0.88 in the 2–10 keV band. In evaluating flux of the possible non-thermal X-ray emission, we first tried to fit the background spectrum with a two power-law model, and found photon indices of 0.85 and -5.8, respectively. The source spectrum was fitted with a model comprising of the two power-law models with the normalizations being multiplied by the vignetting-correction factor, and an additional power-law model representing the putative non-thermal X-ray emission, with the photon index of 2.66 which is the same as that in the TeV γ-ray band (Aharonian et al., 2008a). Consequently, we only obtained an upper limit for the non-thermal X-ray emission. The upper limit flux in the 2–10 keV band is obtained to be $\leq 2.1 \times 10^{-14}$ ergs cm^{-2} s^{-1}.

5.5 Discussion

By the spectral fitting, hard-tail X-ray was discovered only from inner region. We concluded that this component probably has non-thermal origin. Diffuse thermal emission was detected from not only inner but shell region. Here we reveal the nature of the thermal component and discuss the origin of non-thermal component. We also present the study of wide-band spectrum of north-eastern peak of TeV γ-ray region.

5.5.1 The Nature of the Thermal Component

We found the $\sim$0.3 keV thermal emission from the north-eastern shell and the inner regions (and the south-eastern rim region) from the spectral analysis. Table 5.6 summarizes pre-shock electron density (n_0), number of electrons ($N_{\rm e}$), mass, and thermal energy ($E_{\rm thermal}$), on the basis of the best-fit parameters summarized in table 5.1 and table 5.4. We assume that the distance to W28 is 1.9 kpc (Velázquez et al., 2002), and the plasma distributes uniformly along the line of sight. In the shell regions, the shape is assumed an oval with the line-of-sight extent being the same as the semi-minor axis appearing on the image ($r_{\rm s}$). The volumes are calculated to be equal to $(4/3)\pi r_{\rm l} r_{\rm s}^2$, where $r_{\rm l}$ is the length of the semi-major axis on the image. The volumes of the inner regions were estimated as a rectangular parallelepiped (region A, B, C) or a cylindrical column (region D) multiplying a length along the line-of-sight on the assumption that the inner region of W28 is a sphere. With the aid of the emission measure ($EM = \int n_{\rm e} n_{\rm H} dV$) obtained from the spectral fitting and V, we calculated $n_{\rm e}$, taking into account $n_{\rm e} \approx 1.24 n_{\rm H}$ for fully ionized solar

Table 5.6: Thermal parameters of W28 from spectral fitting

Regions	V [cm^3] [1]	n_0 [cm^{-3}] [2]	$n_e t$ [10^{11}cm^{-3}s] [3]	N_e [10^{56}]	Mass [$M_\odot$]	$E_{thermal}$ [10^{48}erg]
Shell						
1	3.7×10^{55}	$0.62^{+0.11}_{-0.09}$	98 (>4)	$0.90^{+0.16}_{-0.14}$	$0.073^{+0.013}_{-0.011}$	0.15 ±0.03
2	3.7×10^{55}	1.5 ±0.1	11 (>6)	2.1 ±0.2	0.17 ±0.02	0.29 ±0.03
3	4.5×10^{55}	1.9 ±0.1	50 (>9)	3.5 ±0.3	0.29 ±0.02	0.45 ±0.04
Inner						
A	3.0×10^{57}	0.14 ±0.02	$3.6^{+1.9}_{-1.2}$	16 ±2	$1.3^{+0.1}_{-0.2}$	$2.6^{+0.3}_{-0.4}$
B	5.6×10^{57}	$0.098^{+0.018}_{-0.013}$	$2.6^{+1.4}_{-0.7}$	22^{+4}_{-3}	$1.8^{+0.3}_{-0.2}$	$3.7^{+0.7}_{-0.5}$
C	6.0×10^{57}	$0.083^{+0.018}_{-0.015}$	$2.6^{+1.2}_{-0.6}$	20^{+4}_{-3}	1.6 ±0.3	$3.7^{+0.8}_{-0.7}$
D	3.0×10^{57}	$0.088^{+0.018}_{-0.013}$	$3.1^{+3.4}_{-1.2}$	11^{+2}_{-1}	$0.86^{+0.17}_{-0.12}$	$1.8^{+0.4}_{-0.3}$
Total	1.8×10^{58}	—	—	75^{+6}_{-5}	$6.1^{+0.5}_{-0.4}$	13 ±1

[1] Volumes were calculated on the assumption that the shell regions are an oval, region A, B, C are a rectangle parallelepiped and region D is a cylindrical column. See the text for more detail.
[2] Pre-shock electron density. Post-shock electron density were obtained by using *E.M.* and the volume. We assume strong shock that a forward-shock plasma is 4 times compressed than the upstream medium.
[3] Ionization parameters ($n_e t$) were found from the spectral fitting with a VNEI model as explained in § 5.4.

abundance plasma. Assuming the strong shock, pre-shock electron density is obtained to be n_0=n_e/4. The number of electrons ($N_e = n_e V$), the total mass and the thermal energy ($E_{thermal} = \frac{3}{2}(N_e + N_H + N_{He})kT$) were obtained under the assumption of energy equipartition between electrons and ions. The total thermal energy should be larger if other portions of the remnant are included, and if the proton temperature is significantly larger than the electron temperature as is expected for supernova remnants with large shock velocities (Ghavamian et al., 2007).

As noticed from this table, n_0 is much higher in the north-eastern shell regions ($1 \sim 2$ cm^{-3}) than in the inner regions ($\sim$0.1 cm^{-3}) by a factor of $\sim$10. In particular, shell region 3, which apparently interacts with a molecular cloud (see Fig. 5.4 and 5.5), has the largest n_0. The temperature and the electron density of the north-eastern shell regions are plotted in Fig. 5.12. The higher temperature region has lower density. This is probably because the original ejecta energy is distributed among larger amount of interstellar matter for higher density regions, as indicated by the total mass in the table. The ionization parameters are, on the other hand, larger in the shell regions with $n_e t \sim 10^{13}$ s/cm^3 than in the inner regions with $n_e t \sim 10^{11}$ s/cm^3. This the result of slow ionization due to low electron density in the inner regions. The plasma age obtained with the combination of $n_e t$ and n_e to be several times 10^4 year for both the shell and inner regions. The total volume of the region covered with the current study is about 5% of the whole SNR on the assumption that W28 is a sphere with a radius of 13 pc. Given that the mass and the total energy in the north-eastern shell and inner regions are 6.1 $M_\odot$ and 1.3×10^{49} ergs, respectively (table 5.6), the mass and the thermal energy of the entire SNR are estimated to be $\sim$120 $M_\odot$ and $\sim 2.6\times10^{50}$ ergs, respectively. On the assumption that the electron density of the interstellar medium before a supernova expansion is 1 cm^{-3}, the total swept up mass by the shock is $\sim$200 $M_\odot$, which is roughly consistent with the mass estimate obtained from our spectral analysis.

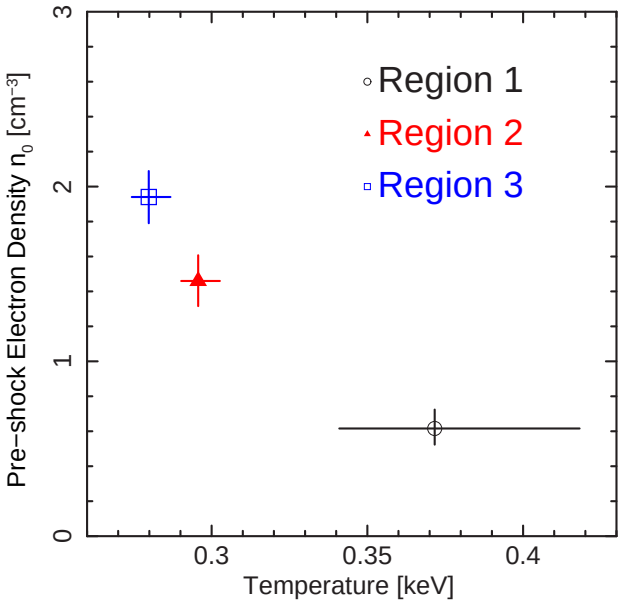

Figure 5.12: Relation between the temperature and the pre-shock electron density of shell regions.

5.5.2 On the Origin of Hard X-ray Spectrum

Let us consider the emission mechanism of the hard X-ray component detected from the inner regions. We suggested that this component is probably non-thermal emission, as demonstrated in §5.4.3.

There are a few possibilities to explain the non-thermal X-ray emission from the observed region of W28. One is, of course, synchrotron emission from shock-accelerated electrons. If the non-thermal emission detected from the inner regions is synchrotron X-ray from primary electrons, their cooling time of synchrotron photon ($t_{\rm cool,synch}$) can be estimated by using eq.(2.27) and eq.(2.31),

$$t_{\rm cool} = 4.3 \times 10^3 \left(\frac{B}{10\,\mu{\rm G}}\right)^{-1.5} \left(\frac{\epsilon}{1\,{\rm keV}}\right)^{-0.5} \ [{\rm yr}], \tag{5.1}$$

where ϵ is a synchrotron photon energy. With a few μG magnetic field, $t_{\rm cool}$ is $\sim 10^4$ yr which is consistent with the age of W28 (§ 5.5.1). Thus the observed power-law X-ray emission can be interpreted as the synchrotron emission from primary electrons. We suggest one possibility that electrons were accelerated at the shock front passing through the inner regions ages ago, and stayed there. There is a trend that the photon indices of the power-law model are larger for regions with larger separation from the north-eastern shell region (see table 5.4). The softened spectrum is probably caused by the cooling effect of the electrons because the acceleration occurred earlier near the center. In addition, the photon indices are $\sim$3.0 for all inner regions. On the other hand, the expected photon index of synchrotron emission from electrons with a power-law number index of 2.0 expected from DSA (see §2.3.1), is 1.5. This spectrum steepening is probably caused by the cooling effect. Takahashi et al. (2008) reported the case of SNR RX J1713.7-3949, in which the photon indices of power law are 2.4 in the 0.4–12 keV and 3.2 in the 12–40 keV, which difference is presumably caused by synchrotron cooling. They argued

that the cutoff energy is in the range of 1–9 keV. The age of W28 is older than that of RX J1713.7-3949 (the age of RX J1713.7-3949 is believed to be ∼1000 yr; e.g. Wang et al. (1997)), thus the cutoff energy can be lower in the case of W28 than RX J1713.7-3949, and the spectral steeping can be seen below 10 keV.

Secondly, since the observed region of W28 contains a lot of molecular clouds, it is possible that the observed power-law X-ray emission is a synchrotron emission from secondary electrons produced by collisions of the accelerated protons with molecular cloud gas followed by pion decay. It is also possible that the primary electrons make non-thermal bremsstrahlung. In these cases, however, the observed non-thermal emission should correlate spatially with the molecular clouds. Contrary to this expectation, we detected no power-law X-ray emission from the south-eastern rim region (§ 5.4.2) which overlaps with a molecular cloud. Note that we detected the power-law X-ray emission from inner region D in which a bundle of the molecular cloud is included. Nevertheless, the power-law intensity in region D is not enhanced compared with the adjacent region A through C, which are set out of the molecular clouds. The hard band image (Fig. 5.7(b)) does not show any apparent correlation with the molecular cloud distribution.

All these facts suggest that the non-thermal X-ray emission detected from the inner regions is the synchrotron X-ray emission from the primary electrons. We note that the thermal electron densities of the inner regions, where the non-thermal emission was detected, are lower than ∼0.5 cm^{-3} (table 5.6). This is consistent with a picture that efficient electron acceleration takes place only in a shock wave generated in a low density environment (Bamba et al., 2008b; Nakamura et al., 2009; Ellison et al., 2000). Non detection of non-thermal X-ray from shell regions, which have high electron density, also supports this picture.

5.5.3 The Relation with TeV γ-ray Emission

We obtained the upper limit of the X-ray flux from the TeV γ-ray emission region in § 5.4.4. Figure 5.13 shows the spectral energy distribution of the TeV γ-ray and the X-ray flux upper limit in the region. The red line is the TeV γ-ray power-law spectrum (Aharonian et al., 2008a) with a photon index of 2.66, while the blue line is the upper limit of the X-ray power-law spectrum with a photon index the same as that in the TeV band. The TeV flux is renormalized to that of the X-ray flux by taking the difference in the integration region into account (the X-ray region is the $6\farcm6 \times 1\farcm9$ ellipse while the TeV γ-ray integrated region in Aharonian et al. (2008a) is a circle with a radius of $11\farcm8$). The corrected TeV γ-ray flux is 3.3×10^{-13} ergs cm^{-2} s^{-1} in the 1–10 TeV band.

We assumed that the TeV γ-ray emission is powered through 1-zone Inverse Compton scattering (IC) of the cosmic microwave background off the accelerated electrons, and the electrons emit synchrotron radiation in the X-ray band. The characteristic energy of synchrotron photons ϵ, and of IC photons E produced by an electron are related as

$$\epsilon \simeq 0.07 \left(\frac{E}{1\ \mathrm{TeV}}\right)^2 \left(\frac{B}{10\ \mu\mathrm{G}}\right)\ \ [\mathrm{keV}], \tag{5.2}$$

where B is the magnetic field (Aharonian et al., 1997). The flux ratio of the synchrotron flux (f_{sync}) and inverse Compton flux (f_{IC}) at these energies can be determined solely by

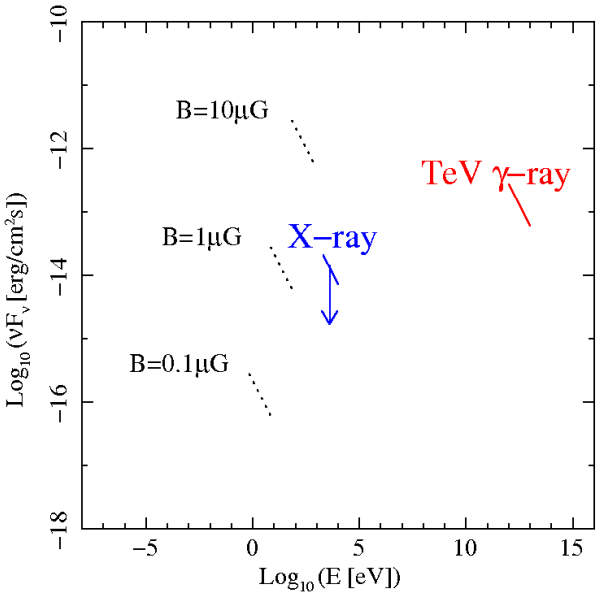

Figure 5.13: Spectrum energy distribution of TeV γ–ray region from the X–ray (in blue) and TeV γ–ray (in red) bands. A photon index is 2.66 for both spectra. The dashed plots are the synchrotron radiation models with various magnetic field.

the magnetic field strength (Aharonian et al., 1997) as

$$\frac{f_{\rm IC}}{f_{\rm sync}} \simeq 0.1 \left(\frac{B}{10\ \mu{\rm G}}\right)^{-2} . \tag{5.3}$$

We draw synchrotron X-ray spectra with various magnetic field (B = 0.1, 1.0, and 10.0 μG) in Fig. 5.13 in dashed lines. We only obtained the upper limit of the magnetic field of $\leq$5 μG. This might be a little too weak for particle acceleration region, although it is possible that electrons accelerated in the past escape from the acceleration region and emit IC photons in the observed position where the magnetic field is weak. However, the TeV γ-ray emission region well coincides with the distribution of the molecular cloud, as demonstrated in § 5.3 (Fig. 5.5). This suggests that TeV γ-ray is emitted through the decay of pions generated by the high energy proton impact to the molecular clouds.

We then try to calculate a spectral energy distribution from X-ray to TeV γ-ray based on the pion decay (see §2.3.4). The resultant γ-ray spectrum depends on an energy distribution function of the accelerated protons

$$\frac{dN}{dE} = C\,E^{-p}\exp(-E/E_{\rm max,p}) \ \ (E_{\rm min,\,p} < E), \tag{5.4}$$

and the density of the molecular cloud. Here we set the minimum proton energy at the rest mass of proton ($E_{\rm min,\,p} = m_{\rm p}c^2$ = 938 MeV). It is well known that the resultant γ-ray energy is proportional to that of the bombarding proton and hence we can simply adopt the number index p be equal to the photon index of the observed TeV γ-ray (p = 2.66). We assume the distance to W28 to be 1.9 kpc (Velázquez et al., 2002) to constrain the normalization C. The density of the molecular cloud is measured from the CO observation

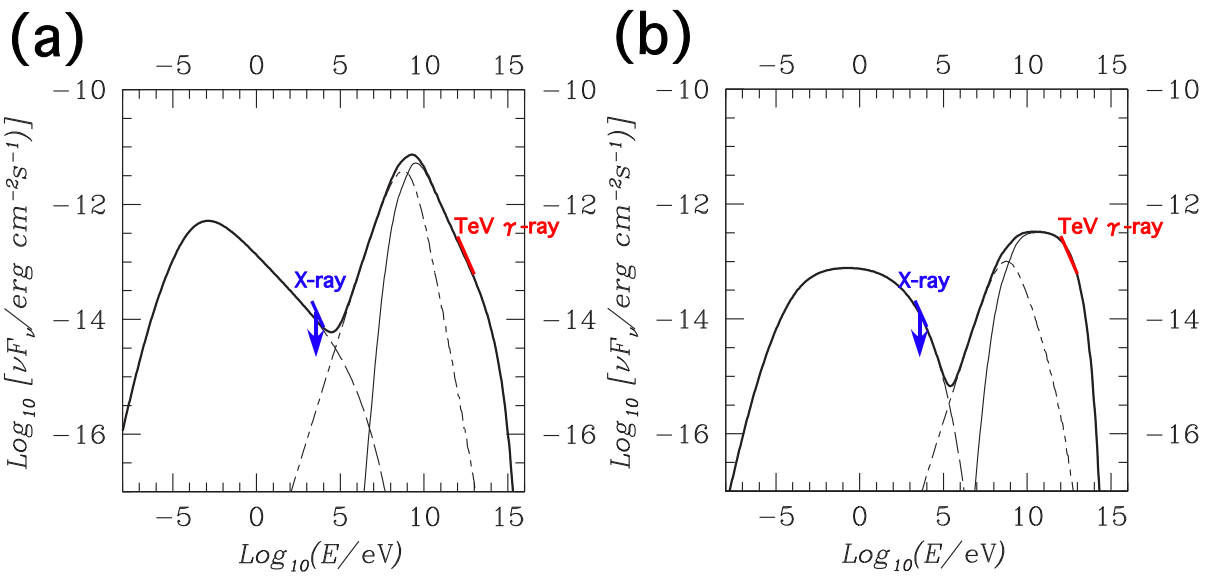

Figure 5.14: Spectra of hadronic emissions with the age, the distance and the number density of molecular cloud of $t_{\rm age}$=30000 yr, D=1.9 kpc and $n_{\rm mc}$=1000 cm^{-3}, respectively. Emissions are π^0-decay γ-ray (solid line), bremsstrahlung (dot-dashed line) and synchrotron (dashed line) emission from secondary electrons produced by charged pions. Total emissions are shown in bold line. Blue and red line show upper limit X-ray and TeV γ-ray spectra. (a) With proton number index p=2.66, maximum proton energy $E_{\rm max,p}$=1000 TeV, total energy $E_{\rm total}$=3.0 $\times 10^{47}$ erg, and magnetic field $B \leq$ 800 μG. (b) With p=2.0, $E_{\rm max,p}$=40 TeV, $E_{\rm total}$=8.1 $\times 10^{45}$ erg, and $B \leq$ 1500 μG.

(Arikawa et al., 1999), which is 10^3 cm^{-3}. With these parameters, we fitted the observed TeV γ-ray spectrum, and found that $E_{\rm max,\,p} \geq 10^{15}$ eV. The total energy of the accelerated protons is obtained to be 3.0×10^{47} erg, which is much smaller than the supernova explosion energy ($\simeq 10^{51}$ erg). The result is displayed in Fig. 5.14(a). Note that non-thermal bremsstrahlung originating from secondary electrons produced through collisions between the accelerated protons and the molecular cloud neutrons contribute significantly to the resultant spectrum, although it dominates somewhat lower energy. Given $E_{\rm max,\,p}$ and the energy distribution of the secondary electrons, which can be calculated from that of the protons, and the absence of the synchrotron X-ray emission, we can set the upper limit on the magnetic field strength. By referring to the upper limit of the X-ray flux, we have obtained $B \leq$800 μG. We remark that this upper limit of the magnetic field was obtained by setting $E_{\rm max,\,p} = 10^{15}$ eV. In the case of $E_{\rm max,\,p} > 10^{15}$ eV, the model synchrotron spectrum is enhanced and extends to higher energy without being cutoff in the X-ray band. Consequently, a weaker magnetic field is required for the model synchrotron X-ray spectrum to be accommodated with the X-ray flux upper limit. The upper limit B =800 μG is therefore the most conservative one in the case of p=2.66. The B =800 μG case is shown in Fig. 5.14(a). The obtained parameters are summarized in table 5.7.

We note that, at the old SNR shocks with low shock velocity, the maximum energy of accelerated particles may be smaller due to the escape of high energy protons (e.q. Ohira et al. (2009)). We thus have tried to calculate a spectrum in the case that the number index of the proton is equal to the canonical value of the Fermi acceleration $p = 2.0$ in the

Table 5.7: Physical parameters obtained with hadronic model fitting

Proton number index (p)	(a) 2.66	(b) 2.0
Maximum proton energy ($E_{\rm max,p}$) [TeV]	≥ 1000	40
Total energy ($E_{\rm total}$) [erg]	3.0×10^{47}	8.1×10^{45}
Magnetic field (B) [μG]	≤ 800	≤ 1500
Photon flux in the 0.1–1 GeV [ph/cm^{2}s]	2.3×10^{-8}	6.3×10^{-10}
in the 1–100 GeV [ph/cm^{2}s]	4.1×10^{-9}	1.6×10^{-10}

lower energy side. In this case, we adjust $E_{\rm max,\,p}$ so that the resultant model spectrum can be fitted to the observed TeV γ-ray spectrum. The result of the maximum B case is shown in Fig. 5.14(b). The maximum proton energy is found to be $E_{\rm max,\,p} = 40$ TeV, and the total proton energy is 8.1×10^{45} erg, which is again much smaller than the supernova explosion energy. The upper limit of the magnetic field strength is $B \leq$1500μG.

Abdo et al. (2009) reported based on the *Fermi* observation that the integrated photon fluxes in the bands 0.1–1 GeV and 1–100 GeV are 7.42×10^{-7} photons cm^{-2} s^{-1} and 4.51×10^{-8} photons cm^{-2} s^{-1}, respectively. On the other hand, the photon fluxes in the same energy bands in our models are calculated to be 2.0×10^{-8} ph cm^{-2} s^{-1} and 2.7×10^{-9} ph cm^{-2} s^{-1}, respectively, for the case of Fig. 5.14(a), and 5.6×10^{-10} ph cm^{-2} s^{-1} and 2.0×10^{-10} ph cm^{-2} s^{-1}, respectively, for the case of Fig. 5.14(b), shown in table 5.7, both of which are smaller than the values obtained by *Fermi*. This is because the source integrated region of *Fermi* is larger than and slightly different from our integrated region (Fig. 5.11a). Hence, the flux of our models can be regarded as being consistent with that of the GeV emission.

5.6 Summary of W28

We analyzed the *XMM-Newton* data of the north-eastern part of the supernova remnant W28. The observed X-ray image is composed of the bright and twisted north-eastern shell and the inner emission region which is part of the center-filled emission brightening toward the south-west end of the field of view.

The north-eastern shell region is found to reach ionization-equilibrium state and can be fitted well with a single temperature optically thin thermal emission model with kT of $\simeq$0.3 keV. From the emission measure and the apparent volume, the pre-shock electron density is found to be as high as $\simeq$2 cm^{-3}. Since a bunch of molecular cloud spatially coincides with the outer edge of a part of the shell, this high density is probably brought about by collision of the plasma with the molecular cloud.

The thermal emission with a temperature of $\simeq$0.3 keV is also detected from the inner region, although it is slightly deviated from ionization equilibrium, with an ionization time scale $n_{\rm e}t$ of $\simeq 10^{11}$ cm^{-3}s. This ionization time scale together with the emission measure results in pre-shock density of thermal electrons to be $\sim$0.1 cm^{-3}, and consequently, the age of this SNR is obtained to be several times 10^4 yr. Moreover, we have discovered a hard-tail X-ray, which is likely to be a non-thermal power-law emission with a photon index of $\sim$3, from the inner region of this old SNR. Since there is no evidence of interaction with any molecular clouds, this emission is probably synchrotron X-ray emission

emanating from primary electrons accelerated in the shock wave.

In contrast, there is no significant X-ray emission from one of the TeV γ-ray peaks. We only obtained the upper limit flux of $<2.1\times 10^{-14}$ erg cm^{-2} s^{-1} in the 2–10 keV band, assuming a power-law spectrum with the same photon index as in the TeV γ-ray ($= 2.66$). The spatial coincidence of the molecular cloud and TeV γ-ray emission site suggests that TeV γ-ray is hadronic origin. We calculate the hadronic process spectra, and found that π^0-decay emission is dominant in TeV γ-ray band. A weak upper limit on the magnetic field strength is obtained $B \leq 1500\mu$G from the X-ray flux upper limit.

Chapter 6

Analysis of CTB37B

6.1 Overview of CTB37B

CTB37B (G348.7+0.3) is a shell-type supernova remnant which was discovered in radio band (Clark et al., 1975). It is located at (l, b) = (348.°7, +0.°3) with a distance of 10.2 ± 3.5 kpc (Caswell et al., 1975). Figure 6.1 (a) shows the 333 MHz radio map of CTB37 complex region adapted from Kassim et al. (1991). CTB37B has the partial radio shell with a radius of $\sim 5'$, corresponding to a physical radius of $\sim$15 pc at the distance of 10.2 kpc. This region is one of the most active regions in our Galaxy where star-burst activities, a number of shell structures probably associated with recent SNRs and OH maser sources (Frail et al., 1996) are detected in radio band. Since the TeV γ-ray source, which is named "HESS J 1713-381", was detected by the H.E.S.S. observation (Aharonian et al., 2006), the region has been reobserved with H.E.S.S., and the results were reported by Aharonian et al. (2008b). Figure 6.1 (b) shows the TeV γ-ray excess map of CTB37 complex quoted from Aharonian et al. (2008b). A morphological fit of "HESS J1713-381" was made with a model consisting of two Gaussian emission profiles convolved with the PSF of the instrument. The intrinsic rms width extracted from this fit is $2.'6 \pm 0.'8$, which is compatible with a shell-like structure with a radius $\sim 4'$–$6'$, consistent with the estimated radio shell size. Aharonian et al. (2008b) suggested that the origin of TeV γ-ray emission is the decay of neutral pions produced in proton-proton interaction in the region of the SNR shell, based on the morphology and the flux of TeV γ-ray observational results. In spite of the evidence of the high activities in other wave bands, X-ray observations have been relatively poor. Only ASCA (Tanaka et al., 1994) has detected a part of CTB37B at the edge of the field of view of the Gas Imaging Spectrometer (GIS) (Ohashi et al., 1996; Makishima et al., 1996) in the course of the galactic plane survey (Sugizaki et al., 2001; Yamauchi et al., 2008). Although the statistics are limited, and the response of the GIS is not qualified at the pointing position of CTB37B, Yamauchi et al. (2008) represented that the fit of a power law to the GIS spectrum results in a steep photon index of $\sim$4.1, whereas fit of an optically thin thermal plasma model requires a high temperature of $\sim$1.6 keV. These results strongly suggest that the X-ray spectrum is a mixture of a non-thermal power law and an optically thin thermal plasma emission. In addition, Aharonian et al. (2008b) resolved a bright point source located near the shell of CTB37B from the diffuse emission by *Chandra*, although its spectral parameters are not constrained very well because of the short exposure time. Halpern & Gotthelf (2009) discovered the spin period of this source to be $P = 3.82$ sec by using new *Chandra* observation data in

continuous clocking (CC) mode, which has 2.85 msec timing resolution.

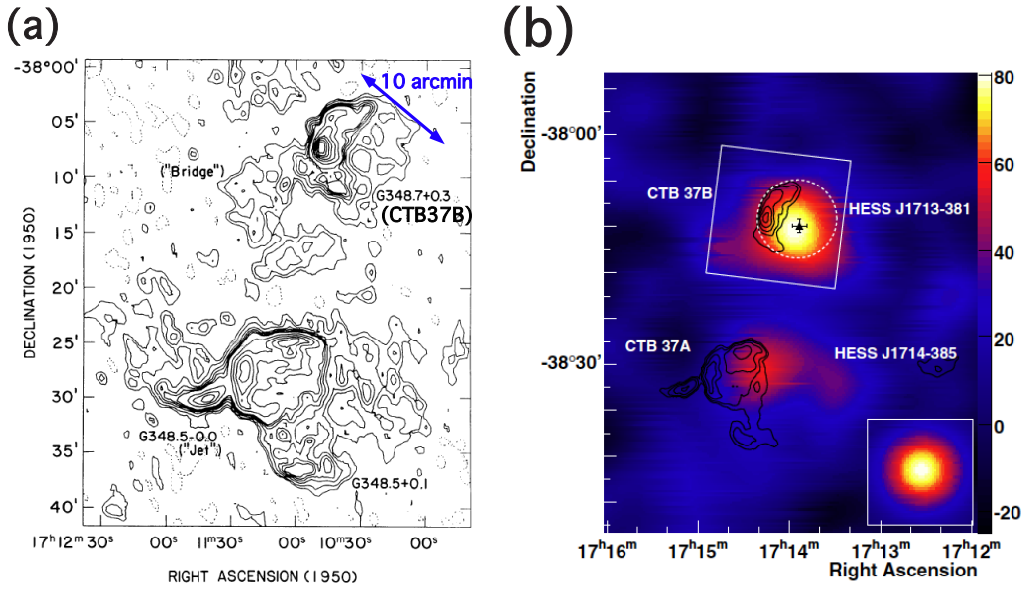

Figure 6.1: (a) 333 MHz radio image of the CTB37 complex adapted from Kassim et al. (1991). CTB37B corresponds to G348.7+0.3. (b) TeV γ-ray excess map of CTB37 complex taken from Aharonian et al. (2008b). The black contours represent radio emission from the Molonglo Galactic Plane Survey (Green et al., 1999). The simulated PSF is shown in the box in the bottom right corner. The color scale of the map is in units of counts per 0.0145 degree^2.

6.2 *Suzaku* and *Chandra* Observation and Data Reduction

In order to take an image and high-quality spectra of CTB37B, we carried out an observation of CTB37B with *Suzaku*. We also refer to the *Chandra* archival data to include the spatial structure and to compare them to our *Suzaku* data.

6.2.1 *Suzaku* Observation

CTB37B was observed with *Suzaku* during 2006 August 27–29. The nominal pointing position was (RA, Dec) = ($17^h13^m57^s$, $-38°12'15''$, J2000). We concentrate on the XIS data in this thesis, because the HXD has no imaging capability, and hence there remains a large systematic error in estimating the flux from CTB37B.

The XIS was operated in the normal full-frame clocking mode with neither burst nor window options and SCI-off. The editing mode was 3×3 in low and medium data rates and 5×5 in high and super-high data rates. In the analysis, we employed the data processed with the revision 1.2 pipeline software, and used the HEADAS software (version 6.2) and XSPEC (version 11.3.2) for the data reduction and spectral analysis, respectively. We applied the charge-transfer inefficiency (CTI) correction by ourselves

with the xispi software and CTI parameters of 2006–08–23. After screening the data, the effective exposure time was 80 ksec in total. Response matrix files (RMF) and ancillary response files (ARF) were made using xisrmfgen and xissimarfgen (Ishisaki et al., 2007) version 2007–09–22 under the assumption that the emissions are from a point source.

6.2.2 *Chandra* Observation

A *Chandra* observation was performed on the 2007 February 2 with the Advanced CCD Imaging Spectrometer (ACIS). Chips I0, I1, I2, I3 S2 and S3 were used. The data reduction and analysis were made using the *Chandra* Interactive Analysis of Observations (CIAO version 3.4, CALDB version 3.3.0). The total exposure time was 26 ksec after screening the data.

6.3 Image Analysis

6.3.1 *Suzaku* Images

Fig. 6.2 (a) and (b) show *Suzaku* XIS images in 0.3–3.0 keV and 3.0–10.0 keV. They were created by combining those from all the four XIS modules and smoothed with a Gaussian with σ =12 $''$, which is close to the XRT core size and effective in highlighting the diffuse emission. The source that is located at (l, b) $\simeq$ (348.°68, 0.°37) appears as the brightest source both in the soft and hard bands. Another source extending to the south of the brightest source, at (l, b) $\simeq$ (348.°63, 0.°32) seems to be a diffuse source, which manifests itself only in the band above 3 keV. In addition to these sources, a point source is detected at (l, b) $\simeq$ (348.°56, 0.°33) in the band below 3 keV. The sky position is consistent with that of the point source 1RXS J171354.4−381740 listed in the ROSAT Bright Star Catalogue (Voges et al., 1999). In order to investigate these sources separately, we defined the following photon-integration regions (see Fig. 6.2) for the spectral analysis. Region 1 is the green circle with a radius of 2.′6 centered at the intensity peak of the brightest source. Region 2 is the blue ellipse with a major and minor axis of 2.′5 and 1.′1, respectively, which is centered at the second diffuse source. Region 3 is the circle colored in magenta with a radius of 1.′3. The other three regions with the same colors, but with dashed lines, define those collecting the background events. We set these background regions by taking into account the telescope vignetting.

6.3.2 *Chandra* Images

Fig. 6.2(c) shows the *Chandra* image in the 0.3–10.0 keV band corrected for the telescope vignetting and smoothed with a Gaussian with $\sigma = 6\ ''$ to see the point sources clearly. In total, 18 sources are detected above 5σ confidence level (Aharonian et al., 2008b). Panels (d) and (e) are images in 0.3–3.0 keV and 3.0–10.0 keV, respectively, after removing the point sources. They were smoothed with a Gaussian with a $\sigma = 40\ ''$ to highlight the diffuse emission. The definition of the colored regions is the same as those drawn in the *Suzaku* images. The brightest source in region 1 is a point source, which is defined as source A, located at (l, b) = (348.°681, 0.°371). Although most of the flux from region 1 originates from the point source, it is revealed from figure 6.2(d) that region 1 is accompanied by diffuse emission. These two components are mixed in the *Suzaku* images. As expected

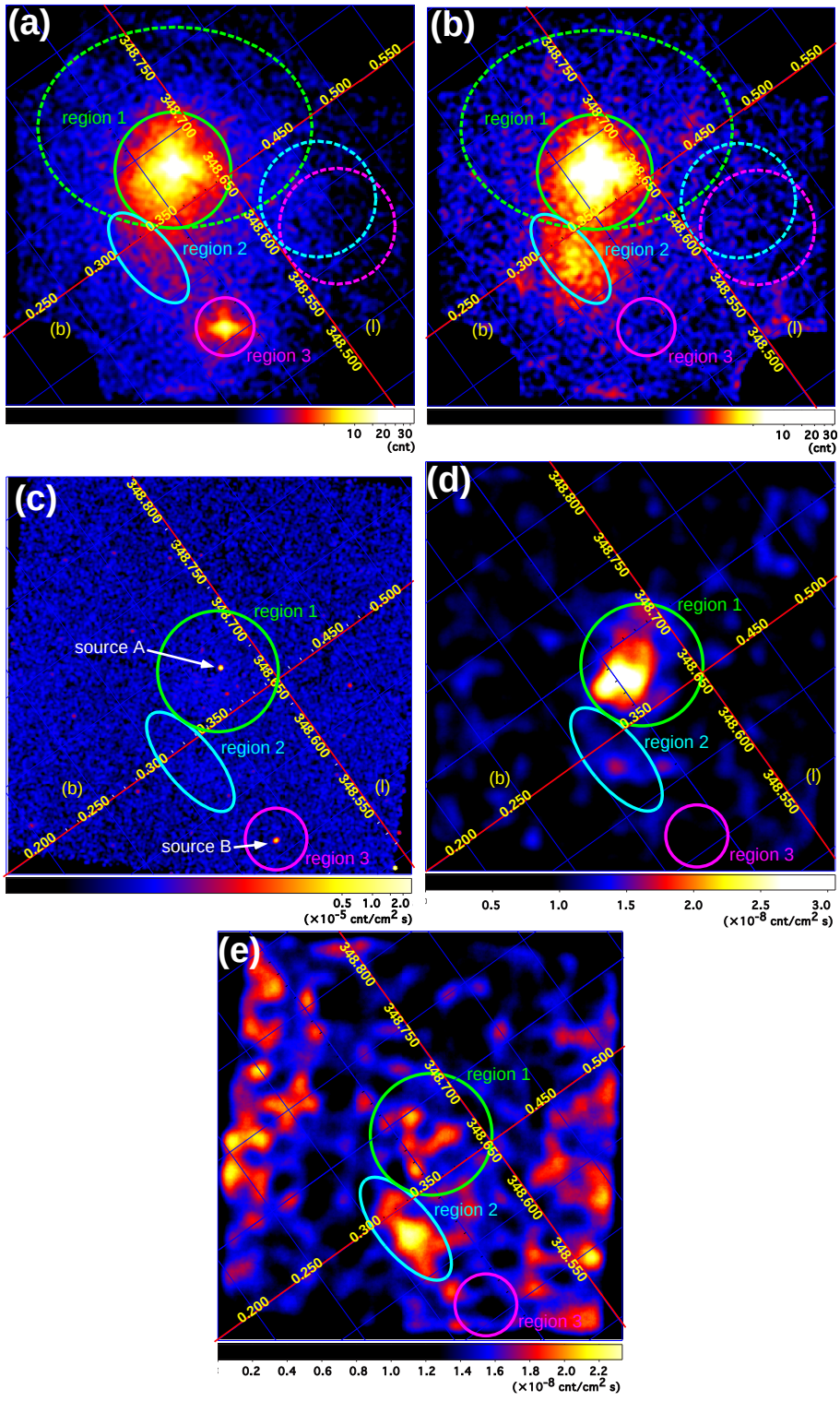

Figure 6.2: Images of CTB37B in the galactic coordinates. Panels (a) and (b) are *Suzaku* images in 0.3–3.0 keV and 3.0–10.0 keV, respectively, which are smoothed with a Gaussian with $\sigma = 12\ ''$. Panel (c) is the *Chandra* image in the 0.3–10.0 keV band being smoothed with a Gaussian with $\sigma = 6\ ''$. Panels (d) and (e) are the *Chandra* images in 0.3–3.0 keV and 3.0–10.0 keV, respectively. After removing point sources, we smoothed them with a Gaussian with a σ of 40 $''$. Solid circles in green, blue, and magenta are the integration region of source photons, which are named as region 1 through 3 in this order. Region 1 is a circle with a radius of $2'.6$, region 2 is an ellipse with a size of $1'.1 \times 2'.5$, and region 3 is a circle with a radius of $1'.3$. The dashed regions are corresponding background-integration regions.

Table 6.1: Count rates of sources and diffuse emission of *Chandra* data*.

Region	Energy band	Point source count rate [10^{-2} counts s^{-1}]	Diffuse emission count rate [10^{-2} counts s^{-1}]
region 1	0.3–3.0 keV	2.7 ±0.1	3.3 ±0.2
	3.0–10.0 keV	2.4 ±0.1	0.64 ±0.26
	total	5.0 ±0.1	3.9 ±0.4
region 2	0.3–3.0 keV	—	0.43 ±0.15
	3.0–10.0 keV	—	0.93 ±0.19
	total	—	1.4 ±0.2
region 3	0.3–3.0 keV	2.3 ±0.1	—
	3.0–10.0 keV	0.024 ±0.021	—
	total	2.3 ±0.1	—

* All errors are at 1σ confidence level.

from the *Suzaku* images in figure 6.2(a) and (b), region 2 is brighter than region 1 in the band above 3 keV. In region 3, there is the second bright source (defined as source B, which is 1RXS J171354.4−381740) located at (l, b) = (348.°561, 0.°332), and no diffuse emission is associated in 0.3–3.0 keV and 3.0–10.0 keV band. Table 6.1 summarizes the background-subtracted source count rates separately for point and diffuse sources in region 1, region 2 and region 3.

6.3.3 Correlation with Other Energy Band

Fig. 6.3 shows brightness contours of radio at 1.4 GHz in blue and of TeV γ-ray with H.E.S.S. in green, overlaid on the gray scale image of the *Suzaku* in the 0.3–10.0 keV band. Sources A and B resolved by *Chandra* are represented by the filled red boxes. The radio image is taken from the NRAO VLA Sky Survey (NVSS) database[1] (Condon et al., 1998). The X-ray emission well conforms with the shell in radio. Particularly, the diffuse X-ray source detected by *Suzaku* in region 2 is associated with the southern radio sub-peak. On the other hand, the peak of TeV γ-ray emission and source A seems to be separated from the radio shell. Note, however, that, due to limited spatial resolution of H.E.S.S, the apparent TeV source morphology is consistent with in a thin shell of radius $\sim 4.'5$, consistent with the radius of the radio shell (Aharonian et al., 2008b).

6.4 Spectral Analysis

In this section, we present results of spectral analysis of the two regions described above. We adopt the metal composition of Anders & Grevesse (1989) as the solar abundance as well as W28 analysis. Spectral fits are carried out with XSPEC. We always adopt an ancillary response file (ARF) for a point source, since the sizes of region 1 and 2 are so small that the resultant spectral parameters including the flux will differ only by ∼1% from the case if we take into account the spatial extent. The errors quoted are always at the 90% confidence level. Note that the point source detected in region 3 does not be

[1] http://www.cv.nrao.edu/nvss/

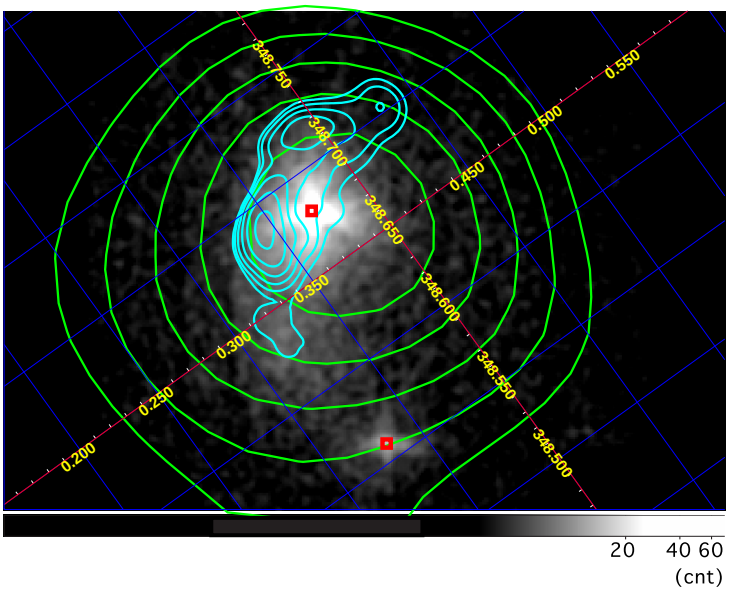

Figure 6.3: Gray scale *Suzaku* X-ray image with radio and TeV γ-ray contours (blue and green, respectively) overlaid. The blue radio contours are in logarithmic scale from 0.016 to 1.3 Jy/beam. The green TeV contours are in linear scale from 30 to 50 count/0.9 arcmin^2 stepped by 4. Red boxes are source A and B.

directly concerned with CTB37B, thus the analysis of region 3 is described in Appendix A.

6.4.1 Region 1

The *Chandra* spectrum of source A is shown in figure 6.4 (a). In extracting this spectrum, we took a circular integration region with a radius of 3″ centered at the source. We made no background subtraction. Since there is no apparent emission lines, we attempted to fit a power-law model undergoing photoelectric absorption ("phabs" model in XSPEC) to the spectrum. The best-fit model is overlaid in the upper panel of figure 6.4 (a) as the histogram. The best-fit parameters are summarized in table 6.2. The photon index, the hydrogen column density, and the intrinsic flux in the 2.0–10.0 keV band are $3.2^{+0.4}_{-0.3}$, 4.0 ($\pm$0.6) $\times 10^{22}$ cm^2, and 1.8 ($\pm$0.2) $\times 10^{-12}$ ergs cm^{-2}s^{-1}, respectively, which are consistent with those of Aharonian et al. (2008b). Figure 6.4 (b) is the background-subtracted *Chandra* region 1 diffuse emission spectrum, excluding the point sources in figure 6.2. Background spectrum was extracted from the dashed green circle shown in figure 6.2, which is the same as *Suzaku* region 1 background region. Kα emission lines from He-like Si (1.86 keV) and S (2.46 keV) were detected. This means that the spectrum includes a thermal emission component. We thus tried to fit the spectrum with a non-equilibrium collisional ionization plasma emission model ("vnei" model in XSPEC; Borkowski et al. (2001); Hamilton et al. (1983); Borkowski et al. (1994); Liedahl et al. (1995)) undergoing photoelectric absorption. In the fitting, we set abundances of Si and S free to vary. The other abundances are fixed at the solar abundance. The best-fit parameters are summarized in table 6.2, and the best-fit models are displayed in figure 6.4 (b). The temperature and the emission measure are $0.57^{+0.38}_{-0.17}$ keV and $1.0^{+4.0}_{-0.7} \times 10^{58}$ cm^{-3}, respectively. We only

Table 6.2: Best-fit parameters of the CTB37B region 1 spectra

Parameters		*Chandra* source A	*Chandra* diffuse	*Suzaku*
Power Law				
Photon Index		$3.2^{+0.4}_{-0.3}$	···	3.0 ±0.2
Intrinsic Flux [1]		1.8 ±0.2	···	$3.3^{+0.3}_{-0.4}$
VNEI				
Temperature [keV]		···	$0.57^{+0.38}_{-0.17}$	$0.89^{+0.21}_{-0.17}$
abundance [2]	Mg	···	1.0 (fix)	$0.61^{+0.31}_{-0.19}$
	Si	···	$1.6^{+1.3}_{-0.8}$	$0.40^{+0.21}_{-0.14}$
	S	···	$2.0^{+3.7}_{-1.4}$	1.0±0.6
$n_e t$ [3]		···	> 1.3	$3.5^{+13}_{-1.1}$
E.M. [4]		···	$1.0^{+4.0}_{-0.7}$	$2.1^{+1.6}_{-1.0}$
$N_{\rm H}$ [5]		4.0 ±0.6	$3.3^{+0.9}_{-0.6}$	$3.6^{+0.4}_{-0.2}$
χ^2/d.o.f (reduced χ^2)		14.6/18 (0.81)	17.8/14 (1.27)	176.1/166 (1.06)

[1] Flux in the 2.0–10.0 keV band in units of 10^{-12} ergs cm^{-2} s^{-1}.
[2] Abundance ratio relative to the solar value (Anders & Grevesse, 1989).
[3] Ionization time–scale in units of 10^{10} s cm^{-3} , where n_e and t are the electron density and age of the plasma.
[4] Emission measure $E.M. = \int n_e n_H dV \simeq n_e^2 V$ in units of 10^{58} cm^{-3}, where n_e and V are the electron density and the plasma volume. The distance to CTB37B is assumed to be 10.2 kpc (Caswell et al., 1975)
[5] Absorption column density in units of 10^{22} cm^{-2}.

obtained the lower limit of ionization parameter $n_e t > 1.3 \times 10^{10}\,\mathrm{cm^{-3}s}$.

Figure 6.4 (c) is the background-subtracted *Suzaku* spectrum of region 1. The black and red crosses represent the data points from the sum of the FI CCDs and those of the BI CCD, respectively. We obtained a higher quality spectrum with *Suzaku* than with *Chandra*. Although there is no sign of Fe Kα line in the 6–7 keV band, we have obviously detected Kα emission lines from He-like Mg (1.34 keV), Si (1.86 keV), and S (2.46 keV) as well as a Kβ emission line from He-like Si (2.18 keV). We thus tried to fit the *Suzaku* spectrum with a model composed of a power law representing source A and vnei model for diffuse thermal emission, undergoing photoelectric absorption. In the fitting, we set abundances of Mg, Si, and S free to vary. The abundances of the other elements are fixed at the solar abundances. The best-fit parameters are summarized in table 6.2, and the best-fit models are displayed in figure 6.4 (c). The fact that no iron Kα emission line was detected can be interpreted as the non-thermal component dominating the spectrum in the energy band above 3 keV. The reduced χ^2 of 1.06 implies that the fit is acceptable at the 90% confidence level. The temperature and the ionization parameter of the "vnei" component are obtained to be $kT = 0.89^{+0.22}_{-0.17}$ keV and $n_e t = 3.5^{+13}_{-1.1} \times 10^{10}$ cm^{-3}s, respectively. The results obtained from our *Suzaku* spectral analysis are consistent with that from *Chandra* diffuse emission spectrum within the error, except for the Si abundance. On the other hand, the photon index of the power-law model is $\Gamma = 3.0 \pm 0.2$ and the intrinsic flux is $3.3^{+0.3}_{-0.4} \times 10^{-12}$ ergs cm^{-2}s^{-1}. The photon index is consistent between *Suzaku* and *Chandra*, whereas the flux with *Suzaku* seems to be greater than that with *Chandra* by a factor of ∼1.8.

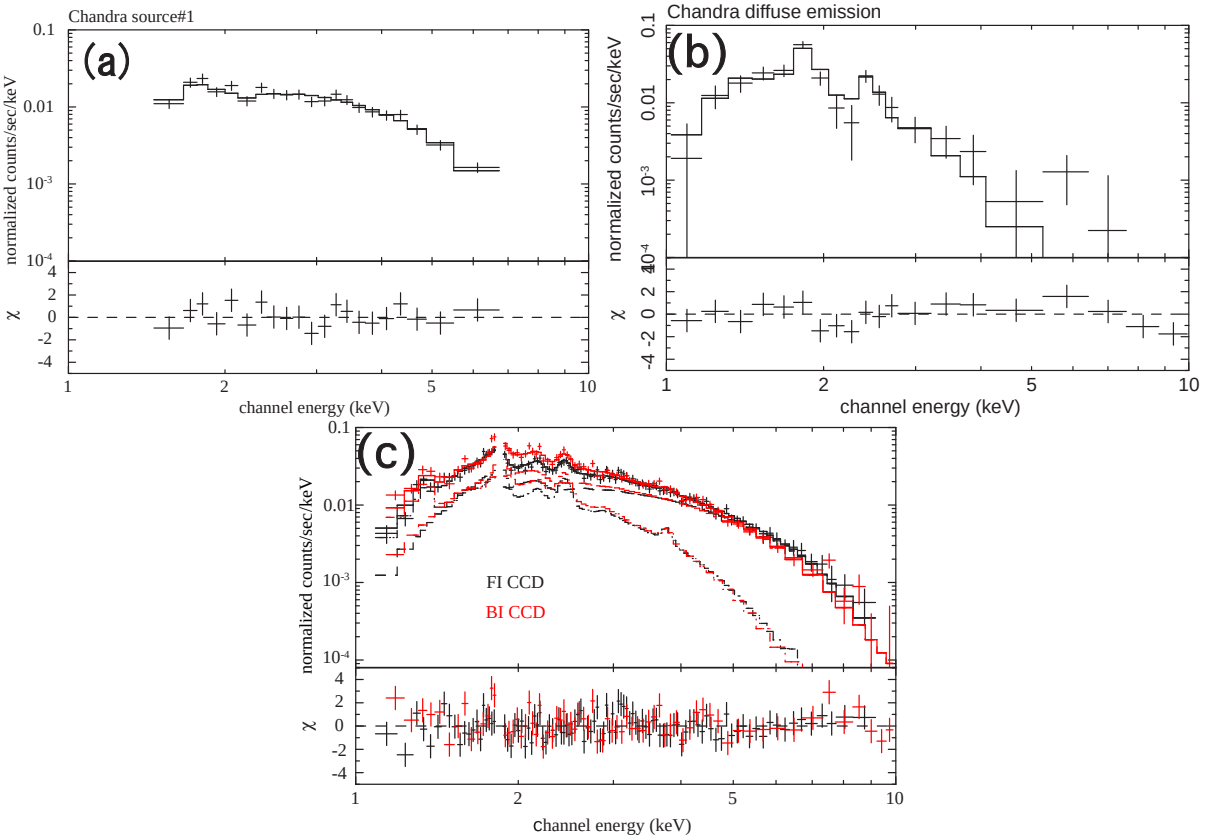

Figure 6.4: (a) *Chandra* spectrum integrated from a circular region with a radius of 3′ centered on source A. The best-fit model represented by a power law (histogram) is overlaid. (b) *Chandra* spectrum of region 1 except point sources. "vnei" model is overlaid. (c) *Suzaku* spectra of region 1 from the FI-CCDs (black) and the BI-CCD (red) with a model composed of a "vnei" and a power law model. The best-fit parameters are summarized in table 6.2.

6.4.2 Region 2

The *Suzaku* spectra of region 2 together with best-fit model and residual are shown in figure 6.5. The basic features, such as the He-like Si Kα emission line and no apparent

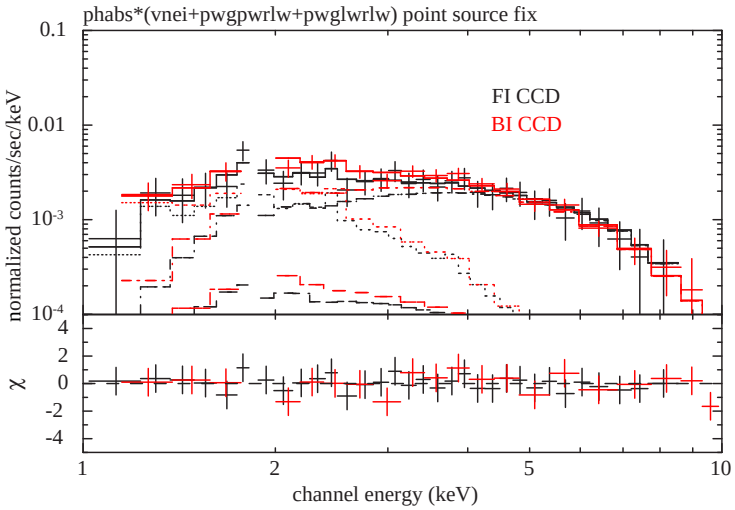

Figure 6.5: XIS spectra of region 2 with a model composed of a "vnei" and two power-law components, of which one represents contamination from source A. The normalization of "vnei" model and all parameters of the other power law are set free to vary.

sign of Fe emission line are similar to those in region 1. In addition to the thermal and non-thermal components, we need to take into account possible contamination from source A which is brightest in region 1. In fitting the region 2 spectra, we thus first tried a "vnei + power law (1) + power law (2)" model, where the power law (1) accounts for the source A, contamination, and the power law (2) represents a non-thermal component dominating the high energy band image in region 2 (figure 6.2). The vnei component, on the other hand, represents the contamination from region 1, and intrinsic thermal emission from region 2 if any. Note that the region 2 spectra are statistically poorer than those of region 1. Hence we have fixed the temperature, the abundances of Mg, Si, and S, the ionization parameter of the vnei component and the photon index of power law (1) at the best-fit values obtained in the region 1 fit, which are summarized in table 6.2. The flux between 2.0–10.0 keV of power law (1) is fixed at 3.3×10^{-14} ergs cm^{-2} s^{-1}, which is $\sim$1% of the source A flux, on the basis of the vignetting function (Serlemitsos et al., 2007). As a result, the free parameters are the hydrogen column density, the normalization of the vnei component, and all parameters of power law (2). The result of the fit is shown in figure 6.5, and the best-fit parameters are summarized in table 6.3. The $E.M.$ of the vnei component is $\sim$ 11 (4-20) % of the region 1 best-fit value. On the other hand, we simulated the contamination of the vnei component from region 1 using smoothed *Chandra* diffuse image shown in figure 6.6, and found the contamination is $\sim$ 7%. The thermal component apparent in region 2 spectra can therefore be entirely regarded as being contamination from region 1, and the upper limit of the $E.M.$ intrinsic to region 2 is 13% of that of region 1, or 2.7×10^{57} cm^{-3}. The photon index of power law (2) results in $\Gamma = 1.5$ (±0.4) with the reduced χ^2 of 0.36. It is remarkable that the X-ray photon index, $\Gamma = 1.5$, is consistent with the standard radio energy index of non-thermal SNRs $\alpha = 0.5$.

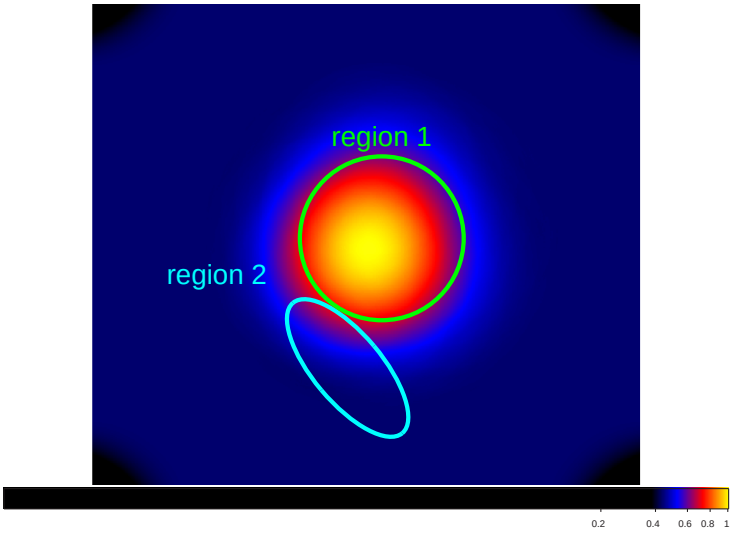

Figure 6.6: Smoothing image of *Chandra* region 1 diffuse emission with a smoothing Gaussian σ of 90 $''$.

We next replaced the power-law (2) component by an "srcut" model, which simulates a synchrotron spectrum from an exponentially cut off power-law distribution of electrons in a homogeneous magnetic field (Reynolds, 1998; Reynolds & Keohane, 1999). According to Kassim et al. (1991), the radio spectral index (α) is 0.3 with a flux at 1 GHz of 26 Jy. This small index, however, is probably due to contamination of thermal emission. A similar situation has been reported for 30 Dor C (Smith & Wang, 2004). We thus fixed α at 0.5, which is the typical value of the SNRs in the radio band, and set the flux at 1 GHz free to vary. As a result, the normalization of the srcut model was obtained to be 1.43 mJy at 1 GHz. This is much smaller than the radio flux 26 Jy at 1 GHz. Note, however, that this radio normalization is an integration of the entire radio image of CTB37B, part of which is, however, spilt out of regions 1 and 2. Moreover, the radio flux encompassed in region 2 is only $\approx$2% of that in region 1. We therefore estimate the radio flux within region 2 to be $\approx$1% of the total, or $\approx$ 300 mJy at 1 GHz. Even after this correction, simple extrapolation of the srcut model well fit to the X-ray spectra to the radio band is much smaller than the observed radio flux. We guess that the flux in the radio band is dominated by thermal emission. The resultant normalization (emission measure) of the vnei component does not change within the error. The reduced χ^2 value is nearly the same as that of the power-law fit. The lower limit of the roll-off energy was obtained to be 14.8 keV. We confirmed that the roll-off energy does not change drastically if we varied α in the range 0.3–0.7. Based on these results, it is possible to interpret that the spectrum of the non-thermal component extends from X-ray to radio with an energy index of 0.5 in the radio band.

6.4.3 Region 1 with additional non-thermal diffuse emission

As mentioned in §6.4.1, the *Suzaku* flux of the power-low component in region 1 is greater than that of *Chandra* source A by a factor of $\sim$1.8. Possible reasons for this difference are; (i) the variability of the source A flux, or (ii) the existence of another diffuse emission. We

Table 6.3: Best-fit parameters of the CTB37B region 2 spectrum

Parameters		VNEI + Powerlaw + Powerlaw	VNEI + Powerlaw + srcut
VNEI			
Temperature [keV]		0.89 (fix)	0.89 (fix)
abundance [1]	Mg	0.61 (fix)	0.61 (fix)
	Si	0.40 (fix)	0.40 (fix)
	S	1.0 (fix)	1.0 (fix)
$n_e t$ [2]		3.5 (fix)	3.5 (fix)
E.M. [3]		$0.23^{+0.18}_{-0.15}$	$0.23^{+0.14}_{-0.15}$
Power Law (1)			
Photon Index		3.0 (fix)	3.0 (fix)
Intrinsic Flux [4]		0.033 (fix)	0.033 (fix)
Power Law (2)			
Photon Index		1.5 ±0.4	···
Intrinsic Flux [5]		$0.78^{+0.07}_{-0.08}$	···
srcut			
alpha		···	0.5 (fix)
roll-off E [keV]		···	>14.8
Normalization [4]		···	1.4
Intrinsic Flux [5]		···	0.78
phabs $N_{\rm H}$ [6]		$3.5^{+0.5}_{-0.7}$	$3.5^{+0.5}_{-0.7}$
χ^2/d.o.f (reduced χ^2)		17.5/48 (0.36)	17.5/48 (0.36)

[1] Abundance ratio relative to the solar value (Anders & Grevesse, 1989).
[2] Ionization time–scale in units of 10^{10} s cm^{-3} , where $n_e t$ and t are the electron density and age of the plasma.
[3] Emission measure $E.M. = \int n_e n_H dV \simeq n_e^2 V$ in units of 10^{58} cm^{-3}, where n_e and V are the electron density and the plasma volume. The distance to CTB37B is assumed to be 10.2 kpc (Caswell et al., 1975)
[4] Radio flux at 1 GHz in units of 10^{-3} Jy.
[5] Flux in the 2.0–10.0 keV band in units of 10^{-12} ergs cm^{-2} s^{-1}.
[6] Absorption column in units of 10^{22} cm^{-2}.

need more observation to reveal the variability of source A. Here we check the possibility of existence of diffuse non-thermal emission in region 1.

We first tried to fit the *Chandra* region 1 diffuse emission spectrum with the "power law + vnei" model, where the power law represents the non-thermal diffuse emission which could be of the same origin as that detected in region 2. The photon index of the power law is fixed at the best fit value (Γ=1.5), demonstrated in §6.4.2. The spectrum with the best-fit model is shown in figure 6.7 (a), and the best-fit parameters are summarized in table 6.4. The reduced χ^2 is 1.01 for 13 degrees of freedom, which is improved from the fit with the simple "vnei" model shown in §6.4.1 with the reduced χ^2 of 1.27 for 14 degrees of freedom. However, the probability of F test by adding the power-law component to the model is 0.05. The existence of non-thermal diffuse emission is not highly significant. The intrinsic flux of the power law is obtained to be $0.27^{+0.16}_{-0.20} \times 10^{-12}$ ergs cm^{-2}s^{-1}.

Secondary, we fitted the region 1 *Suzaku* spectrum with "power law (1) + power law (2) + vnei" model, where power law (1) is the contribution from source A, and power law (2) plays a role as a non-thermal diffuse component which is found from region 2. The parameters of power law (1) and the photon index of power law (2) are fixed as the best fit values shown in §6.4.1 and §6.4.2. The result of the fit is shown in figure 6.7 (b), and the best-fit parameters are summarized in table 6.4. The reduced χ^2 of 1.08 implies that the fit is acceptable at the 90% confidence level, as well as the fitting the model without power law (2) with reduced χ^2 of 1.06, shown in §6.4.1. It is therefore possible that non-thermal diffuse X-ray source that is detected in region 2 also exists in region 1 solely from *Suzaku* data. The intrinsic flux of power law (2) is obtained to be $0.86^{+0.15}_{-0.17} \times 10^{-12}$ ergs cm^{-2}s^{-1}, which is much larger than that obtained from *Chandra* spectral analysis. Based on these results we consider the flux inconsistency of the power-law component as more plausibly being attributed to a flux variation of source A.

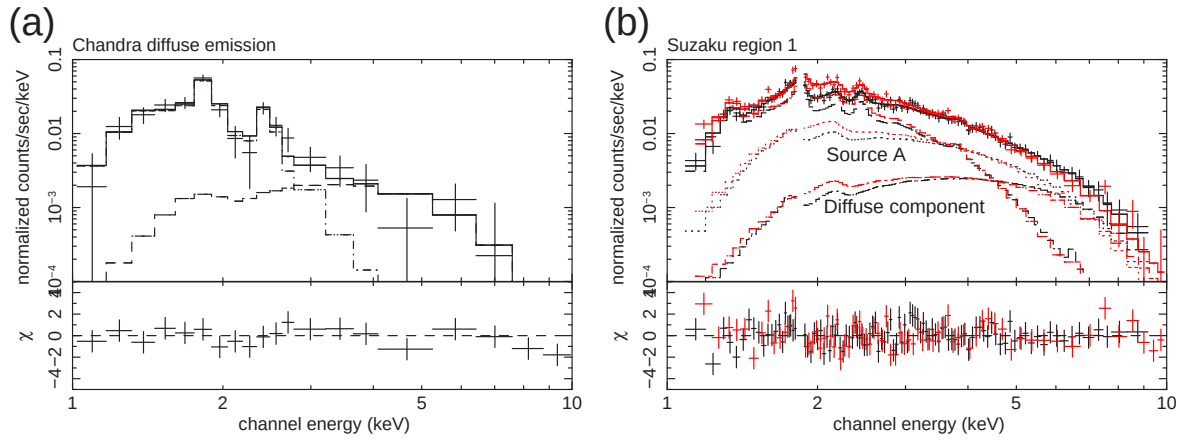

Figure 6.7: (a) *Chandra* spectrum of region 1 diffuse emission. "power law + vnei" model is overlaid. (b) *Suzaku* spectra of region 1 from the FI-CCDs (black) and the BI-CCD (red) with a model composed of a "2 power law + vnei" model. The best-fit parameters are summarized in table 6.4.

Table 6.4: Best-fit parameters of the CTB37B region 1 spectra with non-thermal diffuse component

Parameters		*Chandra*	*Suzaku*
Power Law 1 (source A)			
Photon Index		···	3.2 (fix)
Intrinsic Flux [1]		···	1.8 (fix)
Power Law 2 (diffuse emission)			
Photon Index		1.5 (fix)	1.5 (fix)
Intrinsic Flux [1]		$0.27^{+0.16}_{-0.20}$	$0.86^{+0.15}_{-0.17}$
VNEI			
Temperature	[keV]	$0.35^{+0.23}_{-0.10}$	$0.84^{+0.18}_{-0.06}$
abundance [2]	Mg	1.0 (fix)	$0.69^{+0.29}_{-0.24}$
	Si	$3.7^{+9.5}_{-2.3}$	$0.28^{+0.08}_{-0.07}$
	S	$8.6^{+35}_{-6.8}$	$0.35^{+0.39}_{-0.08}$
$n_e t$ [3]		>7.3	$10^{+6.3}_{-8.2}$
E.M. [4]		$2.6^{+6.4}_{-2.1}$	$3.7^{+0.9}_{-0.8}$
$N_{\rm H}$ [5]		$3.4^{+0.9}_{-0.8}$	$4.0^{+0.2}_{-0.5}$
χ^2/d.o.f (reduced χ^2)		13.1/13 (1.01)	180.2/167 (1.08)

[1] Flux in the 2.0–10.0 keV band in units of 10^{-12} ergs cm^{-2} s^{-1}.
[2] Abundance ratio relative to the solar value (Anders & Grevesse, 1989).
[3] Ionization time–scale in units of 10^{10} s cm^{-3} , where n_e and t are the electron density and age of the plasma.
[4] Emission measure $E.M. = \int n_e n_H dV \simeq n_e^2 V$ in units of 10^{58} cm^{-3}, where n_e and V are the electron density and the plasma volume. The distance to CTB37B is assumed to be 10.2 kpc (Caswell et al., 1975)
[5] Absorption column density in units of 10^{22} cm^{-2}.

6.5 Discussion

X-ray emission from CTB37B is composed of the diffuse thermal component (region 1) and the non-thermal component (region 2) as well as a point source (source A), as demonstrated in §6.3 and §6.4. Here we reveal the environments and conditions of CTB37B from thermal component, and discuss about the cosmic-ray acceleration using the fitting result of non-thermal component.

6.5.1 Thermal Component

We have calculated the electron number density and the age of the diffuse thermal plasma of region 1 and 2 on the basis of the best-fit parameters summarized in table 6.2 and 6.3. We assume that the plasma in region 1 distributes uniformly within a sphere with a radius of 1.′4, which is the Half-Width-of-Half-Maximum (HWHM) radius obtained from the *Chandra* image (Aharonian et al., 2008b). Assuming the distance to CTB37B of 10.2 kpc (Caswell et al., 1975), we obtain the real radius of region 1 to be $r_{\rm reg1} = 1.3 \times 10^{19}$ cm. Accordingly, the volume of the region 1 plasma is $V_{\rm reg1} = (4/3)\pi r_{\rm reg1}^3 = 9.2 \times 10^{57}$ cm^3. In the same way, from HWHM of an estimated image size of 1.′9 × 0.′9, the real length of semi-major and semi-minor axes result in $r_{\rm reg2,l} = 1.7 \times 10^{19}$ cm and $r_{\rm reg2,s} = 8.2 \times 10^{18}$ cm, respectively. Assuming that the line-of-sight extent of region 2 is $r_{\rm reg2,s}$, the volume of region 2 is calculated to be $V_{\rm reg2} = (4/3)\pi r_{\rm reg2,l} r_{\rm reg2,s}^2 = 4.8 \times 10^{57}$ cm^3 (the resultant electron density becomes smaller by a factor of $\sqrt{2}$ if we substitute $r_{\rm reg2,l}$ for $r_{\rm reg2,s}$). With $E.M. = \int n_e n_H dV = 2.1^{+1.6}_{-1.0} \times 10^{58}$ cm^{-3} (region 1) and 2.6×10^{57} cm^{-3} (region 2 upper limit, see § 6.4.2), the electron number density of region 1 and 2 are

$$n_{\rm e,\,reg1} \;=\; 1.7\;(1.2 - 2.2)\;\;[{\rm cm}^{-3}]$$

and

$$n_{\rm e,\,reg2} \;\leq\; 0.82\;\;[{\rm cm}^{-3}],$$

where we adopt the relation $n_{\rm e} \approx 1.24\ n_{\rm H}$ for fully ionized plasma. The parameter region in parenthesis is that allowed at the 90% confidence level. Assuming the strong shock, we obtain the pre-shock densities to be ∼0.43 cm^3 and ≤0.21 cm^3, respectively, which are significantly lower than the average density of the interstellar matter in the galactic plane. That means CTB37B exploded in a low density space. The density of region 1 together with the ionization parameter obtained from the fit of the region 1 spectra $n_{\rm e,\,reg1} t = 3.5^{+13}_{-1.1} \times 10^{10}$ [cm^{-3} s], enables us to estimate the age of the plasma observationally for the first time as

$$t_{\rm reg1} \;=\; 6.5\;(3.7 - 31) \times 10^2\;\;[{\rm yr}].$$

CTB37B is one of the best candidates of SN393 in Chinese historical record (Stephenson & Green, 2002). The plasma age calculated from the observed ionization parameter and emission measure supports this identification.

The number of electrons ($N_{\rm e} = n_{\rm e} V$) in region 1 and 2 are $N_{\rm e,\,reg1} = 1.6\,(1.1{-}2.0) \times 10^{58}$ and $N_{\rm e,\,reg2} \leq 3.9 \times 10^{57}$. As a result, the total mass included in the two regions are 15 (11–20)$M_\odot$ and ≤3.7$M_\odot$, respectively, and the thermal energy

$$E_{\rm reg1} = 6.4\;(4.1 - 8.6) \times 10^{49}\;\;[{\rm ergs}]$$
$$E_{\rm reg2} \leq 1.6 \times 10^{49}\;\;[{\rm ergs}].$$

under the assumption of energy equipartition between electrons and ions.

6.5.2 Non-thermal Component

The non-thermal diffuse component detected from region 2 has a remarkably flat X-ray spectrum with a photon index of 1.5. Since this photon index is equal to the typical radio photon index (energy index $\alpha = 0.5$), the non-thermal emission spectrum can be considered as extending from the radio band smoothly to the X-ray band, thereby the roll-off energy results in as high as $\geq$15 keV (table 6.3). This roll-off energy is higher than any other SNR that is accompanied by the non-thermal X-ray and TeV γ-ray emission, such as $\leq$9 keV for RX J1713.7–3946 (Takahashi et al., 2008), $\sim$0.23 keV for SN1006 (Bamba et al., 2008a), $\sim$0.87 keV for RCW 86 (Bamba et al., 2005). This indicates high electron acceleration efficiency in region 2. In addition, the density around region 2 is considered to be lower than in region 1, given that only the upper limit of the thermal emission is obtained (§ 6.6.1). The lower density may indicate higher shock velocity due to the smaller deceleration, which is consistent with the fact that the roll-off frequency is proportional to the square of the shock velocity (Aharonian & Atoyan, 1999).

It should be a matter of debate whether the TeV γ-ray emission and the non-thermal X-ray emission from region 2 are produced by the same population of electrons, since the images of these two bands shown in Fig. 6.3 are far from similar at first sight. The TeV γ-ray image is compatible with a shell with a radius of $\sim 4'$–$6'$ due to limited spatial resolution of H.E.S.S. (Aharonian et al., 2008b), which is compatible with the size of the radio shell. We thus assume that the TeV γ-ray emission is powered through 1-Zone Inverse Compton scattering (IC) of the cosmic microwave background due to the accelerated electrons.

The maximum electron energy ($E_{\rm max}$) can be evaluated by the shape of TeV γ-ray spectrum. Using the H.E.S.S. spectrum whose photon index is 2.3 (Aharonian et al., 2006) shown in Fig. 6.8 in blue, we determined $E_{\rm max}$ of 10 TeV. The red line in Fig. 6.8, on the other hand, is the X-ray power-law spectrum of region 2 with a photon index of 1.5. A series of the dashed plots are the model spectra calculated under the assumptions of $E_{\rm max}$ of 10 TeV, an index of the electron number density as a function of energy distribution of 2, and various magnetic field (0.1, 1.0 and 10.0 μG). It is clear from this figure that 1-zone IC model is unable to explain the synchrotron X-ray spectrum with any magnetic field strength. This suggests that TeV γ-ray emission is due to multi-zone IC scattering, or the decay of neutral pions generated by the high energy proton impacts, although the molecular cloud, which is the key of TeV γ-ray emission caused by π^0 decay, does not detected around CTB37B yet.

The flux of the power law in region 1 measured by *Suzaku* is apparently greater than that with *Chandra* source A by a factor of 1.8 (§6.4.1, table 6.2). Note that the point spread function of the *Suzaku* XRTs is not so sharp. Hence one may doubt that part of the power-law flux detected by *Suzaku* can be attributed to a putative diffuse non-thermal emission. We thus checked the existence of non-thermal diffuse emission in region 1 described in §6.4.3, on the assumption that non-thermal emission, detected in region 2 with a photon index of 1.5, is spatially connected to region 1. Although we could add a power-law model representing non-thermal diffuse X-rays to fit the *Suzaku* spectrum in region 1, the *Chandra* spectrum permits a much lower flux level. We thus conclude that the existence of the non-thermal diffuse emission in region 1 is marginal. Accordingly, the

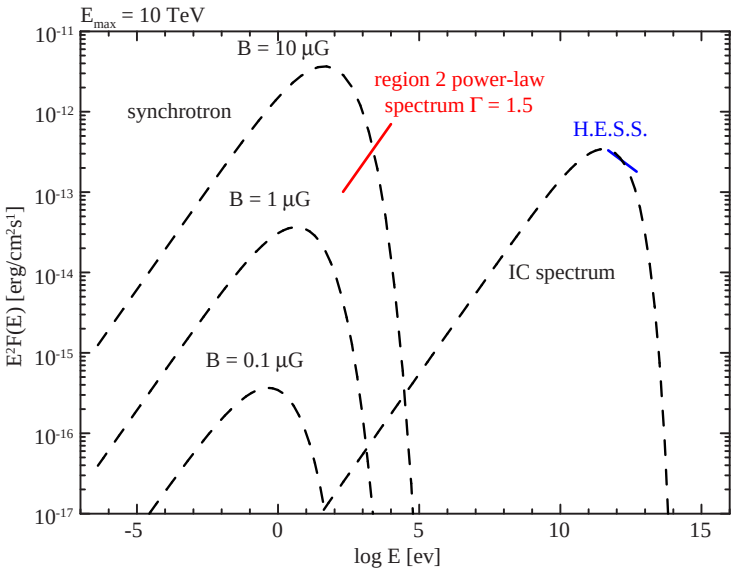

Figure 6.8: Spectrum energy distribution of region 2 from the X-ray and TeV γ-ray bands. The dashed plots on the left are the synchrotron radiation models with various magnetic field, and on the right is IC model spectrum. All the curves assume the maximum energy of electrons of 10 TeV. Blue line is the spectrum from H.E.S.S observation ($\Gamma = 2.3$; Aharonian et al. (2006)), and the red line is the *Suzaku* region 2 spectrum which is a power law with $\Gamma = 1.5$.

results derived here need not to be changed.

6.5.3 The Nature of Source A

The best-fit spectral parameters of *Chandra* source A and those of *Suzaku* region 1 (source A and the diffuse thermal emission) are summarized in table 6.2. The measured hydrogen column densities ($N_{\rm H} \simeq 4 \times 10^{22}$ cm^{-2}) are the same between *Chandra* and *Suzaku*. However, since the *Suzaku* spectra below $\sim$1 keV is dominated by the diffuse thermal component (Fig. 6.4), $N_{\rm H}$ obtained with *Suzaku* is determined mainly by the diffuse emission. This implies that source A is probably associated physically with the diffuse thermal emission in region 1, and is most likely a neutron star (or a black hole) born with the supernova explosion leading to CTB37B. Hence, CTB37B is probably Type II SNR. In fact, the large photon index of 3.2, the luminosity of 2.2×10^{34}ergs s^{-1}, and the spin period of 3.82 sec (Halpern & Gotthelf, 2009) are consistent with those of anomalous X-ray pulsar (AXP; Fahlman & Gregory (1981); Kuiper et al. (2006)). In addition, we showed the possibility of flux variance of source A, described in §6.4.3. This result supported that source A is an AXP, since long term variation is detected from some other AXPs (Gavriil & Kaspi, 2002; Kaspi et al., 2003). Further observation with high angular resolution will be able to reveal the flux variation of source A.

6.6 Summary of CTB37B

We have obtained with *Suzaku* the images and the high quality spectra of the supernova remnant CTB37B. The X-ray diffuse emission region coincides with that of radio and TeV γ-ray. The X-ray emission consists of thermal and non-thermal diffuse components as well as a point source resolved by *Chandra*.

The diffuse thermal emission can be best described by a non-equilibrium collisional ionization plasma model (NEI model) with a temperature, an ionization parameter ($n_{\rm e}t$ [cm^{-3}s]), and the abundances of 0.9±0.2 keV, 3.5 $^{+13}_{-1.1} \times 10^{10}$, and $\simeq 0.5 Z_{\odot}$ (Mg, Si), respectively. The image size and the observed emission measure provides the number density of the thermal electrons before the shock to be 0.2–0.4 cm^{-3}, which is significantly lower than that of the Galactic plane. This suggests that the supernova explosion associated with CTB37B took place at a low density space. From the ionization parameter and the number density of the thermal electron, the age of the plasma is found to be $\sim$650 $^{+2500}_{-300}$ yr. This is consistent with the tentative identification of CTB37B with SN393 within the error.

In contrast, the diffuse component occupying southern part of CTB37B (region 2) is non-thermal and represented by a power-law model or a srcut model. The photon index of 1.5 is significantly smaller than any other non-thermal SNR, but is consistent with that of a typical non-thermal SNR in the radio band. The srcut model fit with its normalization set free to vary therefore results in a high roll-off energy of >15 keV. Under the assumption that TeV γ-ray was emitted by 1-zone IC scattering, there are no solution for magnetic field strength that can reproduce the observed synchrotron spectrum in X-ray. This suggests that TeV γ-ray is produced by multi-zone IC scattering, or by the decay of neutral pions generated by the high energy proton impacts.

Owing to the high spatial resolution of *Chandra*, a point source is resolved from the brightest part of the *Suzaku* image of CTB37B (region 1). Its association to the diffuse thermal emission indicated by $N_{\rm H}$, thus CTB37B is probably Type II SNR. The photon index of $\sim$3, the X-ray luminosity of order 10^{34} erg s^{-1}, and the spin period of 3.82 sec all indicate that the point source is a new anomalous X-ray pulsar.

Chapter 7

Discussion

7.1 Summary of the Observational Results of W28 and CTB37B

In this thesis, we analyzed X-ray data of the two SNRs, W28 and CTB37B, from which TeV γ-rays were detected. The detection of TeV γ-ray is one of the direct evidence of cosmic-ray acceleration with the particle energy above $\sim$TeV. Our main results on cosmic-ray acceleration are;

- We discovered a power-law X-ray emission at high energy side of the XIS bandpass from both SNRs. This emission is most likely synchrotron X-ray from accelerated high energy electrons.

- Thermal X-ray was also detected. The electron density ($n_{\rm e}$) are derived from the spectral fitting, and we found that both SNRs are in low plasma density site.

We obtained the information of not only thermal but also non-thermal X-ray from middle-aged SNR with TeV γ-ray emission for the first time. In this chapter, we discuss about the time history of cosmic-ray acceleration in SNRs, and the environment of acceleration site with physical parameters of SNRs, using not only the two but also other Galactic SNRs with synchrotron X-ray emission.

7.2 Physical Parameters of Non-thermal X-ray SNRs

Table 7.1 shows a set of Galactic SNRs, which have synchrotron X-ray emission, with observational parameters. Note that our sample does not include Kepler, one of the young SNRs with synchrotron X-rays, since the thermal X-ray is too strong to derive precise parameters of synchrotron X-ray emission (see Reynolds et al. (2007)). Crab-like SNRs, which morphology in radio and X-ray are center-filled with an active rotation-powered pulsar (§3.3), are not included, either. The size (apparent diameter) and radio spectral index were obtained from Green's Catalog[1]. The physical radius is calculated by using distance to the object and apparent radius. The radio surface brightness at

[1]http://www.mrao.cam.ac.uk/surveys/snrs/

1 GHz continuum emission is calculated according to Case & Bhattacharya (1998), which is defined as

$$\Sigma_\nu \equiv 1.505 \times 10^{-19} \frac{S_\nu}{\theta^2} \ \ [\mathrm{W\,m^{-2}\,Hz^{-1}\,sr^{-1}}] \ , \tag{7.1}$$

where S_ν is 1 GHz flux in Janskys, and θ is an apparent diameter in arcminutes. S_ν can also be obtained from Green's Catalog[1]. The description of SB (Surface Brightness) ratio is given later (§7.3.2). The plasma electron density obtained from thermal X-ray, shown in table 7.1 is the value at upstream.

Comments on the Non-thermal X-ray Luminosity Estimate

The non-thermal X-ray luminosity listed in table 7.1 are the contributions from whole SNR, except W28, CTB37B, and G156.2+5.7. The evaluation method of these 3 SNRs X-ray luminosity are described below;

- W28
  We assume that the hard-tail component detected in W28 inner region is synchrotron X-ray emission by the accelerated electrons. The volume of the region covered with this study is about 5 % of the whole W28 on the assumption that W28 is a sphere with a radius of 13 pc. We thus assumed the upper limit X-ray luminosity of twentyfold value, which is included as a systematic error.

- CTB37B
  Synchrotron X-ray was detected from the south-part of CTB37B (region 2; see §6). However, synchrotron X-ray emission could be extended to the north-part of CTB37B shown in §6.4.3 (region 1). We included the X-ray luminosity of the non-thermal diffuse component evaluated with *Suzaku* to a systematic error.

- G156.2-5.7
  Yamauchi et al. (1999) reported the result with *ASCA* 2 pointing observation, which covered with the diameter of $40' \times$ 2 field of G156.2+5.7. We quoted the flux from this 2 pointing *ASCA* observation. They estimated the total X-ray flux in the $110'$ diameter SNR to be $\sim 2.4 \times 10^{-11}$ erg cm^{-2}s^{-1} by using the mean surface brightness. We used this value as the upper limit X-ray flux of G156.2+5.7.

Table 7.1: Physical Parameters of Non-thermal X-ray SNRs

Target name	Distance	Size [a]	Radius	Non-thermal Luminosity	
	[kpc]	[′]	[pc]	2–10 keV [10^{34} erg/s]	1–10 TeV [10^{34} erg/s]
W28	1.9 ±0.3	48	13 ±2	$0.069^{+1.3}_{-0.020}$	$0.062^{+0.021}_{-0.018}$
CTB37B	10.2 ±3.5	10 [b]	15 ±5	$0.97^{+3.1}_{-0.59}$	$1.6^{+1.2}_{-0.9}$
G1.9+0.3	8.5	1.5	1.9	$4.9^{+0.1}_{-0.2}$	—
Cas A	$3.4^{+0.3}_{-0.1}$	5	$2.5^{+0.2}_{-0.1}$	110^{+20}_{-6}	$0.33^{+0.06}_{-0.02}$
Tycho	$3.8^{+1.5}_{-1.1}$	8	$4.4^{+1.8}_{-1.3}$	12^{+12}_{-6}	<0.16
RX J1713 [c]	1.0	65 × 55	$8.7^{+0.8}_{-0.7}$	6.5	0.42
SN1006	2.2 ±0.1	30	9.5 ±0.3	$2.1^{+0.2}_{-0.1}$	0.054 ±0.004
G28.6-0.1	$7.0^{+1.5}_{-1.0}$	13 × 9	11 ±2	$0.88^{+0.42}_{-0.23}$	—
VELA Jr.	0.65 ±0.35	120	11 ±6	$0.42^{+0.58}_{-0.33}$	$0.22^{+0.30}_{-0.17}$
G32.45+0.1	17^{+7}_{-4}	6	15^{+6}_{-3}	$4.5^{+4.5}_{-1.9}$	—
G156.2+5.7	$1.0^{+0.3}_{-0.7}$	110	16^{+5}_{-11}	$0.060^{+0.43}_{-0.055}$	—
RCW86	2.8 ±0.4	42	17 ±2	$3.8^{+1.2}_{-1.0}$	$0.74^{+0.23}_{-0.20}$

[a] Apparent diameter obtained from radio emission.
[b] We used the size of partial radio shell shown in figure 6.1 (a).
[c] Abbreviation of RXJ1713.7-3946.

Table 7.1: Continue

Target	Radio band			Thermal X-ray	Reference
name	Surface brightness[d]	SB ratio	Spectral index[d]	Electron density[e]	
	Σ_ν[Wm^{-2}Hz^{-1}sr^{-1}]	$\Sigma_\nu/\Sigma_{1\mathrm{GHz}}$		$n_{0,\mathrm{th}}$ [cm^{-3}]	
W28	2.0×10^{-20}	2.4	∼0.35	0.12 ±0.02	This work,(1)(2)
CTB37B	3.2×10^{-20}	4.9	0.3	< 0.21	This work,(3)(4)
G1.9+0.3	4.0×10^{-20}	0.059	0.6	—	(5)
Cas A	1.6×10^{-17}	35	0.77	< 5.8	(6)(7)(8)(9)
Tycho	1.3×10^{-19}	1.1	0.65	< 0.4	(10)(11)(12)(13)
RX J1713	—	—	—	—	(14)(15)(16)
SN1006	3.2×10^{-21}	0.17	0.6	0.03	(17)(18)(19)(20)
G28.6-0.1	3.7×10^{-21}	0.28	—	—	(21)
VELA Jr.	5.2×10^{-22}	0.042	0.3?	? [f]	(22)
G32.45+0.1	1.0×10^{-21}	0.16	—	—	(23)
G156.2+5.7	6.2×10^{-23}	0.011	0.5	0.022	(24)(25)(26)
RCW86	4.2×10^{-21}	0.69	0.6	0.07 ±0.04	(27)(28)(29)(30)

[d] Parameters are obtained from Green's catalog (http://www.mrao.cam.ac.uk/surveys/snrs/)
[e] Upstream electron number density. We assume strong shock that a forward-shock plasma is 4 times compressed than the upstream medium.
[f] Estimation is difficult because of the contamination of thermal X-ray emission from Vela SNR.
(1) Velázquez et al. (2002), (2) Aharonian et al. (2008a), (3) Caswell et al. (1975), (4) Aharonian et al. (2008b), (5) Reynolds et al. (2008), (6) Reed et al. (1995), (7) Helder & Vink (2008), (8) Albert et al. (2007), (9) Lazendic et al. (2006), (10) Krause et al. (2008), (11) Tamagawa et al. (2009), (12) Aharonian et al. (2001), (13) Seward et al. (1983), (14) Fukui et al. (2003), (15) Slane et al. (1999), (16) Aharonian et al. (2004), (17) Winkler et al. (2003), (18) Bamba et al. (2008a), (19) Melitta et al. (2009), (20) Yamaguchi et al. (2008), (21) Bamba et al. (2001), (22) Aharonian et al. (2007b), (23) Yamaguchi et al. (2004), (24) Gerardy & Fesen (2007), (25) Yamauchi et al. (1999), (26) Katsuda et al. (2009), (27) Rosado et al. (1996), (28) Bamba et al. (2000), (29) Aharonian et al. (2009), (30) Vink et al. (2006)

7.3 Acceleration of Electrons

As mentioned in §2.3, accelerated high energy electrons interact with magnetic field, and emit synchrotron radiation from radio to X-ray band. Especially, synchrotron X-ray is emitted by electrons with $\geq$ TeV energy. Here we take note of the history of electron acceleration, and discuss on the environment of acceleration site.

7.3.1 Correlation with Radius and Synchrotron X-ray Luminosity

To probe the electron acceleration history, we have to investigate the time (or SNR age) dependence of synchrotron X-ray luminosity. However, the age of SNRs are unknown except historical SNRs; Cas A, Tycho, SN1006 and RCW86. Another method to determine an SNR age is using an ionization parameter $n_{\rm e}t$, where $n_{\rm e}$ is an electron number density and t is an ionization age of the plasma, which can be obtained from the spectral fitting of thermal X-ray emission with NEI model. We used this model for the analysis of W28 and CTB37B described in § 5 and § 6. The ionization age could be different from the real age such as SN1006 (Yamaguchi et al., 2008), and our sample includes SNRs with no thermal X-ray; G1.9+0.1, RX J1713, G28.6-0.1, and G32.45+0.1. We thus used a SNR radius instead of an age, because a radius can represents an SNR age based on the SNR evolution, introduced in §3.2. Figure 7.1 shows the correlation between radius and synchrotron X-ray luminosity. In this figure, red points show the results of this thesis. The marks mean the difference of SNR type; boxes are Type Ia SNRs, dots are core-collapse SNRs and triangle are unknown type SNRs, respectively. Young, small SNRs with R $\leq$5 pc have the synchrotron X-ray luminosity above $\sim 10^{34}$ erg/s. With the radius of $\geq$ 10 pc, the luminosities vary, and show the declining trend.

For comparison, the luminosity of radio continuum emission at 1 GHz versus the radius of the Galactic SNRs with known distances, is shown in figure 7.2. Blue points are SNRs of our sample. Crab-like SNRs are shown with cross points. Radio continuum emission from SNRs is almost non-thermal synchrotron emission from accelerated electrons with the energy of $\sim$ GeV. There is no correlation between radius and radio luminosity with no cut-off around 10 –20 pc in contrast to the synchrotron X-ray luminosity, and radio luminosities are within 10^{22} – 10^{25} erg s^{-1} Hz^{-1}. SNRs with $R>$ 20 pc are detected in radio band.

Factor of Synchrotron X-ray Luminosity Decrease

Here we consider the factor of X-ray luminosity decrease. As noted in § 2.2.3 and § 2.3.1, the power of synchrotron emission is

$$\begin{aligned} P &= 1.6 \times 10^{-3}\, {E_e}^2\, B^2 \quad [\mathrm{erg/s}] \\ &\propto {E_e}^2\, B^2, \end{aligned} \tag{7.2}$$

where $E_{\rm e}$ is an accelerated electron energy and B is a magnetic field (eq (2.26)). The typical synchrotron photon energy is described as

$$\begin{aligned} \varepsilon = h\nu_{\rm synch} &= 1.2 \left(\frac{E_{\rm e}}{100\,\mathrm{TeV}}\right)^2 \left(\frac{B}{1\mu\mathrm{G}}\right) \quad [\mathrm{keV}] \\ &\propto {E_e}^2\, B, \end{aligned} \tag{7.3}$$

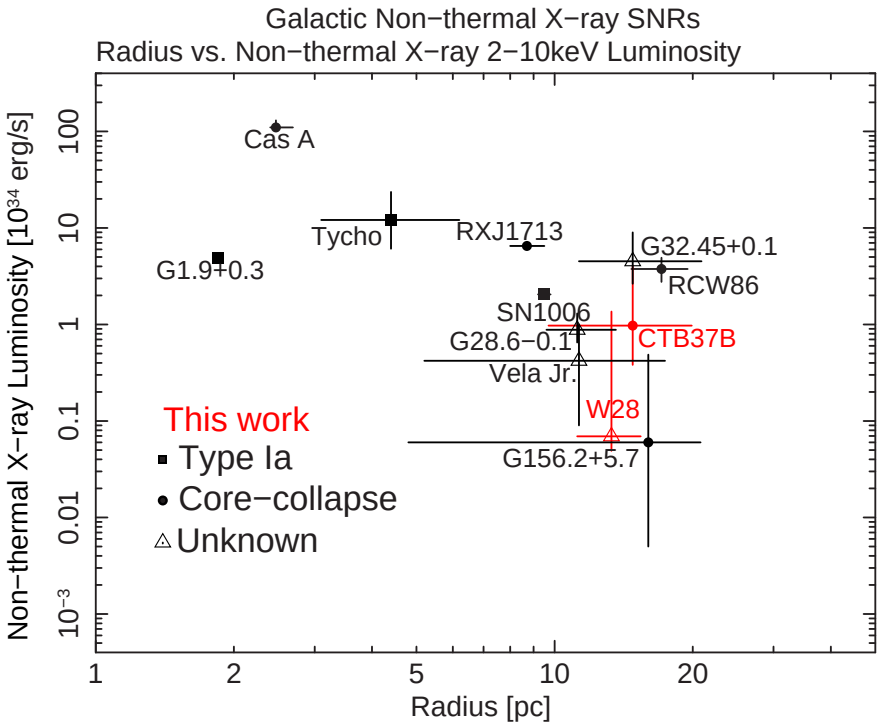

Figure 7.1: Correlation between radius and 2–10 keV synchrotron X-ray luminosity of Galactic SNRs

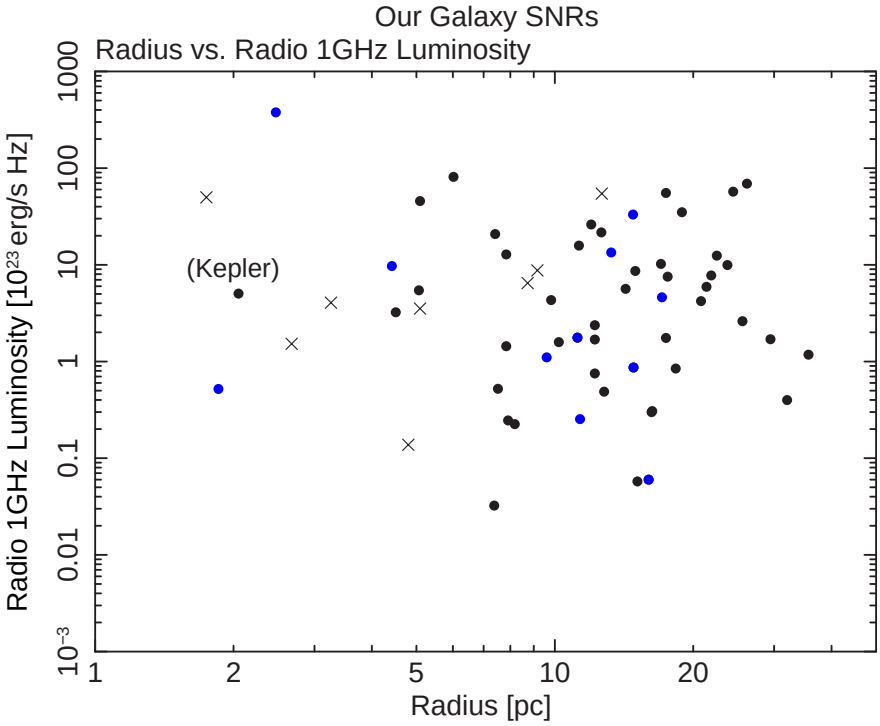

Figure 7.2: Radius vs. luminosity of radio continuum emission at 1 GHz of our Galaxy SNRs. Blue points show our sample of synchrotron X-ray detected SNRs. Crab-like SNRs are shown in cross points.

(eq. (2.31)). The synchrotron X-ray luminosity depends on $E_{\rm e}$ and B.

On the other hand, the power of synchrotron emission is proportional to the number of electron. Electrons lose their energy by synchrotron emission. The electron distribution can be described with the spectral form of a power-law with the index p and the exponential cut-off at $E_{\rm max,e}$. In the high energy cut-off region where the energy losses of electrons are dominated by the synchrotron cooling, the electron spectrum has a behavior, $N_{\rm e} \propto \exp\{-(E_{\rm e}/E_{\rm max,e})^2\}$, (Zirakashvili & Aharonian, 2007). Here we assume the electron distribution to be

$$N_{\rm e}(E_{\rm e})\,dE_{\rm e} = A\,{E_{\rm e}}^{-p} \exp\{-(E_{\rm e}/E_{\rm max,e})^2\}\,dE_{\rm e} \tag{7.4}$$

where A is a normalization and $E_{\rm max,e}$ is a maximum electron energy. When $E_{\rm max,e}$ becomes smaller of $\sim$ TeV, the number of electron, which emits synchrotron X-ray, decrease, and the power of synchrotron X-ray drops off.

We thus have to evaluate B and the electron distribution with $E_{\rm max,e}$ to explain the observational synchrotron X-ray luminosity trend.

Model to explain the Time History of Synchrotron X-ray Emission

We construct a simple model to calculate the synchrotron X-ray luminosity to explain the observational results.

Let us start to calculate the shock velocity $v_{\rm s}$ to determine B and $E_{\rm max,e}$, because SNR radius, B, and $E_{\rm max,e}$ can be represented by using $v_{\rm s}$, shown as follows.

We assume $v_{\rm s}$ as a function of the age of SNR $t_{\rm age}$ as (Yamazaki et al. (2006) and § 3.2)

$$v_{\rm s}(t_{\rm age}) = \begin{cases} v_i & (0 < t_{\rm age} < t_1;\ \text{Free expansion phase}), \\ v_i \left(\frac{t_{\rm age}}{t_1}\right)^{-3/5} & (t_1 < t_{\rm age} < t_2;\ \text{Sedov phase}), \\ v_i \left(\frac{t_2}{t_1}\right)^{-3/5} \left(\frac{t_{\rm age}}{t_2}\right)^{-2/3} & (t_2 < t_{\rm age};\ \text{Radiative phase}) \end{cases} \tag{7.5}$$

where

$$t_1 = (3E/2\pi\, m_{\rm H}\, n_0\, {v_i}^5)^{1/3} = 2.1 \times 10^2 (E_{51}/n_0)^{1/3} {v_{i,9}}^{-5/3} \ \ {\rm yr}, \tag{7.6}$$

$$t_2 = 4 \times 10^4 {E_{51}}^{4/17}\, {n_0}^{-9/17} \ \ {\rm yr}, \tag{7.7}$$

(Blondin et al., 1998), and $v_i = v_{i,9} \times 10^9\ {\rm cm\,s^{-1}}$ and $E = E_{51} \times 10^{51}$ erg are the initial velocity and the initial energy of ejecta, n_0 is an electron number density in upstream thermal plasma, respectively. The shock radius $R_{\rm s} = \int v_{\rm s} {\rm d}t$ can be calculated. We adopt $E_{51} = v_{i,9} = 1$ as a fiducial case.

As the ejecta expands, the shock wave is developed, and the kinetic energy of the shock is distributed among the magnetic field energy, the thermal energy, the cosmic-ray energy, and so on. The fractional energies of them seem constant and time-independent. (e.q. Bamba et al. (2005)). We thus assumed that the magnetic field energy density of the downstream $U_B (= B_{\rm d}^2/2\pi)$ is proportional to the thermal energy density of downstream ($U_{\rm th}$),

$$\begin{aligned} \frac{B_{\rm d}^2}{8\pi} &= \varepsilon_B\, U_{\rm th} \\ &= \frac{3}{2}\,\varepsilon_B\, r\, n_0\, kT_{\rm d}\ , \end{aligned} \tag{7.8}$$

where ε_B is a coefficient, r is a compression ratio and $kT_{\rm d}$ is a temperature of downstream. $kT_{\rm d}$ is obtained by using the Rankine-Hugoniot equation (eq. (2.4), (2.5), (2.6)),

$$kT_{\rm d} = \frac{r-1}{r^2}\, m_{\rm p}\, v_{\rm s}^2 \ . \tag{7.9}$$

Then the magnetic field is derived from

$$B_{\rm d} = \left(12\pi\, m_{\rm p}\, \frac{r-1}{r}\, \varepsilon_B\, n_0 \right)^{1/2} v_{\rm s} \ . \tag{7.10}$$

We assumed that $\varepsilon_B = 0.005$, which can roughly represent the predicted magnetic field from observations such as 250 –500 μG with Cas A and Tycho ($R \sim 3$ pc), and ∼100 μG with SN1006 and RX J1713.7–3946 ($R \sim 10$ pc) (Parizot et al., 2006). Note that the magnetic field is saturated to the interstellar magnetic field times the compression ratio ($B_{\rm ISM} \times r$), ultimately. Here we assume $B_{\rm ISM}$ of 10 μG.

As discussed in §2.2.3, the key parameter to determine the maximum electron energy $E_{\rm max}$ is whether the SNR age is shorter than the synchrotron loss time scale or not. The synchrotron time scale is given by $t_{\rm loss,e} = 1.25 \times 10^4 (E_{\rm max}/10\,{\rm TeV})^{-1} (B_{\rm d}/10\mu{\rm G})^{-2}$ yr (see eq. (2.27)). When $t_{\rm age} < t_{\rm loss,e}$ (age-limited case), the maximum energy is given as

$$E_{\rm max,age} = \frac{4.8 \times 10^2}{\xi} \left(\frac{v_{\rm s}}{10^8\ {\rm cm\,s^{-1}}} \right)^2 \left(\frac{B_{\rm d}}{10\ \mu{\rm G}} \right) \left(\frac{t_{\rm age}}{10^5\ {\rm yr}} \right) \quad [{\rm TeV}] \ , \tag{7.11}$$

where ξ is gyrofactor, and in the loss-limited case ($t_{\rm age} > t_{\rm loss,e}$), $E_{\rm max,e}$ is

$$E_{\rm max,loss} = \frac{24}{\xi^{1/2}} \left(\frac{v_{\rm s}}{10^8\ {\rm cm\,s^{-1}}} \right) \left(\frac{B_{\rm d}}{10\ \mu{\rm G}} \right)^{-1/2} \quad [{\rm TeV}] \ , \tag{7.12}$$

(see eq. (2.25) and (2.28)). Here we presume the strong shock (r=4), and the gyrofactor ξ of 3.0.

The model-predicted correlation with a radius and other physical parameters are shown in figure 7.3. We calculated in 3 cases with the upstream plasma density n_0=0.01 cm^{-3}, 0.1 cm^{-3}, and 1.0 cm^{-3}, respectively. Panel (a) shows the shock velocity dependence to the radius. The free expansion phase ($v_{\rm s}$=constant) continues at the radius R of ∼10 pc with n_0=0.01 cm^{-3}, $R \sim 5$ pc with n_0=0.1 cm^{-3}, and $R \sim 2$ pc with n_0=1 cm^{-3}, respectively. The evolution of the magnetic field $B_{\rm d}$ varies according to n_0, although $B_{\rm d}$ fixes down at the interstellar magnetic field with R ∼20 pc as shown in panel (b). Electrons are accelerated to be 20 – 70 TeV when SNRs are small and young, in free expansion phase. The radius becomes larger, $E_{\rm max,e}$ decrease with a factor of 1.5 – 3. With low plasma electron density n_0, the accelerated electron gets energy higher. This means that $E_{\rm max,e}$ is determined with loss-limited case already at the radius of 1 pc, because $E_{\rm max,age} \propto B_{\rm d}$, $E_{\rm max,loss} \propto B_{\rm d}^{-1/2}$ (see eq. (7.11) and (7.12)), and $B_{\rm d}$ has adverse sense of $E_{\rm max,e}$ for different n_0 shown in figure 7.3 (b) and (c).

The synchrotron X-ray luminosity can be calculated with B, $E_{\rm max,e}$ and electron distribution of $N_{\rm e}(E)dE = AE^{-p}{\rm e}^{-(E/E_{\rm max,e})^2}dE$ shown in eq. (7.4). The number index p is assumed to be 2.0, which is the predicted value of the DSA theory (§2.2.2) with compression ratio $r = 4$. To fit the calculated luminosity to the observed data, we used the normalization of electron number distribution A of 4.0×10^{47} [GeV^{-1}] at 1 GeV. For

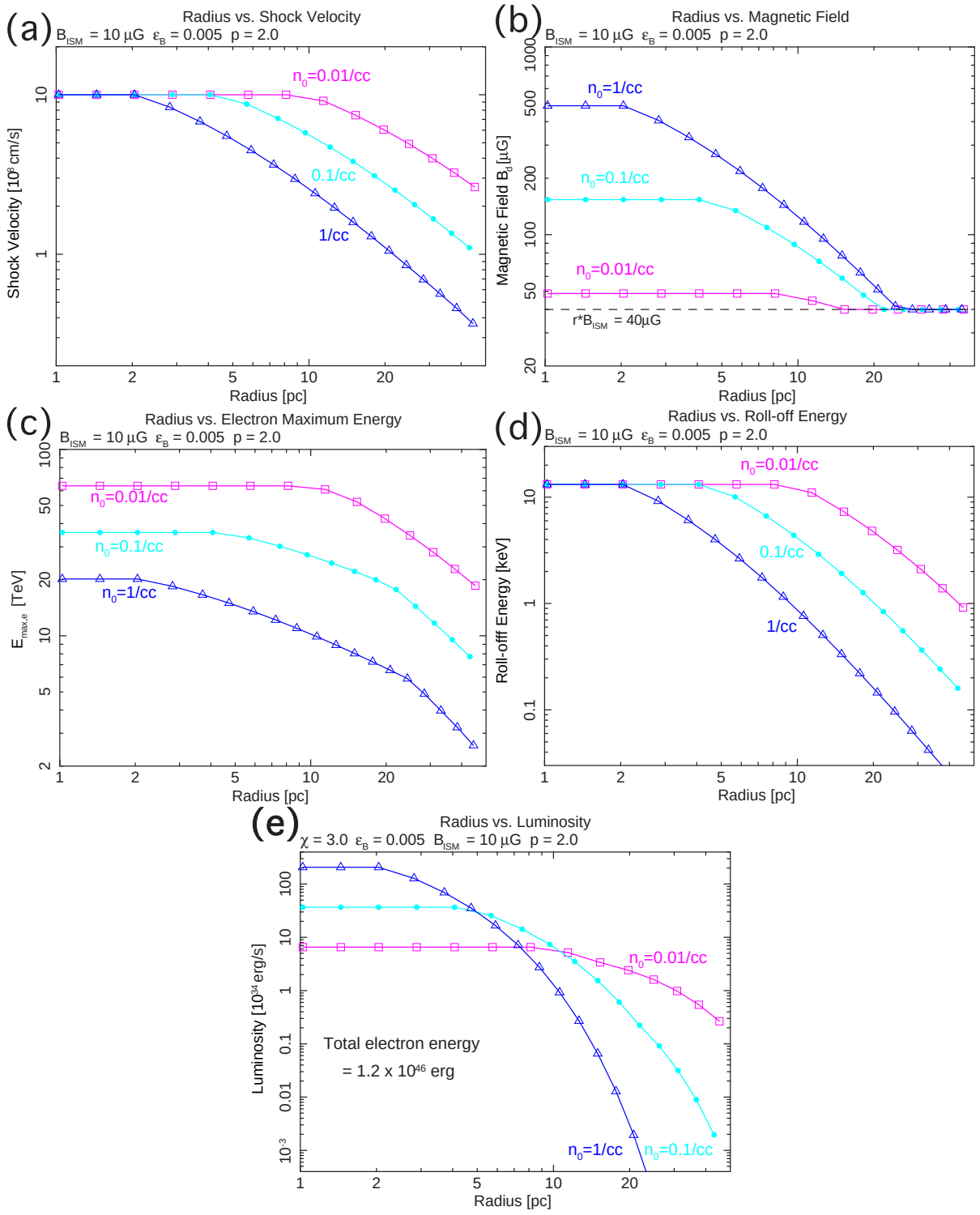

Figure 7.3: Correlation between radius vs. shock velocity (a), radius vs. magnetic field (b), radius vs. maximum electron energy (c), radius vs. roll-off energy of synchrotron emission (d), and radius vs. synchrotron X-ray luminosity (e).

simplicity, we fixed the value A for the calculations with n_0=0.01 cm^{-3}, 0.1 cm^{-3}, and 1.0 cm^{-3}. Using this electron distribution, the total accelerated electron energy above 511 keV is obtained to be 9.2×10^{45} erg –1.2×10^{46} erg with $E_{\rm max,e}$ of 1 TeV – 100 TeV, which is smaller than the expansion energy of 10^{51} erg, thus this model is consistent with the energy budget on electron acceleration. The roll-off frequency of synchrotron emission is given by Reynolds & Keohane (1999) to be

$$\nu_{\rm roll} \sim 1.6 \times 10^{16} \left(\frac{B_{\rm b}}{10\,\mu{\rm G}} \right) \left(\frac{E_{\rm max,e}}{10\,{\rm TeV}} \right)^2 \quad [{\rm Hz}]. \tag{7.13}$$

Particularly in the loss-limited case, using eq. (7.12), $\nu_{\rm roll}$ can be written as

$$\nu_{\rm roll} \sim 9.6 \times 10^{16}\, \xi^{-1} \left(\frac{v_{\rm s}}{10^8\ {\rm cm\,s^{-1}}} \right)^2 \quad [{\rm Hz}]. \tag{7.14}$$

The observed 2–10 keV luminosity strongly depends on this roll-off frequency (or energy). Figure 7.3 (d) shows the radius dependence of roll-off energy. Synchrotron X-ray luminosity decrease comes from that the roll-off energy passes over the X-ray band around the radius of 10 – 20 pc. Finally, we obtained the calculated 2–10 keV synchrotron X-ray luminosity shown in figure 7.3 (e).

Compare to the Observation and the Model

We compared with observation results and calculated luminosity for $n_0 = 0.01,\ 0.1,\ 1.0\,{\rm cm^{-3}}$, respectively. Results are shown in figure 7.4. Calculated results well represent the observational data points with the electron number density n_0 of 0.01 – 1.0 cm^{-3}. The dispersion of the data could be caused by the difference of an environment of explosion, mainly an plasma electron number density n_0. This means acceleration of electrons strongly depends on n_0. The time scale of synchrotron X-ray emission is longer with small n_0.

As a result, we described the development of synchrotron X-ray luminosity to the radius by considering the evolution of SNRs. Thus, the history of accelerated electrons can be explained with this simple model. Electrons which have ∼TeV energy, which radiate synchrotron emission in the X-ray band, are accelerated in SNRs with a radius of ≤20 pc. An electron density of exploded site plasma exercises an effect of electron acceleration.

Parameter dependence for the Model

We have calculated the synchrotron X-ray luminosity with $\varepsilon_B = 0.005$, $\xi = 3.0$, $B_{\rm ISM} = 10\ \mu$G, $p = 2.0$. ε_B is an unknown parameter, which is the proportionality coefficient between magnetic field energy density and thermal energy density (see eq. (7.8)). ξ is a gyrofactor ($\sim(B/\delta B)^2$), which represents a measure of the magnetic field turbulence. The smallest possible value of ξ=1 (so-called Bohm limit) corresponds to the case of the most efficient acceleration. From observations, the range of ξ could be 1 – 10 (Takahara, 2002). The magnetic field of interstellar matter $B_{\rm ISM}$ is believed to be ∼10 μG, and number index of accelerated electron distribution p is obtained based on the acceleration theory (eq. (2.18)) with the assumption of strong shock (r=4), to be p=2.0. Here we considered dependence of our model on the unknown parameter ε_B and ξ.

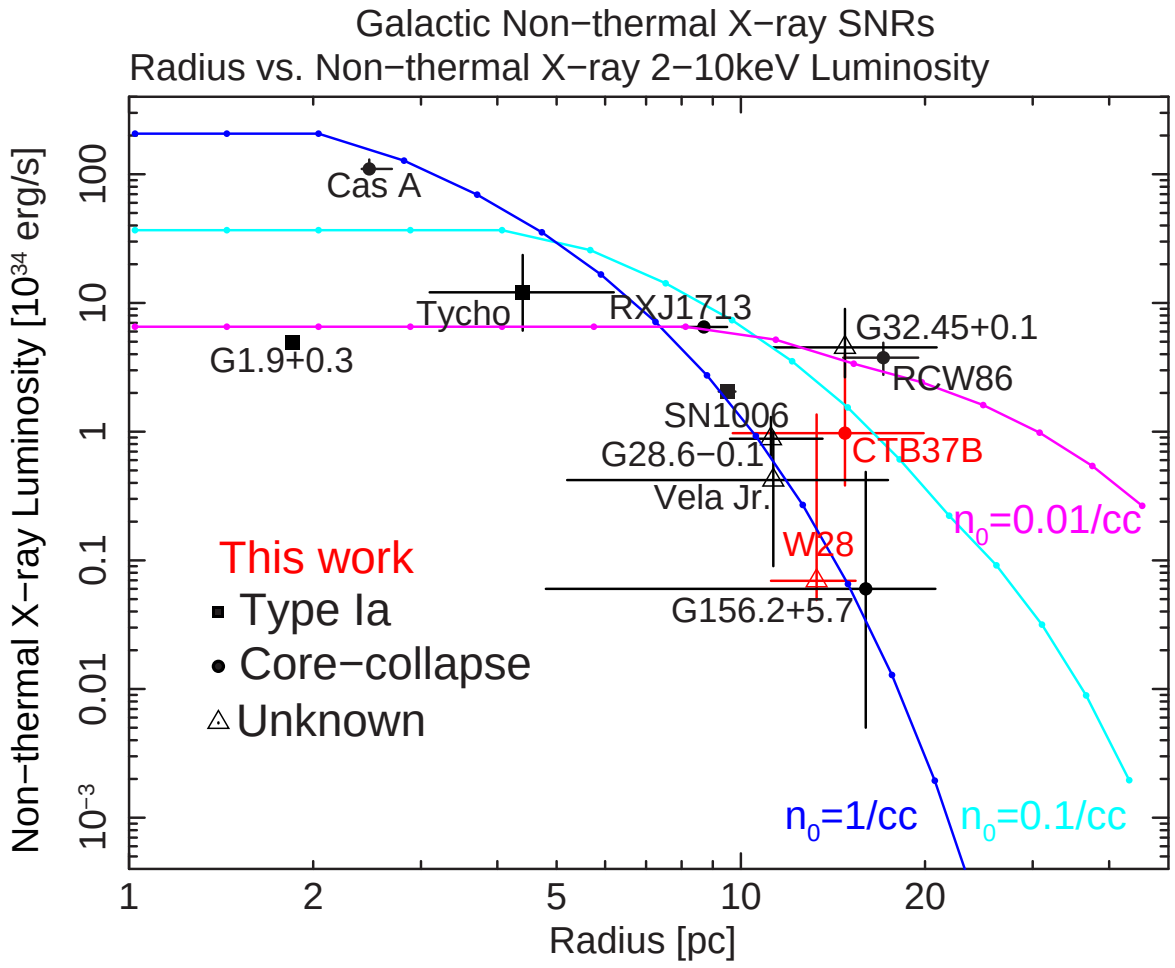

Figure 7.4: Calculation results of synchrotron X-ray luminosity with the observational data

We checked in the case of $\varepsilon_B = 0.0005$ and 0.05, which are 1/10 and 10 times the value by the previous case of $\varepsilon_B = 0.005$. Magnetic field, maximum electron energy, synchrotron roll-off energy, and luminosity are shown in figure 7.5. The magnetic field strongly depends on ε_B. The maximum electron energy is few dozens of TeV for both cases. The trends of luminosity are same, and the model well represented the observational data. Total accelerated electron energy above 511 keV is 10^{45}–10^{46} erg for both cases, which is consistent with energy budget on electron acceleration.

We next checked the dependence of gyrofactor ξ with 1.0 and 10.0. The parameters of which depend on ξ are maximum electron energy, roll-off energy of synchrotron X-ray emission, and luminosity, respectively (eq. (7.11) to (7.14)). Results are shown in figure 7.6. The maximum electron energy is up to $\sim$100 TeV with ξ=1.0. The calculated luminosity represent the observation results, although the shape of luminosity curve is slightly different. The luminosity decreases earlier with ξ=10.0 than that with ξ=1.0. Total electron energy is $\sim 10^{46}$ erg, which is consistent as well as with other parameter calculation.

As a result, the observed result can be explained with this model with ε_B of 0.0005 – 0.05 and ξ of 1.0 –10.0. Energy budget of electrons is also consistent with any cases. We found one important result that the electron acceleration history strongly depends on the plasma density n_0. With any parameters, synchrotron X-ray from accelerated electrons have longer time scale with low n_0.

Note that we did not take into account some effects in our model, which may be important, such as time dependence or density dependence of the electron injection rate on the acceleration site, since we have no clear indication from observations. We did not consider possible difference associated with SN type (see §3.2), and so on. Nevertheless, our model as a whole reproduces the apparent correlation between the luminosity and the radius, and is important as a first step to understand the history of accelerated electrons. Reflection of those effects to the model is a scope of future work.

7.3.2 Relation Between Radio Surface Brightness and Non-thermal X-ray

The relation between a physical radius and a surface brightness of radio continuum emission is reported by Case & Bhattacharya (1998), so-called "$\Sigma - D$ relation". Figure 7.7 shows $\Sigma - D$ relation for galactic SNRs. The radio surface brightness is defined as eq. (7.1), and values of our sample are listed in table 7.1 (Σ_ν). The data of SNRs with known distance are plotted. Here we included the data of Kepler's SNR, and Crab-like SNRs shown with cross points. The best-fit relation model is derived in Case & Bhattacharya (1998) as

$$\Sigma_{1\mathrm{GHz}} = 2.07^{+3.10}_{-1.24} \times 10^{-17} \times D^{(-2.38\pm0.26)} \ \ [\mathrm{W\,m^{-2}\,Hz^{-1}\,sr^{-1}}], \tag{7.15}$$

which is described in figure 7.7 with solid line. The surface brightness ratio (SB ratio) shown in table 7.1 are the value of Σ_ν / $\Sigma_{1\mathrm{GHz}}$.

SNRs from which synchrotron X-ray were detected are marked with black boxes and red stars (this work). Most SNRs with synchrotron X-ray, except Cas A, CTB37B, and W28, have low brightness than the best-fit value, which is equal to low SB ratio. Case & Bhattacharya (1998) treated Cas A as a special case (Cas A is the only young, oxygen-rich, with jetlike feature SNR). The surface brightnesses of CTB37B, W28, and Vela

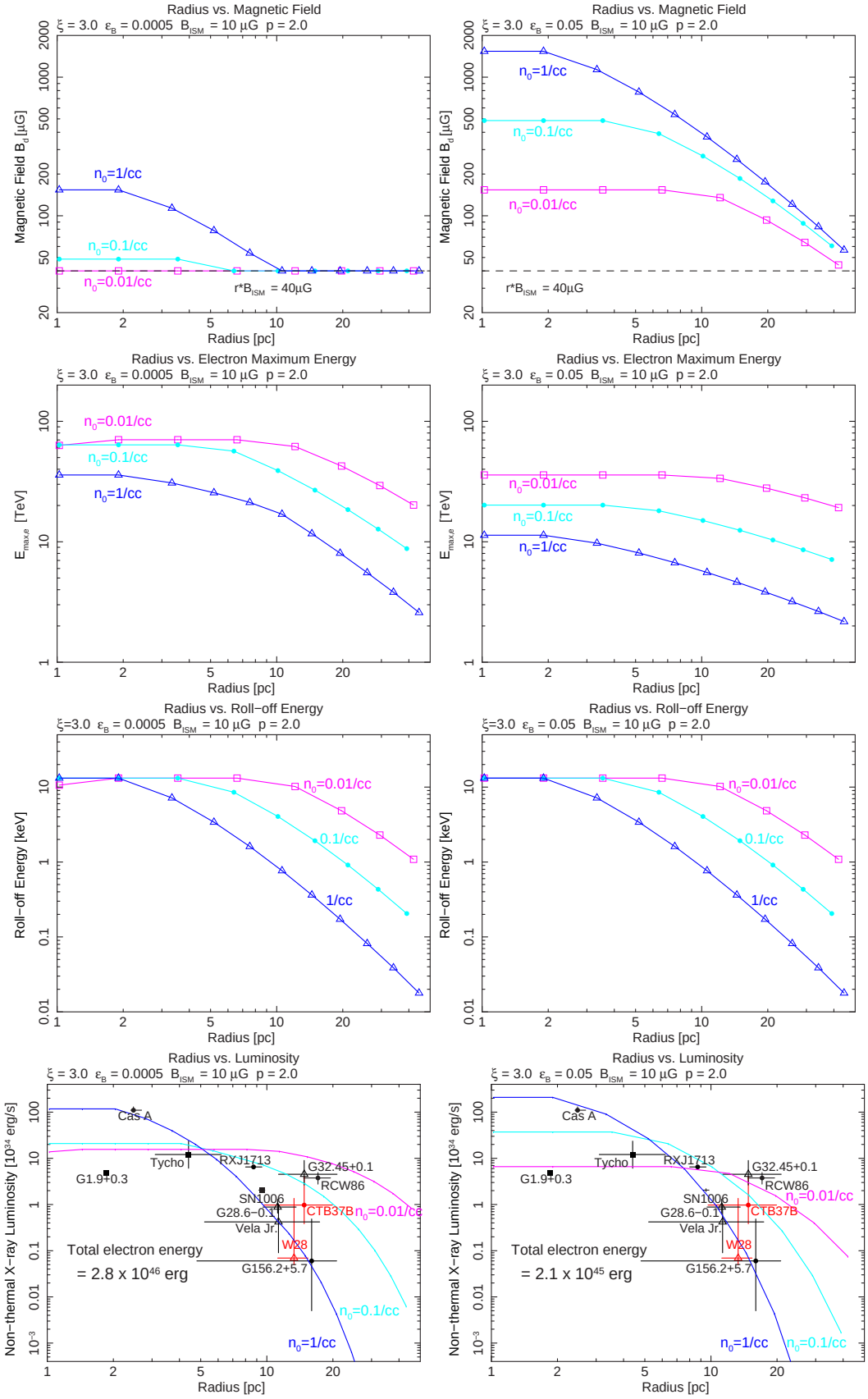

Figure 7.5: ε_B dependence for the model with $\varepsilon_B = 0.0005$ and 0.05. Other parameters are fixed at ξ=3.0, $B_{\rm ISM}$=10μG, p=2.0. Left Panels show in the case of ε_B=0.0005, and right panels are with ε_B=0.05. Magnetic field, maximum electron energy, synchrotron roll-off energy, and observed and calculated luminosity are shown from top through bottom panels.

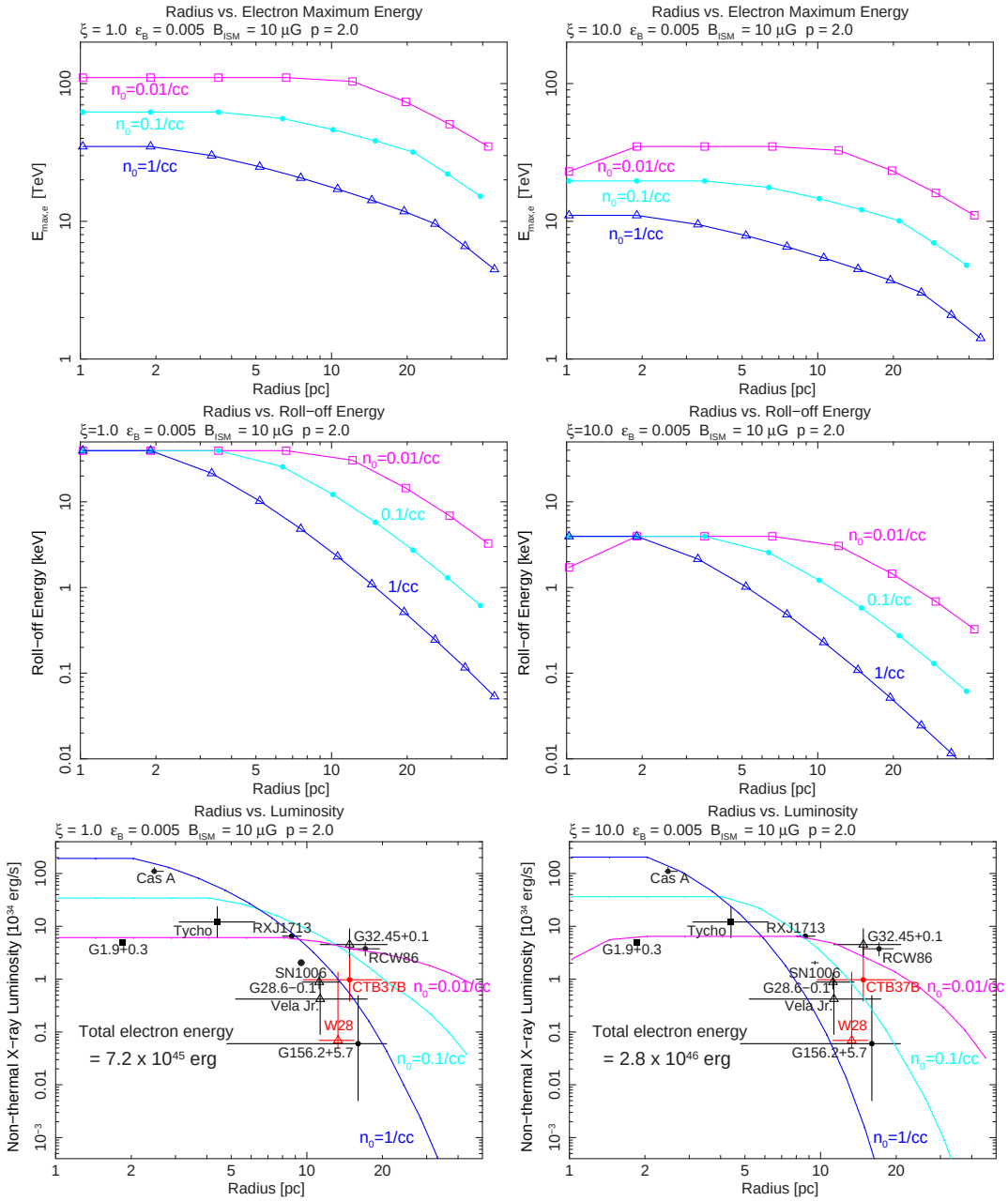

Figure 7.6: ξ dependence for the model with $\xi = 1.0$ and 10.0. Other parameters are fixed at ε_B=3.0, $B_{\rm ISM}$=10μG, p=2.0. Left Panels show in the case of ξ=1.0, and right panels are with ξ=10.0. Maximum electron energy, synchrotron roll-off energy, and observed and calculated luminosity are shown from top through bottom panels.

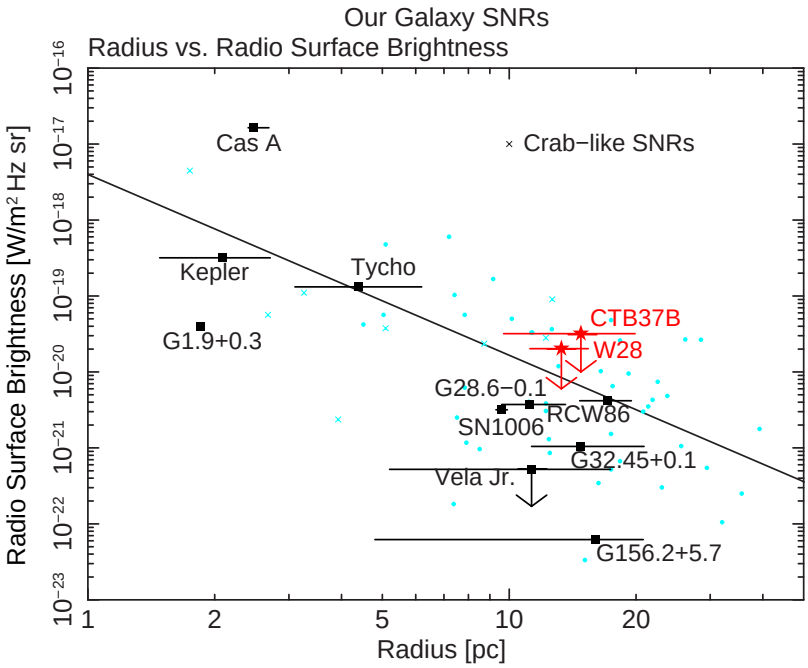

Figure 7.7: Radius vs. surface brightness relation for galactic SNRs. Points show data of SNRs of which distances are known from Green's Catalog. Best-fit model is shown in solid line. SNRs with synchrotron X-ray are shown in black boxes and red stars (this work).

Jr. are upper limits because of small radio spectral index of ∼0.3 shown in table 7.1, which is probably due to contamination of radio thermal emission. These suggest that synchrotron X-ray is likely to be observed from low surface brightness SNRs in the radio band. Radio continuum emission from SNR is almost non-thermal synchrotron emission. Thus, low radio surface brightness means weak synchrotron radiation, that is equal to weak magnetic field, or small accelerated electron number which have the energy of ∼GeV. A weak magnetic field is linked in low thermal plasma electron density n_0 shown in figure 7.3 (b). This is consistent with the trend of relation that synchrotron X-rays from accelerated electrons have longer time scale in lower n_0.

7.3.3 Upstream Electron Number Density Derived from Thermal X-ray emission

Downstream electron number density can be obtained by using thermal X-ray emission. With the strong shock, downstream plasma is 4 times more compressed than the upstream medium. We thus derived upstream electron density $n_{0,\mathrm{th}}$ by diving the downstream electron density by 4. Figure 7.8 shows the correlation of radius and the upstream electron number density. The red points are our work shown in § 5 and § 6. Note that the thermal emission of Cas A and Tycho, which are young SNRs, are mainly from ejecta which are thermalized by the reverse shock. Since the ISM density is believed thinner than that of ejecta, we plot the density of Cas A and Tycho as the upper limit shown triangles in figure 7.8. The electron densities are summarized in table 7.1. Thermal X-ray emission is not detected from RXJ1713, G1.9+0.3, G32.45+0.1, and G28.6-0.1, which means low

density or low temperature of the plasma (see eq. (3.19). The emission power of thermal bremsstrahlung is proportional to $n_e^2 \times T^{1/2}$.) The estimation of the thermal X-ray from Vela Jr. is difficult because of the contamination of thermal X-ray emission from Vela SNR, which is located along the line of sight.

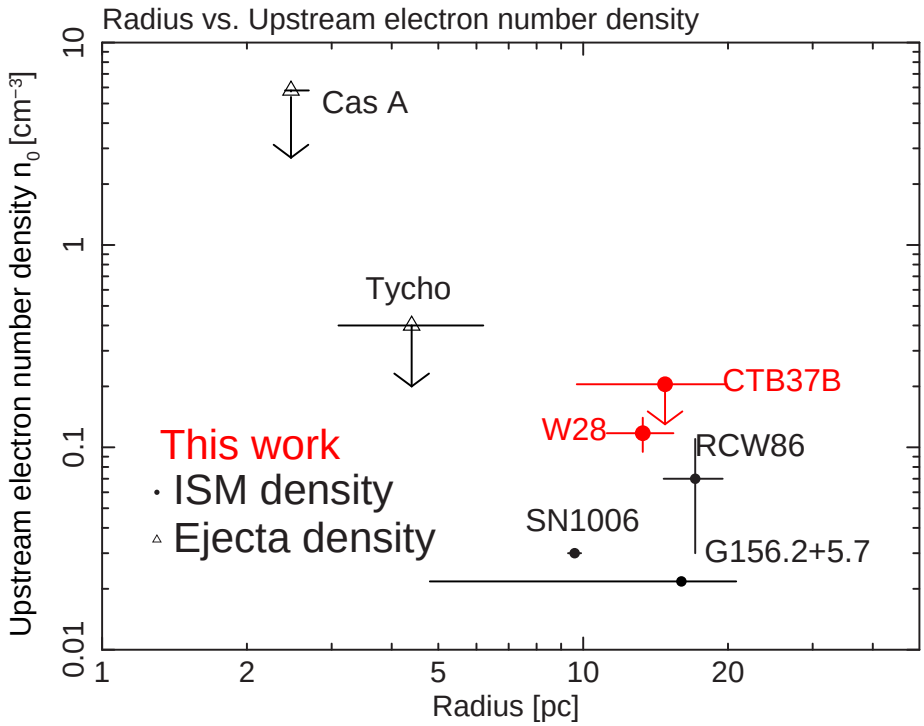

Figure 7.8: Radius vs. upstream electron number density.

Except Cas A, the electron number density is lower than the typical value of galactic plane of $n_0 \sim 1$ cm^{-3}. Especially for $R \geq$10 pc SNRs, the density is less than 0.2 cm^{-3}. This observational fact also supports that the time scale of synchrotron X-ray is longer with smaller n_0.

Note that the plasma density derived from the thermal X-ray ($n_{0,\rm th}$) is slightly different from the density (n_0) which was used to calculate the radius-luminosity curve shown in figure 7.4 (for example, in the case of RCW86, measured plasma density $n_{0,\rm th}$ is 0.07 cm^{-3} in figure 7.8, whereas RCW86 locates on the curve with n_0=0.01 cm^{-3} in figure 7.4.). The density n_0 is the mean density of ISM where the shock wave passed over, while $n_{0,\rm th}$ is the density of the site from which thermal X-rays were detected. Hence, n_0 might be different from $n_{0.\rm th}$.

7.4 Acceleration of Protons

An acceleration of electrons can be explained with a very simple model, by considering the evolution of SNR. Here, we develop an acceleration history model for protons with same assumption of electron acceleration.

We calculated the maximum proton energy $E_{\rm max,p}$ as follows. The cooling timescale of protons due to π^0-decay emission is $t_{\rm loss,p,\pi^0} \sim 6\times10^7\,(n_{\rm H}/1\,{\rm cm}^{-3})^{-1}$ yr as shown in §2.3.4,

and that due to synchrotron radiation is $t_{\rm loss,p,synch} \sim 4 \times 10^8 \, (E_{\rm p}/10^{15}\,{\rm eV})^{-1} \, (B/10\,\mu{\rm G})^{-2}$ yr. These are much longer than the SNR age, thus $E_{\rm max,p}$ in the system is determined by the age-limited case shown in eq.(7.11). Note that we do not consider $E_{\rm max,p}$ with escape-limited case (e.g. Ohira et al. (2009)). Figure 7.9 shows the $E_{\rm max,p}$ dependence with SNR age and radius. In free expansion phase, $E_{\rm max,p}$ increases in proportion to the age, and protons are accelerated up to 10^{15} eV quickly in $\sim$100 yr. When the shock velocity decreases and the evolution of SNR goes into sedov phase, $E_{\rm max,p}$ becomes smaller with $\propto {t_{\rm age}}^{-(4/5)}$ in the system. Protons basically does not loose energy and it should be kept at $\sim 10^{15}$ eV.

In contrast to the case of electron acceleration, the maximum value of $E_{\rm max,p}$ becomes higher for higher plasma density n_0, and the maximum $E_{\rm max,p}$ change only by a factor of $\sim$2 between $n_0 = 0.01$ cm^{-3} to 1 cm^{-3}. Since the protons are free from synchrotron cooling, its maximum energy $E_{\rm max,p}$ is proportional to $B\,t_1$, where t_1 is the life time of the free expansion phase. With the equation of $B \propto {n_0}^{1/2}$ (eq 7.10) and $t_1 \propto {n_0}^{-1/3}$ (eq 7.7), $E_{\rm max,p}$ is proportional to ${n_0}^{1/6}$. As a result, protons are accelerated up to $\sim 10^{15}$ eV with little density dependence. This result is important in explaining the break at $\sim 10^{15.5}$ eV in the observed cosmic-ray spectrum, since if the maximum $E_{\rm max,p}$ had large density dependence, the cosmic-ray spectral break would not have been observed.

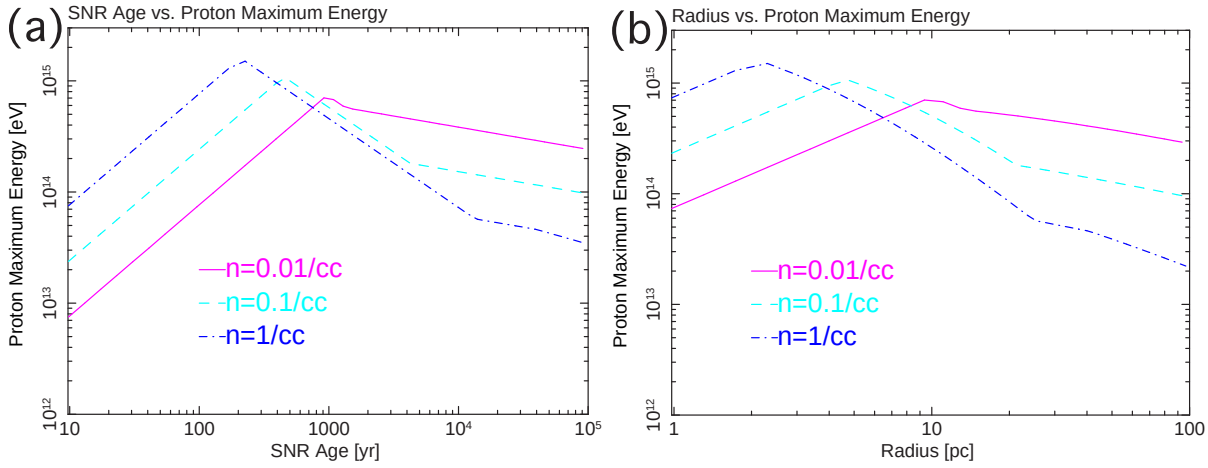

Figure 7.9: Correlation between (a) SNR age and maximum proton energy, (b) radius and maximum proton energy.

We also calculated $E_{\rm max}$ with ε_B=0.05 and ξ=1.0, which means strong magnetic field and high maximum energy in age-limited case (eq. (7.10) and (7.11)), and obtained to be $\sim 10^{15.7}$ eV with n_0=1.0. This is consistent with knee energy of $10^{15.5}$eV.

In addition, We plotted the correlation between radius and 1–10 TeV γ-ray luminosity of galactic SNRs shown in figure 7.10. The meaning of the symbols in figure 7.10, is summarized in table 7.2. Unlike the case of synchrotron X-ray, there is no clear trend in luminosity distribution. The radiation mechanisms of TeV γ-ray are (i) Inverse Compton Scattering (IC), (ii) non-thermal bremsstrahlung, from high energy electrons, or (iii) decay of neutral pions which is caused by the interaction with high energy protons and dense gas, as noted in §2.3. Solid lines in figure 7.10 are calculated radius-TeV luminosity curves on the assumption that TeV γ-rays are emitted by IC scattering by the same population of the high energy electrons responsible for the X-ray synchrotron emission (1-zone IC

scattering). In this calculation, we used the electron distribution constructed in §7.3.1 to explain the correlation with radius and synchrotron X-ray luminosity. The TeV γ-ray luminosity of IC scattering was calculated with eq. (2.49). The calculated luminosity curves have a cut-off at $R \sim$3 pc with n_0=1 cm^{-3}, $\sim$10 pc with n_0=0.1 cm^{-3}, and 20 pc with n_0=0.01 cm^{-3}, while the observed luminosity does not show such a cut-off. In addition, the calculated luminosity is smaller than the observed one by a factor of $\sim$100. These suggest that TeV γ-ray emission is due to the decay of neutral pions generated by accelerated protons, or at least multi-zone IC scattering needs to be incorporated if we stick to the IC origin. However, in the case of large (old) SNRs, TeV γ-ray is probably emitted by proton origin, since there are SNRs not only with low density ($n_0 = 0.01$ cm^{-3}) but also with $n_0 > 0.1$ cm^{-3}.

Table 7.2: Meaning of the difference of marks in figure 7.10

	Molecular cloud detection	Morphology coincidence of TeV γ-ray and MC
●	yes	yes
△	yes	unknown
×	no or unknown	—

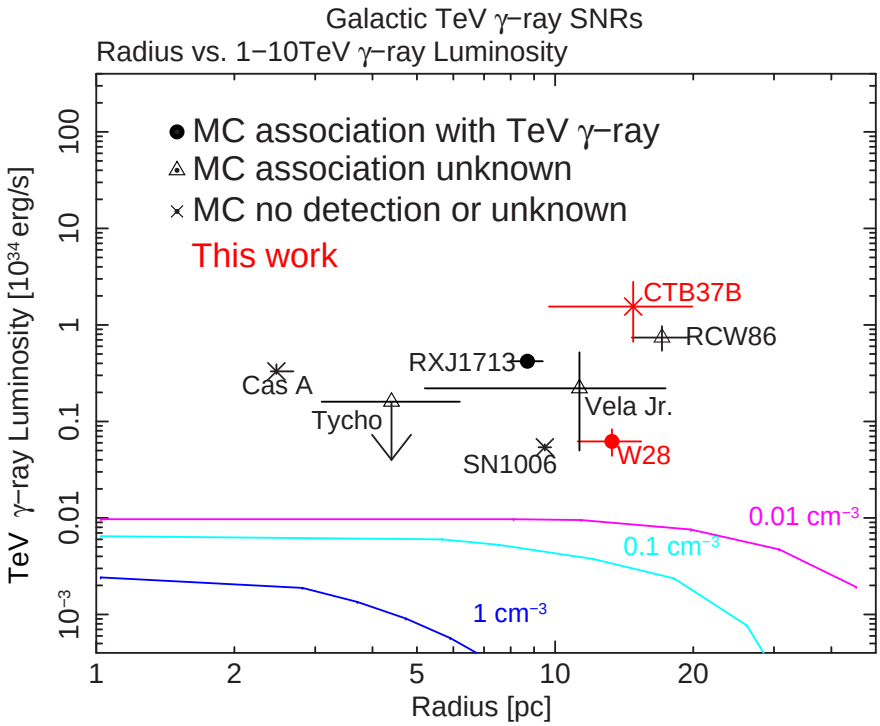

Figure 7.10: Correlation between radius and 1–10 TeV γ-ray luminosity of Galactic SNRs

Chapter 8

Conclusion

We study on cosmic-ray acceleration history in the shocks of SNRs through observations of synchrotron X-ray radiation from accelerated electrons.

As a first step, we discovered synchrotron X-ray from two SNRs W28 and CTB37B, from which TeV γ-ray were detected. These observational results are summarized as follows,

- We analyzed the *XMM-Newton* data of the north-eastern part of the middle-aged SNR W28. With spatially-resolved spectroscopy, we got the following results.

  (i) Hard-tail X-ray emission was discovered from just behind the shock region. We suggest that this hard component is probably synchrotron X-ray emission by accelerated high energy electrons. The spectrum is described by a power-law model with a photon index of $\sim$3.0, and the 2–10 keV luminosity of 6.9×10^{32} erg/s. Thermal plasma emission was detected from the same region, with a temperature kT, a pre-shock electron density n_0, and an age $t_{\rm age}$ of $\sim$ 0.3 keV, $\sim$ 0.1 cm^{-3}, and several times 10^4 yr, respectively. The electron density is much lower than the typical electron density of galactic plane of $\sim$ 1 cm^{-3}.

  (ii) Spectrum of north-eastern shell region was represented with single temperature ionization equilibrium model with kT of $\sim$ 0.3 keV. The electron density is found to be as high as $n_0 \simeq 2$ cm^{-3}, as opposed to inner region. Synchrotron X-ray was not detected from shell region.

  (iii) We obtained the tight upper limit flux of $< 2.1 \times10^{-14}$ erg cm^{-2} s^{-1} in the 2–10 keV band from one of the TeV γ-ray peak. We calculated the hadronic process spectra, and found that π^0-decay emission is dominant in TeV γ-ray band. Using X-ray upper limit flux, a weak upper limit of magnetic field was obtained $B \leq 1500$ μG.

- We obtained the images and high-quality spectra of CTB37B with *Suzaku*. The X-ray emission consists of thermal and synchrotron X-ray diffuse components as well as a point source resolved by *Chandra*.

  (i) The diffuse emission spectrum around the point source was represented with single temperature non-equilibrium collisional ionization plasma model with $kT = 0.9\pm0.2$ keV, $n_0 = 0.4\pm0.1$ cm^{-3} and $t_{\rm age} = 650^{+2500}_{-300}$ yr, respectively.

(ii) Synchrotron X-ray was discovered from southern region of CTB37B, in addition to weak thermal plasma emission. A photon index and the 2–10 keV luminosity of synchrotron X-ray are 1.5 and 9.7×10^{33} erg/s, respectively. The tight upper limit of pre-shock electron density was obtained to be $n_0 < 0.21$ cm^{-3} from the spectral fitting of thermal plasma.

(iii) By the wide-band spectral fitting from X-ray to TeV γ-ray, TeV γ-ray could be emitted by multi-zone Inverse Compton scattering, or the decay of neutral pions.

(iv) The measured hydrogen column density of point source is same with that of diffuse emission. We thus attribute that point source is associated physically with the diffuse emission, and CTB37B is core-collapse SNR.

In the next step, we have compiled a sample of the SNRs with synchrotron X-ray with several physical parameters; a physical radius, a synchrotron X-ray luminosity, a thermal plasma density, and so on, including our new results of W28 and CTB37B. To study the time evolution of electron acceleration, we have checked the relation between the radius and the X-ray luminosity. Results are summarized as follows:

- A trend was found from radius-luminosity relation that the X-ray luminosity decrease with increasing the SNR radius, with drop-off around the radius of $\sim$10 pc.
- We constructed a simple model to explain the observed radius-luminosity relation. This model was based on dynamic and magnetic evolution of SNR, and a diffusive shock acceleration theory. The observational luminosity trend can be explained with this simple model.
- Plasma density of acceleration site is effective parameter for the electron acceleration history. Maximum electron energy $E_{\rm max,e}$ is higher, and the acceleration time scale of electron up to $\sim$ TeV from which emits synchrotron X-ray is longer with low plasma density n_0. The measured thermal plasma density of collected samples, except for the young SNR Cas A, are $n_0 < 1.0$, which is consistent with this result. $E_{\rm max,e}$ is obtained to be 10^{13}–10^{14} eV with our model.
- We also studied the proton acceleration history using the same model. Protons are accelerated up to $\sim 10^{15}$ eV with little density dependence of ${n_0}^{1/6}$. Protons quickly reach a maximum energy in free expansion phase, and is kept at $\sim10^{15}$ eV with little energy loss.
- We studied the relation between radius and TeV γ-ray luminosity. In contrast to the synchrotron X-ray luminosity, there is no luminosity drop-off. We calculated the light curve of TeV γ-ray due to the Inverse Compton scattering using our model. The calculated luminosity is smaller than the observed one by a factor of $\sim$ 100, and the luminosity drops off around $5 \leq R \leq 10$ pc with $n_0 > 0.1$ cm^{-3}. These suggest that TeV γ-ray emission is due to the decay of neutral pions generated by accelerated protons, or at least multi-zone IC scattering needs to be incorporated if we stick to the IC origin. However, in the case of large (old) SNRs, TeV γ-ray is probably emitted by proton origin.

Appendix A

Point source Analysis detected from CTB37B region

Here we describe the analysis, result and discussion of point source, defined source B in §6, detected from CTB37B region. Figure A.1 shows Suzaku and Chandra images of CTB37B in 0.3–3.0 keV and 0.3–10 keV. Source B locates in region 3.

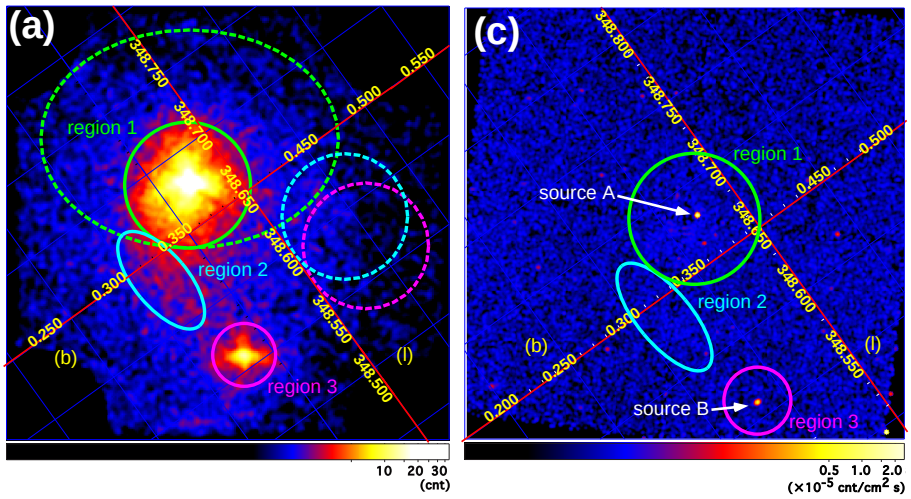

Figure A.1: Images of CTB37B in the galactic coordinates. Left is Suzaku image in 0.3–3 keV and right is Chandra image in 0.3–10 keV. Source B was detected in region 3.

A.1 Spectral Analysis

The emission from region 3 is mainly from source B, thus we used Suzaku data for the spectral analysis because of high quality statics. Magenta dashed circle in figure A.1 (left) are corresponding background-integration region.

Fig. A.2 shows the background-subtracted spectra of region 3. As indicated by the images in figure A.1(left), X-ray flux is detected only below ∼3 keV. Since the absorption is apparently weak and there is Fe-L hump in the 0.7-0.9 keV band, this source seems to be a foreground point source, probably an active star. We thus adopted a model composed of

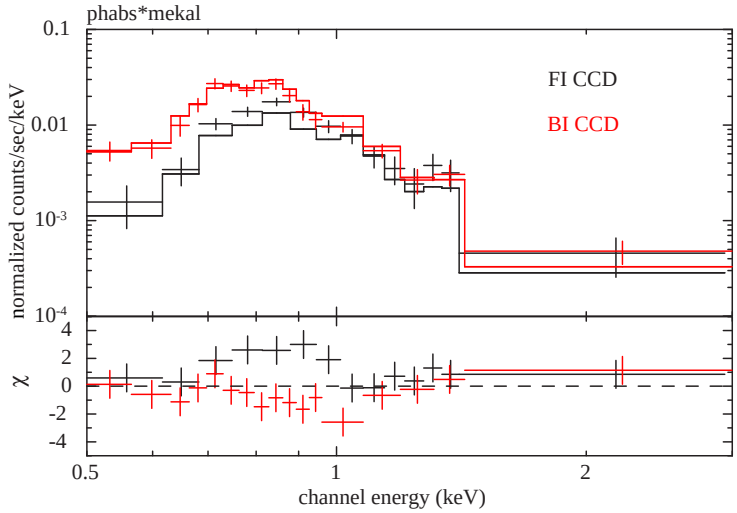

Figure A.2: The XIS spectra of region 3 with the MEKAL model.

a thin thermal collisional equilibrium plasma emission model ("mekal" model in XSPEC; Mewe et al. (1985, 1986); Liedahl et al. (1995); Kaastra et al. (1996)) multiplied by photoelectric absorption, and fitted this model to the spectra in the 0.5–2.0 keV band. The result is shown in Fig. A.2, and the best-fit parameters are listed in Table A.1. Note that the fit residuals exhibit different behavior in the 0.7–1.0 keV band between the FI and BI CCDs. This is probably attributed to calibration uncertainty.

Table A.1: Best-fit parameters of the CTB37B region 3 spectrum

MEKAL	
Temperature [keV]	$0.46^{+0.03}_{-0.05}$
Abundance [1]	$0.20^{+0.12}_{-0.07}$
Normalization [2] [cm^{-3}]	$2.5^{+1.4}_{-0.6}\times10^{-4}$
phabs	
N_H [3]	<0.046
χ^2/d.o.f	52.9/27

[1] Abundance ratio relative to the solar value (Anders & Grevesse, 1989).
[2] Normalization is $\frac{10^{-14}}{4\pi D_A^2}\int n_e n_H dV$ where D_A is the angular size distance to the source (cm), n_e and V are the electron density and the plasma volume.
[3] Absorption column in units of 10^{22} cm^{-2}.

A.2 Timing Analysis

We created a light curve of source B in the 0.5–2.0 keV band with Suzaku, which is shown in Fig. A.3. The time bin size is 512 s. Although we detected no drastic flare event,

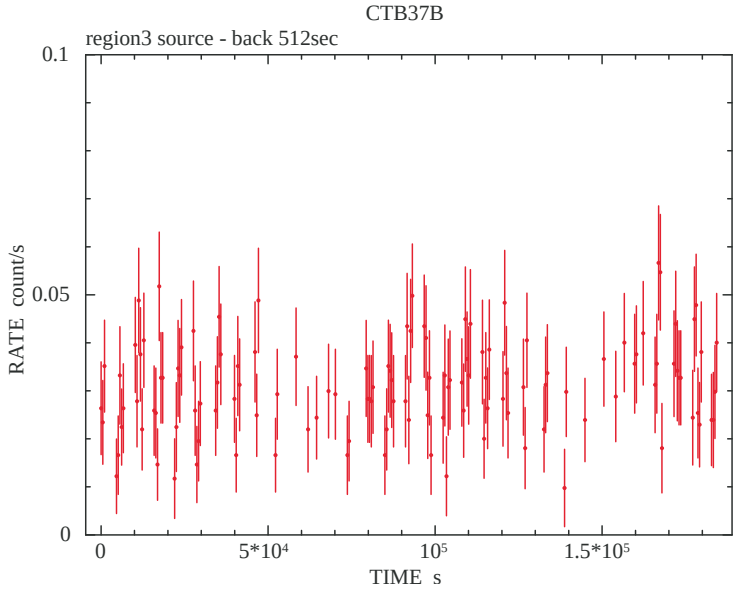

Figure A.3: The light curve of CTB37B region 3 detected with *Suzaku* in the 0.5–2.0 keV band. The time bin size is 512 s.

the light curve seems to show flickering. In fact, Kolmogorov–Smirnov test indicates the probability of no variability in the light curve is 0.0012.

A.3 Discussion

From the spectrum fitting, The hydrogen column density obtained from the fit to the Suzaku region 3 spectra $N_{\rm H} < 4 \times 10^{20} {\rm cm}^{-2}$ (table A.1) is much smaller than that obtained from region 1 and 2 ($N_{\rm H} \sim 3.5 \times 10^{22} {\rm cm}^{-2}$, see table 6.2 and 6.3). This result indicates that source B is a foreground source. The best-fit plasma temperature of $kT \simeq 0.5$ keV is reminiscent of an active star. The existence of flickering supports this suggestion.

Bibliography

Abdo, A. A., et al. 2009, ApJS, 183, 46

Aharonian, F. A., & Atoyan, A. M. 1996, A&A, 309, 917

Aharonian, F. A., Atoyan, A. M., & Kifune, T. 1997, MNRAS, 291, 162

Aharonian, F. A., & Atoyan, A. M. 1999, A&A, 351, 330

Aharonian, F. A., et al. 2001, A&A, 373, 292

Aharonian, F. A., et al. 2004, Nature, 432, 75

Aharonian, F., et al. 2006, ApJ, 636, 777

Aharonian, F., et al. 2007a, A&A, 472, 489

Aharonian, F., et al. 2007b, ApJ, 661, 236

Aharonian, F., et al. 2008a, A&A, 481, 401

Aharonian, F., et al. 2008b, A&A, 486, 829

Aharonian, F., et al. 2009, ApJ, 692, 1500

Albert, J., et al. 2007, A&A, 474, 937

Anders, E., & Grevesse, N. 1989, Geochim. Cosmochim. Acta, 53, 197

Arikawa, Y., Tatematsu, K., Sekimoto, Y., & Takahashi, T. 1999, PASJ, 51, L7

Bamba, A., Koyama, K., & Tomida, H. 2000, PASJ, 52, 1157

Bamba, A., Ueno, M., Koyama, K., & Yamauchi, S. 2001, PASJ, 53, L21

Bamba, A., Yamazaki, R., Yoshida, T., Terasawa, T., & Koyama, K. 2005, ApJ, 621, 793

Bamba, A., et al. 2008a, PASJ, 60, 153

Bamba, A., et al. 2008b, Advances in Space Research, 41, 411

Bell, A. R. 1978, MNRAS, 182, 147

Blondin, J. M., Wright, E. B., Borkowski, K. J., & Reynolds, S. P. 1998, ApJ, 500, 342

Borkowski, K. J., Sarazin, C. L., & Blondin, J. M. 1994, ApJ, 429, 710

Borkowski, K. J., Lyerly, W. J., & Reynolds, S. P. 2001, ApJ, 548, 820

Bressaard, P. J., & van de Hulst, H. C. 1962, Rev. Mod. Phys., 34, 507

Brickhouse, N. S., Dupree, A. K., Edgar, R. J., Liedahl, D. A., Drake, S. A., White, N. E., & Singh, K. P. 2000, ApJ, 530, 387

Case, G. L., & Bhattacharya, D. 1998, ApJ, 504, 761

Caswell, J. L., Murray, J. D., Roger, R. S., Cole, D. J., & Cooke, D. J. 1975, A&A, 45, 239

Chevalier, R. A. 1974, ApJ, 188, 501

Clark, D. H., Green, A. J., & Caswell, J. L. 1975, Australian Journal of Physics Astrophysical Supplement, 37, 75

Claussen, M. J., Frail, D. A., Goss, W. M., & Gaume, R. A. 1997, ApJ, 489, 143

Condon, J. J., Cotton, W. D., Greisen, E. W., Yin, Q. F., Perley, R. A., Taylor, G. B., & Broderick, J. J. 1998, AJ, 115, 1693

Dubner, G. M., Velázquez, P. F., Goss, W. M., & Holdaway, M. A. 2000, AJ, 120, 1933

Dwarkadas, V. V. 2005, ApJ, 630, 892

Ellison, D. C., Berezhko, E. G., & Baring, M. G. 2000, ApJ, 540, 292

Fahlman, G. G., & Gregory, P. C. 1981, Nature, 293, 202

Frail, D. A., Goss, W. M., & Slysh, V. I. 1994, ApJL, 424, L111

Frail, D. A., Goss, W. M., Reynoso, E. M., Giacani, E. B., Green, A. J., & Otrupcek, R. 1996, AJ, 111, 1651

Fukui, Y., et al. 2003, PASJ, 55, L61

Fukui, Y., Inuzuka, S., Ohnishi, T., Nakai, T., Maihara, T., Mizuno, R., 2008, “星間物質と星生成”, 日本評論社 (§3.1)

Gaetz, T. J., & Salpeter, E. E. 1983, ApJS, 52, 155

Gaisser, T. K. 2006, Journal of Physics Conference Series, 47, 15

Gaisser, T. K., & Stanev, T. 2006, Nuclear Physics A, 777, 98

Garcia-Munoz, M., Mason, G. M., & Simpson, J. A. 1977, ApJ, 217, 859

Gavriil, F. P., & Kaspi, V. M. 2002, ApJ, 567, 1067

Gehrels, N., & Williams, E. D. 1993, ApJL, 418, L25

Gerardy, C. L., & Fesen, R. A. 2007, MNRAS, 376, 929

Ghavamian, P., Laming, J. M., & Rakowski, C. E. 2007, ApJL, 654, L69

Ginzburg, V. L., & Syrovatskii, S. I. 1964, The Origin of Cosmic Rays, New York: Macmillan, 1964,

Green, A. J., Frail, D. A., Goss, W. M., & Otrupcek, R. 1997, AJ, 114, 2058

Green, A. J., Cram, L. E., Large, M. I., & Ye, T. 1999, ApJS, 122, 207

Green, D. A. 2009, VizieR Online Data Catalog, 7253, 0

Halpern, J. P., & Gotthelf, E. V. 2009, arXiv:0912.4985

Hamilton, A. J. S., Chevalier, R. A., & Sarazin, C. L. 1983, ApJS, 51, 115

Helder, E. A., & Vink, J. 2008, ApJ, 686, 1094

Hess, V. F. 1911, Phys. Zeits., 12, 998

Hess, V. F. 1912, Phys. Zeits., 13, 1084

Hoffman, I. M., Goss, W. M., Brogan, C. L., & Claussen, M. J. 2005, ApJ, 620, 257

Ishisaki, Y., et al. 2007, PASJ, 59, 113

Jansen, F., et al. 2001, A&A, 365, L1

Jokipii, J. R. 1987, ApJ, 313, 842

Jones, F. C. 1968, Physical Review , 167, 1159

Kaastra, J. S., Mewe, R., & Nieuwenhuijzen, H. 1996, UV and X-ray Spectroscopy of Astrophysical and Laboratory Plasmas, 411

Karzas, W. J., & Latter, R. 1961, ApJS, 6, 167

Kaspi, V. M., Gavriil, F. P., Woods, P. M., Jensen, J. B., Roberts, M. S. E., & Chakrabarty, D. 2003, ApJL, 588, L93

Kassim, N. E., Weiler, K. W., & Baum, S. A. 1991, ApJ, 374, 212

Katsuda, S., Petre, R., Hwang, U., Yamaguchi, H., Mori, K., & Tsunemi, H. 2009, PASJ, 61, 155

Kifune, T., 2004, "宇宙高エネルギー粒子の物理学", 培風館 (§2.3.4)

Kokubun, M., et al. 2007, PASJ, 59, 53

Koyama, K., Petre, R., Gotthelf, E. V., Hwang, U., Matsuura, M., Ozaki, M., & Holt, S. S. 1995, Nature, 378, 255

Koyama, K., Kinugasa, K., Matsuzaki, K., Nishiuchi, M., Sugizaki, M., Torii, K., Yamauchi, S., & Aschenbach, B. 1997, PASJ, 49, L7

Koyama, K., et al. 2007, PASJ, 59, 23

Krause, O., Tanaka, M., Usuda, T., Hattori, T., Goto, M., Birkmann, S., & Nomoto, K. 2008, Nature, 456, 617

Kuiper, L., Hermsen, W., den Hartog, P. R., & Collmar, W. 2006, ApJ, 645, 556

Landau, L. D., & Lifshitz, E. M. 1959, Course of theoretical physics, Oxford: Pergamon Press, 1959,

Lazendic, J. S., Dewey, D., Schulz, N. S., & Canizares, C. R. 2006, ApJ, 651, 250

Liedahl, D. A., Osterheld, A. L., & Goldstein, W. H. 1995, ApJL, 438, L115

Longair, M. S. 1992, High Energy Astrophysics, by Malcolm S. Longair, pp. 436. ISBN 0521387736. Cambridge, UK: Cambridge University Press, March 1992.,

Longair, M. S. 1994, Cambridge: Cambridge University Press, —c1994, 2nd ed.,

Maeda, Y., et al. 2009, PASJ, 61, 1217

Makishima, K., et al. 1996, PASJ, 48, 171

Masai, K. 1994, ApJ, 437, 770

Matsumoto, H., et al. 2007, PASJ, 59, 199

Melitta, N., Marianne, L., & Mathieu, de, N., 2009, ICRC, Proceedings of the 31^{st}

Mewe, R., Gronenschild, E. H. B. M., & van den Oord, G. H. J. 1985, A&AS, 62, 197

Mewe, R., Lemen, J. R., & van den Oord, G. H. J. 1986, A&AS, 65, 511

Mitsuda, K., et al. 2007, PASJ, 59, 1

Nakamura, R., Bamba, A., Ishida, M., Nakajima, H., Yamazaki, R., Terada, Y., Pühlhofer, G., & Wagner, S. J. 2009, PASJ, 61, 197

Nishiuchi, M. 2000, Ph.D. Thesis,

Ohashi, T., et al. 1996, PASJ, 48, 157

Ohira, Y., Murase, K., & Yamazaki, R. 2009, arXiv:0910.3449

Parizot, E., Marcowith, A., Ballet, J., & Gallant, Y. A. 2006, A&A, 453, 387

Reed, J. E., Hester, J. J., Fabian, A. C., & Winkler, P. F. 1995, ApJ, 440, 706

Reynolds, S. P. 1998, ApJ, 493, 375

Reynolds, S. P., & Keohane, J. W. 1999, ApJ, 525, 368

Reynolds, S. P., Borkowski, K. J., Hwang, U., Hughes, J. P., Badenes, C., Laming, J. M., & Blondin, J. M. 2007, ApJL, 668, L135

Reynolds, S. P., Borkowski, K. J., Green, D. A., Hwang, U., Harrus, I., & Petre, R. 2008, ApJL, 680, L41

Rho, J., Dyer, K. K., Borkowski, K. J., & Reynolds, S. P. 2002, ApJ, 581, 1116

Rho, J., & Borkowski, K. J. 2002, ApJ, 575, 201

Rosado, M., Ambrocio-Cruz, P., Le Coarer, E., & Marcelin, M. 1996, A&A, 315, 243

Rybicki, G. B., & Lightman, A. P. 1986, Radiative Processes in Astrophysics, by George B. Rybicki, Alan P. Lightman, pp. 400. ISBN 0-471-82759-2. Wiley-VCH , June 1986.,

Sedov, L. I. 1959, Similarity and Dimensional Methods in Mechanics, New York: Academic Press, 1959,

Serlemitsos, P. J., et al. 2007, PASJ, 59, S9

Seward, F., Gorenstein, P., & Tucker, W. 1983, ApJ, 266, 287

Skilling, J. 1975, MNRAS, 172, 557

Slane, P., Gaensler, B. M., Dame, T. M., Hughes, J. P., Plucinsky, P. P., & Green, A. 1999, ApJ, 525, 357

Smith, D. A., & Wang, Q. D. 2004, ApJ, 611, 881

Stephenson, F. R., & Green, D. A. 2002, Unknown,

Sugizaki, M., Mitsuda, K., Kaneda, H., Matsuzaki, K., Yamauchi, S., & Koyama, K. 2001, ApJS, 134, 77

Takahashi, T., et al. 2007, PASJ, 59, 35

Takahashi, T., et al. 2008, PASJ, 60, 131

Takahata, F., 2002, “天体高エネルギー現象”, 岩波出版 (§2.2, §3.1)

Tanaka, Y., Inoue, H., & Holt, S. S. 1994, PASJ, 46, L37

Tamagawa, T., et al. 2009, PASJ, 61, 167

Tian, W. W., & Leahy, D. A. 2008, ApJ, 677, 292

Velázquez, P. F., Dubner, G. M., Goss, W. M., & Green, A. J. 2002, AJ, 124, 2145

Vink, J., Bleeker, J., van der Heyden, K., Bykov, A., Bamba, A., & Yamazaki, R. 2006, ApJL, 648, L33

Voges, W., et al. 1999, A&A, 349, 389

Wang, Z. R., Qu, Q.-Y., & Chen, Y. 1997, A&A, 318, L59

Wardle, M., & Yusef-Zadeh, F. 2002, Science, 296, 2350

Weisskopf, M. C., Brinkman, B., Canizares, C., Garmire, G., Murray, S., & Van Speybroeck, L. P. 2002, PASP, 114, 1

Willingale, R., Bleeker, J. A. M., van der Heyden, K. J., & Kaastra, J. S. 2003, A&A, 398, 1021

Winkler, P. F., Gupta, G., & Long, K. S. 2003, ApJ, 585, 324

Wootten, A. 1981, ApJ, 245, 105

Yamaguchi, H., Ueno, M., Koyama, K., Bamba, A., & Yamauchi, S. 2004, PASJ, 56, 1059

Yamaguchi, H., et al. 2008, PASJ, 60, 141

Yamauchi, S., Koyama, K., Tomida, H., Yokogawa, J., & Tamura, K. 1999, PASJ, 51, 13

Yamauchi, S., Ueno, M., Koyama, K., & Bamba, A. 2008, PASJ, 60, 1143

Yamazaki, R., Yoshida, T., Terasawa, T., Bamba, A., & Koyama, K. 2004, A&A, 416, 595

Yamazaki, R., Kohri, K., Bamba, A., Yoshida, T., Tsuribe, T., & Takahara, F. 2006, MNRAS, 371, 1975

Yusef-Zadeh, F., Roberts, D. A., Goss, W. M., Frail, D. A., & Green, A. J. 1996, ApJL, 466, L25

Zirakashvili, V. N., & Aharonian, F. 2007, A&A, 465, 695

Acknowledgments

I had a wonderful time with the supports of many people for five years in ISAS. This thesis could not be completed without their help.

First of all, I am deeply grateful to Professor Manabu Ishida, who has given and shown me a pleasure to study astrophysics, an attitude toward study, and very important thing to work in the society. His positive advice have encouraged me many times not only in the research but also in my life.

I greatly appreciate Dr. Aya Bamba in ISAS for giving me a chance to study about Supernova Remnant. She have always watched over close to me, and encouraged me countlessly. She also provided me an opportunity to meet a lot of international researchers. I was very happy to study with her.

I express my thanks to Dr. Ryo Yamazaki in Hiroshima University for giving many advice from a theoretical point of view. It was impressive when the observational results were linked to the theoretical predictions. I thank to Dr. Kazunori Kohri, Professor Ken'ichi Tatematsu, Dr. Hiroshi Nakajima, and associate professor Yukikatsu Terada, who were collaborators of this thesis, for discussing the interpretation of the results not only in X-ray but also in multi-wavelength. I also appreciate to Dr. Gerd Pühlhofer and Professor Stefan J. Wagner for giving me H.E.S.S. data and useful comments about the analysis and results.

I wish to thank to all members in ISAS X-ray group. I had very pleasant time to talk and discuss with them. I was encouraged by them countless times.

And I am deeply grateful for my supervisor Professor Tadayasu Dotani for providing an opportunity to study X-ray astronomy in ISAS. I have learned importance of interpreting the analysis results accurately, and confirming the obtained results. I hope to apply what I have learned to the future.

Finally, I would like to thank to my family for their supports, encouragements, and understandings. The time to spend with my family was relieved me through hard times.